Atoms in non-Dissipative Optical Lattices

Silvia Bergamini

A thesis submitted in partial fulfilment of
the requirements for the degree of
Doctor of Philosophy at the University of London

University College London
University of London
2002

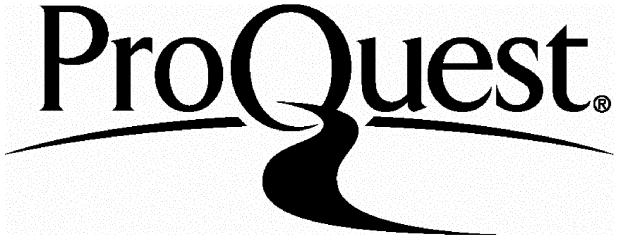

ABSTRACT

Optical lattices induced by light detuned far from the frequency of any atomic resonance transition are ideal systems in which to develop techniques for the coherent control of atomic motional and internal states. Decoherence arising from spontaneous emission can be eliminated to an arbitrary degree by varying the detuning of the optical field. The atoms trapped in these lattices are to a large extent isolated from environmental disturbances and from each other. The first step towards the coherent control of atoms in a far-detuned lattice is their preparation in a single motional state.

In this thesis the preparation of atoms in the ground vibrational state of a two-dimensional far-detuned optical lattice via resolved-sideband Raman cooling is presented. This sideband-cooling scheme involves stimulated Raman transitions between bound vibrational states of a pair of magnetic ground state sublevels, followed by an irreversible step due to optical pumping, resulting in a net loss of one quantum of vibrational energy per cooling cycle. This process provides efficient cooling in two-dimensions and leads to the accumulation of a large fraction of atoms in the 2-D ground vibrational state of a potential well associated with a single Zeeman substate.

Experiments aimed at improving and monitoring the characteristics of the far-detuned lattice and the sideband-Raman cooling efficiency are also described. Parametric excitation experiments and modelling are employed to investigate the

degree of anharmonicity of the optical potential and the importance of heating induced by laser intensity noise, whilst Zeeman-state analysis of the sample is performed for monitoring the distribution of atoms over different magnetic sub-states. Finally, spin-polarization experiments are carried out in order to study the paramagnetic properties of the lattice and lead to an evaluation of a spin-temperature for the sample.

ACKNOWLEDGEMENTS

I'd like to thank David Meacher first of all for giving me the possibility of working on this project and for the help he gave me through my PhD, but also for his friendly way of supervising and very good meals that he cooked for us!

I wish also to thank Philip Jones for his invaluable help in the lab with his expertise of lasers and optics, for answering to my many questions without complaining and for some, very much appreciated, artistic drawings! Many thanks also to Stephan Winklbauer for his very good theoretical work, helpful discussions and for the gift of his old PC. Harry Saunders-Singer gave me a lot of help by patiently and very professionally dealing with some electronics; many thanks, really! Also thanks to Matthew Isherwood, for helpful discussions and nice coffee breaks. Last but not least, best wishes to Malika Goonasakera, who just started her PhD in the group.

Contents

1 Introduction **13**

1.1 Principles of laser cooling 13

1.1.1 Atom-light interaction and light-induced forces 14

1.1.2 Doppler cooling 15

1.1.3 The magneto-optical trap 16

1.1.4 Sub-Doppler cooling 18

1.1.4.1 Motion induced orientation effect 19

1.1.4.2 Sisyphus cooling for an atomic configuration with $F_g = 1/2$ 20

1.1.4.3 Sisyphus cooling for an atomic configuration with $F_g \geq 1$ 23

1.2 Introduction to optical lattices 25

1.2.1 Laser cooling in optical lattices 25

1.2.1.1 Quantization of the atomic motion and band theory 29

1.2.2 Optical Lattice in one dimension 30

1.2.3 Optical lattices in two and three dimensions 31

1.2.3.1 2-D Optical lattice 31

1.2.3.2 3-D Optical Lattice 33

1.3 Aims of this thesis and outline 34

2 Non-Dissipative Optical Lattices 37

2.1 Optical potential in the far-detuned regime and fictitious magnetic field 38

2.2 Effects of static magnetic fields 40

2.3 Band-structure of the 2-D far-detuned optical lattices 41

2.4 Theory of resolved-sideband Raman cooling 47

2.5 Population distribution over vibrational levels 55

2.6 Conclusions 57

3 The Experimental Apparatus 58

3.1 The caesium source 59

3.2 Laser frequency stabilization 59

3.3 Grating-stabilized diode lasers 62

3.4 Laser frequency stabilization on an atomic resonance 65

3.5 Injection locking 70

3.6 Master Oscillator Power Amplifier 73

3.7 Magnetic fields 76

3.8 Time-of-Flight setup 77

3.9 Computer-automation of the system 80

3.10 Conclusions 81

4 Atoms in a Far-Detuned Optical Lattice 82

4.1 Preparation of a cooled sample in a near-detuned optical lattice. . 83

4.2 Loading the Far-detuned Optical Lattice 87

4.2.1 Far-Detuned Optical Lattice Setup 88

4.2.2 Studies of transfer efficiency and losses in the far-detuned lattice 93

4.3 Band population measurements 98
4.4 Conclusions 104

5 Parametric Excitation **105**
5.1 Perturbative treatment of parametric excitations 106
5.1.1 First order perturbation theory 110
5.1.2 Second order perturbation theory and anharmonicity 111
5.2 Parametric Excitation Simulations 113
5.3 Parametric Excitation Measurements 117
5.4 Noise-induced heating rates 122
5.5 Conclusions 124

6 Stern-Gerlach Analysis of Zeeman-state Populations **126**
6.1 Atoms interacting with a magnetic field 128
6.2 Stern-Gerlach simulations 130
6.3 Stern-Gerlach experiments 132
6.4 Magnetization and spin temperature in the near-resonant lattice. . 138
6.4.1 A model for quasi-thermal distribution of spin population . 140
6.4.2 Spin-polarization experiments 144
6.5 Conclusions 154

7 Resolved Sideband-Raman Cooling **155**
7.1 Experimental setup for resolved-sideband Raman cooling 156
7.2 Resolved-Sideband Raman cooling 158
7.2.1 Resolved-sideband limit and causes of broadening 160
7.2.2 Experimental results 161
7.3 Conclusions 169

8 Conclusions **171**

List of Figures

1.1 Scheme of a magneto-optical trap in 1-dimension for a $F = 0 \rightarrow F' = 1$ transition. 17

1.2 Representation of the $\sigma^+ - \sigma^-$ polarized optical molasses configuration. 19

1.3 Induced orientation effect. 20

1.4 Representation of the linear-orthogonal-linear polarization optical molasses configuration. 21

1.5 Semiclassical picture for the Sisyphus cooling on a $F_g = 1/2 \rightarrow F_e = 1/2$ transition. 22

1.6 Semiclassical picture for the Sysiphus cooling on a $F_g = 2 \rightarrow F_e = 3$ transition. 24

1.7 a) level structure of a $F_g = 2 \rightarrow F_e = 3$ atom. Lower left: diabatic potential obtained ignoring coupling between different m_F states Lower right: adiabatic potential obtained considering coupling $\Delta m_{g,} = \pm 2$ 27

1.8 Two dimensional optical lattice configurations for $\theta = \pi/3$, with (A) all the beams polarizations lying on the lattice plane and (B) one of the beams polarization lying on the lattice plane and the two other orthogonal to the lattice plane. 32

1.9 Three dimensional tetragonal optical lattice configurations generated with four beams. 34

2.1 Lowest potential surface of a 2-D optical lattice associated with $m_F = \pm 4$ states. 42

2.2 2D contour plot of the potential surface of a 2-D optical lattice associated with $m_F = -4$ state. 43

2.3 Band structure for a potential depth of 170 E_R, cut in the x-direction. 44

2.4 Band structure for a potential depth of 250 E_R, cut in the x-direction 45

2.5 Band structure for a potential depth of 170 E_R, cut in the y-direction 46

2.6 Band structure for a potential depth of 250 E_R, cut in the y-direction 47

2.7 Experimental setup for resolved-sideband Raman cooling: Raman coupling is introduced by adding a π-polarized component (red) to the light field. 50

2.8 Experimental setup for resolved-sideband Raman cooling. 52

2.9 Band structure for the $m_F = 4$ (blue) potential and $m_F = 3$ (purple) potential. 53

2.10 Magnetic field to tune to the first red sideband for different potential depths. 54

2.11 Block diagram for population of different vibrational levels at different temperatures for 1-D harmonic oscillator for ground state kinetic temperature T_0. 55

2.12 Block diagram for population of different vibrational levels at different temperatures for a 2-D harmonic oscillator with $n_x = 0, n_y = n$ and ground state kinetic temperature T_0. 57

3.1 Scheme of the hyperfine structure for caesium atom. 60
3.2 Scheme of frequencies for the near-detuned lattice and trap beam, as obtained by shifting the master-injecting frequency. 62
3.3 Scheme of the external cavity configuration. 63
3.4 Scheme of the grating in the Littrow configuration. 64
3.5 Representation of the saturation absorption scheme use to stabilize lasers frequency. 66
3.6 Caesium saturated absorption spectrum. Cooling transitions: $6S_{1/2}, F = 4 \rightarrow 6P_{3/2}, F'$. 68
3.7 Derivative of caesium saturated absorption spectrum. Cooling transitions: $6S_{1/2}, F = 4 \rightarrow 6P_{3/2}, F'$. 69
3.8 Caesium saturated absorption spectrum. Repumping transitions: $6S_{1/2}, F = 3 \rightarrow 6P_{3/2}, F'$. 70
3.9 Derivative of caesium saturated absorption spectrum. Repumping transitions: $6S_{1/2}, F = 3 \rightarrow 6P_{3/2}, F'$. 71
3.10 Slave laser design. 72
3.11 Injection locking scheme. 73
3.12 Injection locking signal. 74
3.13 Layout of the optical bench. 75
3.14 Tapered amplifier mount design. 76
3.15 MOPA system consisting of a DBR and TA. 77
3.16 Time-of-flight scheme. 78

4.1 Representation of the lattice plane and quantization axis. 84
4.2 TOF signal of the near detuned lattice and Gaussian fit (dotted line) to extract the temperature. 85
4.3 Probe transmission spectrum through a 2D lattice. 87

4.4 Experimental setup to overlap far-detuned (FD) and near-detuned (ND) beams to form the lattice. 89
4.5 Intensity profile of the far-detuned beam along the horizontal direction. 91
4.6 Intensity profile of the far-detuned beam along the vertical direction. 92
4.7 TOF signal obtained for two different loading times for the far-detuned lattice. 94
4.8 Life-time measurement for the far detuned lattice. 95
4.9 Temperature decay of far-detuned lattice versus time duration. . . 97
4.10 Selecting the lower bands for quantum state preparation. 99
4.11 Measurement of population and temperature variation for selected bands. 100
4.12 Results of band calculations for $U_{max} = 140E_R$. 100
4.13 Results of band calculations for $U_{max} = 80E_R$. 101
4.14 Results of band calculations for $U_{max} = 28E_R$. 101
4.15 Band-dependent losses versus storage time. 102

5.1 Simulation of parametrically induced losses versus modulation frequency and time for: $U_{max} = 200E_R$, $m_F = -4$, $T_{in} = 3\mu$K, $\epsilon_0 = 0.1$, $\sigma_0 = 1.5E_R$. 115
5.2 Simulation of parametrically induced temperature variation versus modulation frequency and time for: $U_{max} = 200E_R$, $m_F = -4$, $T_{in} = 3\mu$K, $\epsilon_0 = 0.1$, $\sigma_0 = 1.5E_R$. 116
5.3 Experimental spectrum of the losses induced by parametrically exciting the lattice vibrational modes. 117
5.4 Comparison between experimental and theory data for population losses. 119

5.5 Experimental spectrum of the change in kinetic temperature induced by parametrically exciting the lattice vibrational modes. . . 120

5.6 Comparison between experimental and theory data for kinetic temperature variations. 121

5.7 Mean energy growth due to intensity noise in the far-detuned lattice beam 124

6.1 Simulated TOF spectrum for a a Stern-Gerlach experiment, for $t_{free-fall} = 25ms, t_{drop} = 30ms, G = 40G/cm$ and starting temperature $T = 4\mu$K. 132

6.2 Simulated TOF spectrum for a a Stern-Gerlach experiment, for $t_{free-fall}$ = 30 ms, t_{drop} = 25 ms, G = 40 G/cm and starting temperature $T = 4\mu$K and $\Pi_{-4} = 40\%$. 133

6.3 Representation of the lattice plane and quantization axis 133

6.4 Magnetic field gradient generated from trap coils. 134

6.5 Spectrum of a Stern-Gerlach experiment in the near-detuned lattice. 135

6.6 Spectrum of a Stern-Gerlach experiment in the far-detuned lattice showing the effects of σ^- and σ^+ optical pumping. 137

6.7 Population of different Zeeman levels versus static magnetic field, for $T_s = 2.5\mu$K , B_{fict} = 30 mG and B_{fict} = 120 mG. 142

6.8 Population of different Zeeman levels versus static magnetic field, for $T_s = 5\mu$K , B_{fict} = 30 mG and B_{fict} = 120 mG. 143

6.9 Spectrum of a Stern-Gerlach experiment in the far-detuned lattice, showing the effect of spin-polarization obtained by adding a small longitudinal magnetic field during the near-detuned lattice phase. . 145

6.10 Populations of different m_F states plotted versus the magnetic field. 147

6.11 Population ratios $\Pi_{m_F=4}$ /Π_{m_F} versus magnetic field. 148

6.12 Population distribution among the m_F states for B_Z=90 mG and estimate of B_{fict}^{min} and B_{fict}^{max}. 150

6.13 Population distribution among the m_F states for B_Z=90 mG and estimate of B_{fict} 151

7.1 Experimental setup for resolved sideband Raman cooling on a 2-D optical lattice. 157

7.2 Temperature variation versus static magnetic field along the z-axis for a sideband Raman-cooled sample of atoms for a kinetic temperature before cooling $T_{ini} = (9.0 \pm 0.2)\mu$K. 162

7.3 Population of the 2-D ground state with $n_x = 0, n_y = 0$ versus static magnetic field along the z-axis for a sideband Raman-cooled sample of atoms, for a kinetic temperature before cooling $T_{ini} = (9.0 \pm 0.2)\mu$K. 163

7.4 TOF signal of a far-detuned lattice with a kinetic temperature $T_K = (2.5 \pm 0.2)\,\mu$K. 166

7.5 Temperature variation versus static magnetic field along the z-axis for a sideband Raman-cooled sample of atoms for a kinetic temperature before cooling $T_{ini} = (2.5 \pm 0.2)\mu$K 167

7.6 Population of the 2-D ground state with $n_x = 0, n_y = 0$ versus static magnetic field along the z-axis for a sideband Raman-cooled sample of atoms, for a kinetic temperature before cooling $T_{ini} = (2.5. \pm 0.2)\mu$K. 168

CHAPTER 1

Introduction

In this chapter an overview of the basic principles of laser cooling for neutral atoms is given, with particular emphasis on Sisyphus cooling in optical lattices. The first section treats cooling processes arising from light-induced forces acting on a moving atom in the Doppler and sub-Doppler limits, as well as the magneto-optical trap configuration. In the second part of the chapter, the mechanisms of cooling and dynamics in optical lattices are presented. The optical potential and the quantum description that leads to the calculation of the vibrational bands of motion are also discussed. In the last section an overview of the known different geometries for optical lattices is given, which explores configurations in one, two and three dimensions.

1.1 Principles of laser cooling

The fundamental mechanisms of atom-light interactions are presented in this section. Radiation pressure can be used to cool moving atoms by exploiting the Doppler effect, as was first proposed by Hänsch and Shawlow in 1975 [1]. Other mechanisms of cooling are linked to the presence of polarization gradients and

lead to sub-Doppler temperatures [2], [3]. The magneto-optical trap configuration [4] is also discussed, which allows not only the cooling of the atoms but also their storage in the trapping region for a considerable time, thus allowing efficient capture of atoms and increased cooling.

1.1.1 Atom-light interaction and light-induced forces

An atom interacting with an electromagnetic field undergoes mechanical effects, due to momentum transfer during processes of absorption and emission of photons. There are two types of forces that arise from this interaction, namely the radiation pressure or scattering force and the dipole force.

Radiation pressure is generated by processes involving the absorption of photons followed by spontaneous emission. Each time an atom absorbs a photon, there is a transfer of momentum from the photon to the atom given by $\mathbf{p} = \hbar\mathbf{k}$, where $\mathbf{k}$ is the wave-vector associated with the incident light. After absorbing, the atom spontaneously emits a photon; spontaneous emission is isotropic, meaning that there is no preferred emission direction. As a result, after averaging over many cycles of photon absorbtion and emission, over a time much longer than the excited state lifetime, there will be no contribution to the net force from spontaneous emission processes. Therefore, the force resulting from multiple photon scattering processes will be $\mathbf{F} = n\hbar\mathbf{k}$, where n is the number of scattered photons per unit time. The photon scattering rate depends on the light intensity I, the detuning $\Delta = \omega_L - \omega_a$ (ω_L is the laser frequency and ω_a is an atomic resonance frequency) and the natural linewidth Γ of the transition.

If we consider a moving atom as a two-level system interacting with a pair of counter-propagating laser beams tuned to a frequency $\omega_L < \omega_a$, it can be shown [2], [3] that the net average force exerted by the light, for times $t \gg 1/\Gamma$ ($1/\Gamma$

being the lifetime of the excited level), is:

$$\mathbf{F} = \hbar\mathbf{k}\frac{\frac{\Gamma}{2}I/I_S}{1 + I/I_S + \left(\frac{2(\Delta - \mathbf{k}\cdot\mathbf{v})}{\Gamma}\right)^2}, \tag{1.1}$$

where I_S is the saturation intensity for the transition, Δ is the light detuning from the resonance frequency of the atomic transition and $\mathbf{v}$ is the atomic velocity. This is the scattering force, otherwise known as radiation pressure.

The dipole force on the other hand, originates from processes of absorption followed by stimulated emission, when a spatial gradient of the light intensity is also present. The dipole force acting on a atom in a laser field can be expressed as [2], [5]:

$$\mathbf{F} = \frac{\hbar(\Delta - \mathbf{k}\cdot\mathbf{v})}{2}\frac{\nabla I/I_S}{1 + I/I_S + \left(\frac{2(\Delta - \mathbf{k}\cdot\mathbf{v})}{\Gamma}\right)^2}. \tag{1.2}$$

Radiation pressure was exploited in the first proposal of laser cooling [1] and in the realization of optical molasses [6]. The first optical trapping was realized the following year [7], exploiting the dipole force generated by a strongly focused laser beam.

1.1.2 Doppler cooling

It is possible to exploit radiation pressure in order to create a viscous force that reduces the kinetic energy of atoms in a vapour, as suggested by Hänsch and Shawlow in 1975 [1]. Counter-propagating laser beams tuned to a frequency lower than that of an atomic resonance can be used, thus creating a viscous force that slows down the atoms along the direction of beam propagation. A moving atom is more likely to absorb a photon from the beam that is propagating in the opposite direction to its motion: the result of many cycles of absorption followed by spontaneous emission is a reduction of the atomic velocity in this direction. This configuration is called *optical molasses*, [6].

In the low intensity limit $I \ll I_S$, equation 1.1 becomes:

$$F = -\alpha v = -4\hbar k_L^2 \frac{I}{I_S} \frac{2\Delta/\Gamma}{[1 + (2\Delta/\Gamma)^2]^2} v \tag{1.3}$$

where Δ is the detuning from the atomic resonance, Γ is the lifetime of the excited state and I_S is the saturation intensity (for caesium, which is the atomic species used in the work described in this thesis, $I_S = 1.12$ mW/cm^2) and v is the velocity component along $\mathbf{k}_L$. The resulting force is a viscous force that tends to slow down the atoms in the direction of propagation of the beams, thus reducing their kinetic energy. The cooling is limited by spontaneous emission processes; due to spontaneous emission, at short times the viscous force fluctuates around its average value, given by equation 1.3. The balance between the heating process and the cooling is studied in [2], [3] where it is shown that the minimum achievable temperature in the Doppler limit is reached when $\Delta = \Gamma/2$ and it is given by:

$$T_{min} = \frac{\hbar\Gamma}{2k_B}. \tag{1.4}$$

For caesium the minimum temperature is $T_{min}^{Cs} = 125$ μK, which corresponds to an atomic rms velocity $v_{rms} = 9$ cm/s. The minimum kinetic energy achievable is therefore limited by the width of the transition used for the cooling process.

1.1.3 The magneto-optical trap

The atomic density achievable in an optical molasses is very low because of the atoms' diffusive motion; even atoms with very small velocity escape from the laser interaction region after a short time. In 1986, Pritchard [4] implemented a scheme, first suggested by Dalibard, which required the use of a spatially non-uniform, magnetic field and counter-propagating laser beams of opposite circular polarization with detuning $\Delta < 0$ in order to exploit the internal atomic structure to provide a restoring force towards the center of the trap as well as a viscous force. It is thus possible to confine and cool a sample of atoms starting from a gas

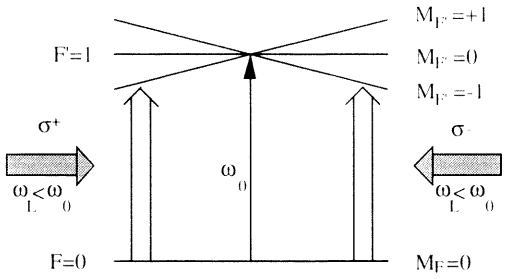

Figure 1.1: Scheme of a magneto-optical trap in 1-dimension for a $F = 0 \rightarrow F' = 1$ transition.

at room temperature using the scheme in [4], which employs counter-propagating laser beams with a detuning $\Delta < 0$ from an atomic resonance and opposite circular polarization $\sigma^+ - \sigma^-$. A hyperfine transition $F = 0 \rightarrow F' = 1$ is selected and an inhomogeneous magnetic field is also added which is null at the trap center and increases linearly moving away from zero point.

As is shown in figure 1.1 for an F=0 to F'=1 transition, the effect of the inhomogeneous magnetic field is to generate a Zeeman-splitting of the levels that is spatially dependent: thus the σ^+ polarized beam is more likely to be absorbed by an atom moving in the opposite direction (because the Zeeman splitting produced by the magnetic field brings the $M_F = -1$ closer to resonance), while the probability for it to interact with an atom moving in the same direction is reduced. The Zeeman splitting is such that the more distant an atom is from the center of the trap, the more the transition is brought in resonance with the beam which is propagating in the opposite direction. In this way, it is possible to generate, as shown in [2], [3], a force acting on the atoms which is the sum of a viscous force that cools the atoms and a confining force. This opens up the possibility of obtaining higher densities of trapped atoms as well as a more efficient cooling process arising from longer interaction times between the atoms and the laser beams. It is shown in [2], [3] that this force can be generated along three spatial dimensions with the use of three pairs of counter-propagating laser beams $\sigma^+ - \sigma^-$ polarized

and a quadrupole magnetic field.

1.1.4 Sub-Doppler cooling

In 1988 temperatures lower than the Doppler limit were reported in optical molasses [8], [9]. These gave evidence that other kinds of mechanisms were also involved in cooling. New theories were developed [5], [10], which explained the observations of temperatures below the Doppler temperature. It was found out that new cooling mechanisms were indeed involved, arising from the degeneracy of the ground level involved in the optical transition and from optical pumping, between different Zeeman sub-levels associated with the polarization gradient, generated by the laser beams.

Let us consider the case of a 1-dimensional optical molasses. It was discovered in [5], [10] that two new cooling phenomena occur, depending on the polarization configuration of the laser beams:

i) two counter-propagating laser beams with opposite circular polarization ($\sigma^+ - \sigma^-$) lead to *motion induced orientation effect*;

ii) two counter-propagating laser beams with orthogonal linear polarization ($\pi^x - \pi^y$) lead to *Sisyphus Cooling*;

The first of the two mechanisms is linked to a radiation pressure imbalance. A moving atom interacting with two counter-propagating $\sigma^+ - \sigma^-$ polarized laser beams, experiences a population imbalance among the sub-levels of its ground state that depends on position, giving rise to an imbalance of the radiation pressure which results in further cooling. In the second case (polarization $\pi^x - \pi^y$), the polarization of the optical field varies along the z-axis. Therefore different transitions (i.e. with distinct Clebsch-Gordan coefficients) between Zeeman sub-levels are favoured, depending on the position. Consequently, the light-shift of the Zeeman sub-levels becomes spatially modulated. Optical pumping processes

occurring in this modulated potential lead to so-called *Sisyphus cooling*. It has been proved [5], [10] that in both cases the minimum temperature achievable in the low saturation limit is proportional to the ratio $\frac{I}{\Delta}$.

In the following I will discuss Sisyphus cooling in detail, as optical lattices are designed to exploit Sisyphus cooling in order to achieve localization, by carefully choosing the laser beams polarization. I will also refer briefly to motion induced orientation as well, as in higher dimensions molasses and MOT, both kinds of cooling mechanisms are present.

1.1.4.1 Motion induced orientation effect

Two counter-propagating laser beams with opposite circular polarization generate a field with a resultant linear polarization that rotates around the z-axis (see figure 1.2). The polarization gradient interacting with the moving atom induces

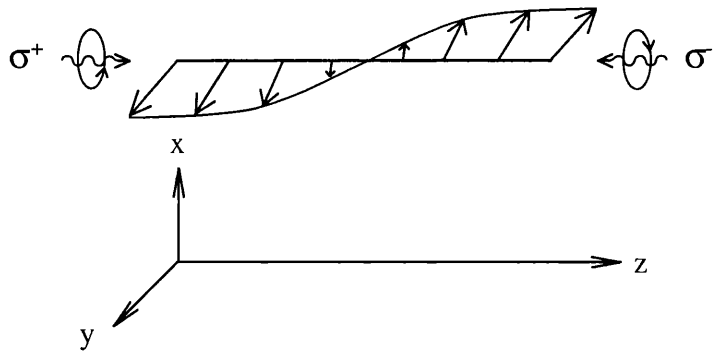

Figure 1.2: Representation of the $\sigma^+ - \sigma^-$ polarized optical molasses configuration which gives rise to a rotating linear polarization.

an atomic orientation and an imbalance between the ground state sub-levels (see figure 1.3 for an $F = 1$ ground state) and leads to a bigger probability for the atom to absorb photons from the beam that is propagating in the direction opposite to its velocity, which results in cooling. It can be shown [5], [10] that in the sub-

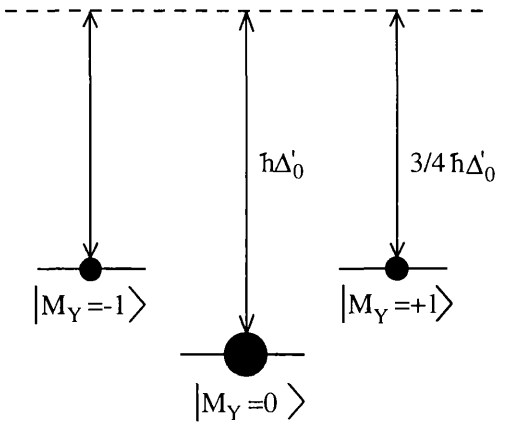

Figure 1.3: Induced orientation effect, which shows an increased population on one of the ground state sub-levels (this case is for an $F = 1$ ground state).

Doppler limit the minimum temperature achievable is given by:

$$k_B T_{sub-Dop} \propto \frac{\hbar\Omega^2}{\Delta}, \tag{1.5}$$

where $\Omega = \Gamma\sqrt{\frac{I}{2I_S}}$ is the Rabi frequency associated to the field and Δ is the detuning. The minimum achievable temperature is very close to the one-photon recoil energy limit.

1.1.4.2 Sisyphus cooling for an atomic configuration with $F_g = 1/2$

The configuration $\pi^x - \pi^y$ (i.e. the two counter-propagating laser beams have orthogonal linear polarization) gives rise to an ellipticity gradient along the z-axis, as shown in figure 1.4. The polarization changes from linear to σ^-, to linear, to σ^+ and so on, along $z-$axis. This leads to a spatial modulation of the light shift of the ground states sub-levels, as shown in figure 1.5, the distance between adjacent locations of pure σ^- and σ^+ light being $\lambda/4$, where λ is the optical wavelength.

Figure 1.5 refers to an atom with a ground state with hyperfine number $F_g = 1/2$ and an excited state with $F_e = 3/2$. This is the simplest situation to describe Sisyphus cooling but does not fully account for the cooling mechanism operating for atoms with large F. For atoms with $F \geq 1$ there is the possibility of cooling

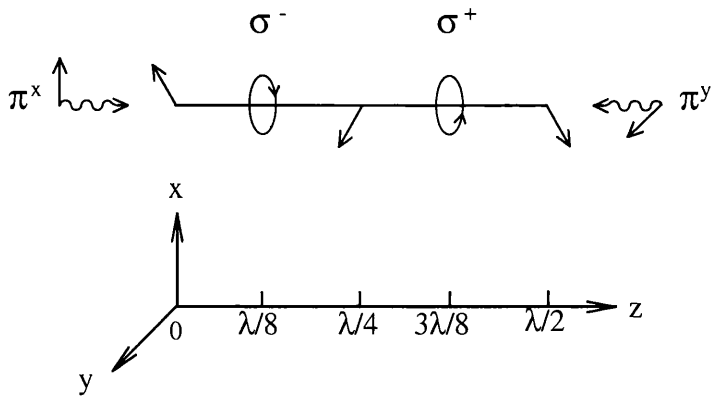

Figure 1.4: Representation of the linear-orthogonal-linear polarization optical molasses configuration, which gives rise to an ellipticity gradient.

caused by optical pumping between different light-shift surfaces at a single well-site, which is not allowed for $F = 1/2$, as each lattice site presents only one light-shift surface. After discussing the $F_g = 1/2$ case I will extend the treatment to atoms with large F_g.

If an atom has almost zero velocity and it is placed at a location of σ^+ light, it will be optically pumped to an $|m_F = 1/2\rangle$ state. The energy levels of the atom will also experience a light shift. Since the Clebsch-Gordan coefficient is larger for the $m_{F_g} = 1/2 \rightarrow m_{F_e} = 3/2$ than for the $m_{F_g} = -1/2 \rightarrow m_{F_e} = 3/2$ transition for σ^+ exciting light, then the ground state sub-level with $m_{F_g} = 1/2$ will experience a larger light shift. The opposite is true at σ^- locations.

When the atoms are moving along the axis of the laser beams with velocity $v \neq 0$, they experience a spatially varying polarization. This means that the two ground state magnetic sub-levels will present a varying light shift along the $z-$axis. As the atoms move from a pure σ^+ point of light towards a point of σ^- light, the probability of being optically pumped to $m_F = -1/2$ increases, and reaches a maximum at locations of pure σ^- light; when the atom in the $m_F = 1/2$ state climbs the potential hill, figure 1.5, and approaches its top, it will be optically

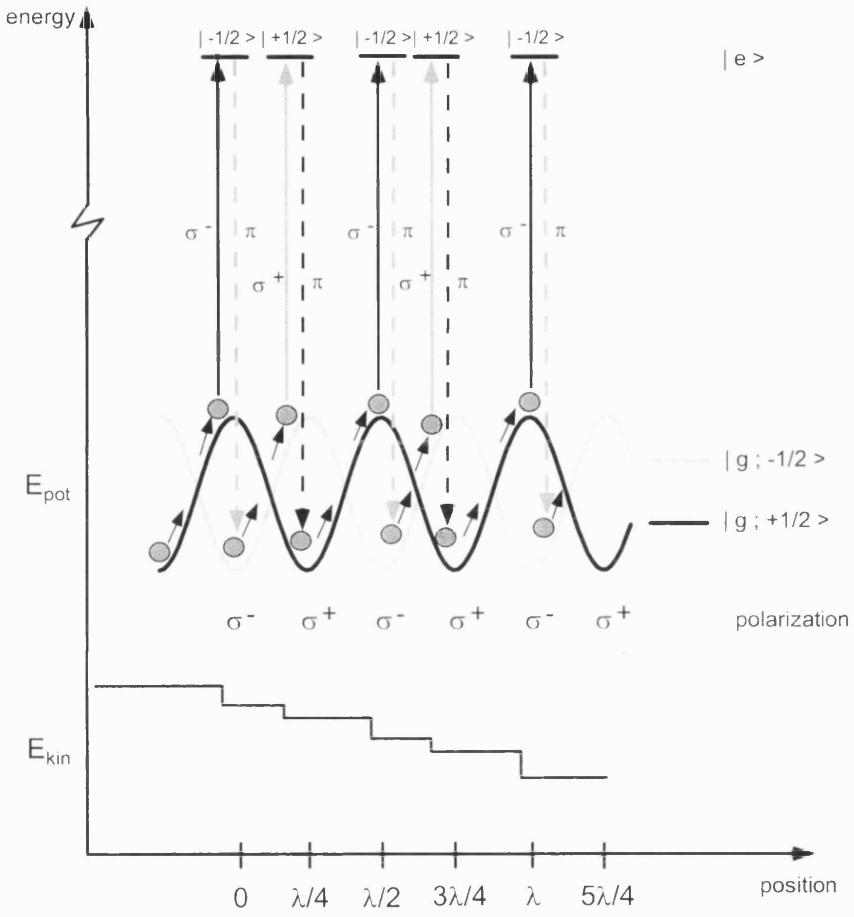

Figure 1.5: Semiclassical picture for the Sisyphus cooling on a $F_g = 1/2 \rightarrow F_e = 1/2$ transition. The atoms are shown to climb potential hills before being optically pumped back at the bottom of the potential well, thus loosing kinetic energy.

pumped to $m_F = -1/2$ and will thus lose kinetic energy. So at the end of the cycle the atom is optically pumped again into a 'valley' of the potential, from where, if it has still enough kinetic energy, it can start climbing again and the process would be repeated. The net result is a dissipation effect related to anti-Stokes Raman processes, driven by the optical pumping. These processes are most efficient when the velocity of the atom is such that $v\tau_p = \lambda/8$, where λ is the wavelength of the laser field and determines the periodicity of the potential (see figure 1.5) and τ_p

is the optical pumping time: this means that when the velocity of the atom is such that the atom moves over a distance $\lambda/4$ during an optical pumping time, the cooling is more efficient. The temperature limit in the Sisyphus case can be estimated, as shown in [2] from:

$$k_B T_{Sys} \sim \hbar \frac{\Omega^2}{|\Delta|}. \tag{1.6}$$

This result predicts that an arbitrarily low temperature can be reached since decreasing the laser intensity and increasing the detuning leads to a lower temperature. Of course the temperature cannot decrease indefinitely, as at some point, the loss of energy during each cooling cycle would be balanced by the recoil energy gained in the spontaneous emission step. The lower limit for intensity determines the minimum temperature achievable, which is of the order of E_R/k_B, where $E_R = \frac{(\hbar k)^2}{2m_{Cs}}$ is the one-photon recoil energy.

1.1.4.3 Sisyphus cooling for an atomic configuration with $F_g \geq 1$

Sisyphus cooling provides cooling and localization of atoms in *optical lattices*, in which each lattice site is associated with a minimum light shift of one or more ground state sub-levels, depending on the F_g number. For a total ground state angular momentum F=1/2, Sisyphus cooling involves optical pumping among states $m_F = 1/2$ and $m_F = -1/2$, which have minima of light shift at different locations. For ground state with $F_g > 1$, more than one sub-level present a minimum of the light-shift at the same location (lattice site), therefore cooling can also happen locally, without hopping between lattice sites.

For an atom with ground state of hyperfine number $F_g > 1$ and excited state $F_e = F_g + 1$ moving within an optical lattice, there is a set of optical potentials associated with the $F_g + 1$ ground states, which are coupled by stimulated Raman transitions. For such atoms there are two possible pictures to describe the mechanisms of cooling, as reported in [11]. In one case, cooling can occur

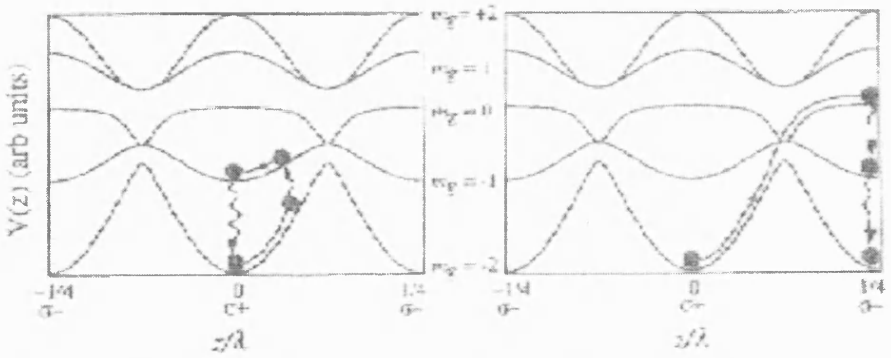

Figure 1.6: Semiclassical picture for the Sysiphus cooling on a $F_g = 2 \rightarrow F_e = 3$ transition. a)represents local cooling, due to optical pumping at a given lattice site and b) hopping cooling, motional induced coupling causes transitions between the adiabatic potentials and atoms are pumped between different lattice sites. Figure from PRA 56, 1705

locally at a given lattice site as atoms preferentially climb steep potential wells and descend shallow ones. As shown in figure 1.6 the two potentials among which cooling happens have different curvature, thus the atoms lose more kinetic energy in climbing than they gain in descending, the difference in energy being dissipated in optical pumping. In the second case, shown in figure 1.6b, atoms cool when they hop between lattice sites, by making non-adiabatic transitions between the coupled set of optical potentials and preferentially being pumped to the potential with the largest light shift. In [11] theoretical studies for the $F_g = 2 \rightarrow F_e = 3$ transition of these cooling mechanisms lead to the conclusion that, although there is some local cooling, the dominant mechanism is cooling with inter-well hopping, with a rate twice as large. Local cooling is expected to be more efficient for atoms with large F, since the larger the F, the more internal states for which local cooling would work become available. In [12] distinct cooling and magnetization decay times were measured for a 1-D optical lattice of caesium atoms cooled on the $F_g = 4 \rightarrow F_e = 5$ transition; the magnetization characteristic time was found to be three times longer than the localization time. The distinct nature of these timescales is a clear signature of local cooling. In [13] the build up of the

localization was measured to take of the order of few microseconds.

1.2 Introduction to optical lattices

Atoms can be cooled and trapped in a periodic lattice of potential wells generated by interfering laser beams. The atoms trapped in these lattices are to a large extent isolated from environmental disturbances and from each other, due to the low filling factor (i.e. fraction of lattice sites populated) characteristic of such lattices. The richness and flexibility inherent to the atom-light interaction allows a wide range of properties characterizing an optical lattice to be adjusted [14] through the geometry of the laser beams, their polarization, intensity and frequency and through the addition of static electric and magnetic fields. Furthermore the possibility of dynamically altering the lattice properties can be exploited and many different experiments can be performed [15]. Experiments devised in the past suggested that these properties must be carefully chosen in order to provide efficient Sisyphus cooling, which only occurs for configurations where light is circularly polarized at positions of maximum light shift.

In this section I will give an introduction to optical lattices. I will describe the methods for treating laser cooling in optical lattices and the quantum treatment that leads to the band theory. I will then present a summary of some possible different configurations extensively discussed in [14]. In particular I will discuss the 2-dimensional configuration used extensively for the experiments performed in the course of this work.

1.2.1 Laser cooling in optical lattices

Many theoretical models have been used for the study of laser cooling in optical lattices and in this section I will highlight the principal methods and results achieved, referring in particular to the Jessen and Deutsch paper of 1998 [16] and

to [17].

The general theory of laser cooling for a multilevel atomic system is discussed in detail in [2] and the main results will be summarized here. Consider a monochromatic optical field which is interacting with a gas of atoms, being tuned close to an atomic transition of ground state $|F_g\rangle$ and excited state $|F_e\rangle$. There are, therefore, $2(F_e + F_g + 1)$ states that evolve coherently through the coupling to the laser field and dissipatively through the coupling to the vacuum. The full description of the system would, in general, be very complicated. However, in the limit of low intensity or large detuning, which also represent the regime where cooling is most efficient, the problem can be simplified. In this regime, the saturation parameter is small and the population of the excited state is consequently small. This means that the time scales of spontaneous emission and optical pumping can be separated, the first being much shorter than the second. Therefore, the excited state population and atomic coherence between ground and excited state relax rapidly and the atoms adiabatically follow the evolution of the ground state manifold. The excited state can then be eliminated and a simplified Hamiltonian can be considered, that acts only on the atom's external coordinates and internal ground state manifold, as discussed in [17]. The reduced Hamiltonian then becomes:

$$H = \frac{\mathbf{P}^2}{2M} + U_0 \left(\epsilon_L(\mathbf{x}) \cdot \hat{\mathbf{d}}\right)^\dagger \left(\epsilon_L(\mathbf{x}) \cdot \hat{\mathbf{d}}\right), \tag{1.7}$$

where $\mathbf{P}$ and $\mathbf{x}$ refer to the center of mass, $\hat{\mathbf{d}} = \sum_{q,m_g} c_{m_g}^{m_g+q} |e, F_e, m_g+q\rangle\langle g, F_g, m_g| \mathbf{e}_q^*$ is the dipole operator, $c_{m_g}^{m_e}$ is the Clebsch-Gordan coefficient coupling the states $|F_g, m_g\rangle$ and $|F_e, m_e\rangle$ and $\mathbf{e}_q$ are the spherical basis vectors.

When the 2-D lattice is formed by beams with all polarization vectors lying in the same plane, choosing the quantization axis normal to the plane, the light field can be decomposed into $\sigma^\pm$ components only. In the very simple case of a $F_g = 1/2 \rightarrow_e F = 3/2$ transition, the $m_g = \pm 1/2$ states are not coupled by the laser field; this means that the coherent atomic motion can be considered as taking

place on two separate scalar potentials, one corresponding to a $m_g = 1/2$ and one to a $m_g = -1/2$ state. For a transition $F \rightarrow F + 1$ with $F \geq 1$, the light shift operator contains both diagonal and off-diagonal terms in the $|g, F_g, m_g\rangle$ basis. The diagonal terms correspond to absorption and stimulated emission processes with $\Delta m_g = 0$ while the off-diagonal ones have $\Delta m_g = \pm 2$. Neglecting off-diagonal elements we obtain the 'diabatic' potentials; if the total light shift operator is diagonalized the 'adiabatic' potentials are obtained, which correspond to light shift eigenvalues of an atom localised at a particular position. The diabatic and adiabatic potentials are both shown in figure 1.7 for a $F_g = 2 \rightarrow F_e = 3$ transition.

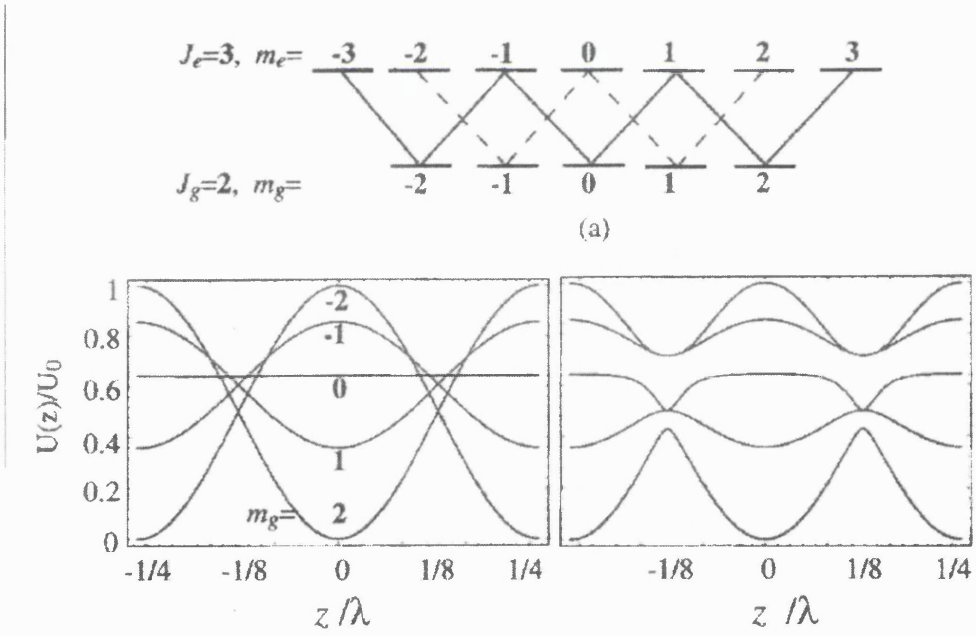

Figure 1.7: a) level structure of a $F_g = 2 \rightarrow F_e = 3$ atom. Lower left: diabatic potential obtained ignoring coupling between different m_F states. Lower right: adiabatic potential obtained considering coupling $\Delta m_g = \pm 2$. Figure from Adv. At. Mol. Opt. Phys. 37, 1996

In general neither of the two representations completely describes the situa-

tion pertaining in near-detuned optical lattices. For slow moving atoms, the time spent in the crossing region of the adiabatic potentials is long enough to allow stimulated Raman transitions, so that the atom motion follows the adiabatic potential, while fast moving atoms follow the diabatic potentials. When the atoms are strongly localized at the bottom of the potential well, the two potentials are almost identical.

Equation 1.7 describes the coherent evolution of an atom, but in order to treat laser cooling, dissipative processes must be added. If the excited state is adiabatically eliminated, then the master equation for the atomic density operator ρ can be written as [17]:

$$\frac{d\rho}{dt} = \frac{1}{i\hbar}[H,\rho] - \frac{1}{2}\Gamma_s\{\Lambda,\rho\} + \Gamma_s \sum_h \int d^2\mathbf{k}_S N_h(\mathbf{k}_s)\left(W_h(\mathbf{k}_s)\rho W_h^\dagger(\mathbf{k}_s)\right) \quad (1.8)$$

The first term just represents the coherent evolution of the system, ruled by the Hamiltonian of equation 1.7. The second and third terms represent the dissipative processes linked to optical pumping between ground-state sublevels. The second term describes the population decay from one ground state sublevel, due to optical pumping into other sublevels and $\Lambda = (\boldsymbol{\epsilon}_L(\mathbf{x})\cdot\hat{d})^\dagger(\boldsymbol{\epsilon}_L(\mathbf{x})\cdot\hat{d})$. The third term represents the transfer of population to the ground state sublevel from other sublevels by optical pumping. The operator $W_h(\mathbf{k}_s) = (e^{i\mathbf{k}_s\cdot\mathbf{x}}\mathbf{e}_h\cdot\hat{d})^\dagger(\boldsymbol{\epsilon}_L(\mathbf{x})\cdot\hat{d})$ rules the absorption processes of a lattice photon, followed by emission of a fluorescence photon with a specific wave-vector $\mathbf{k}_s$ and helicity h with respect to the quantization axis. $N_h(\mathbf{k}_s)$ is the probability distribution of photons with helicity h and wave vector $\mathbf{k}_s$ and Γ_s is the scattering rate. Equation 1.8 can be rewritten in units of the recoil energy E_R, so that it is dependent only on two dimensionless parameters:

i) $\overline{U_0} = \frac{U_0}{E_R}$; it defines the timescale for coherent evolution processes (i.e. oscillation time at the bottom of the potential well)

ii) $\overline{\Gamma_s} = \frac{\hbar\Gamma_s}{E_R}$; it defines the timescales for dissipative optical pumping

The solution of equation 1.8 is in general not trivial, but it can be obtained if some simplifications are made, as detailed below. In the *semiclassical* approximation the coordinates of the center of mass are treated as classical variables; this can be assumed if the spread in Doppler shift, due to the width of the momentum distribution, is small compared to the natural linewidth and when the spatial coherence of the atomic wave-function is small compared to that of the light wavelength. The relaxation time-scale for internal degrees of freedom must be shorter than for external degrees of freedom, so that the atom can be seen as a classical particle subject to an instantaneous force. When the internal timescale becomes much longer than the external one, then a quantum treatment is required, as I will discuss in the following section.

1.2.1.1 Quantization of the atomic motion and band theory

For multilevel atoms in an optical lattice the semiclassical approximation is not applicable, because the internal timescale τ_{int} is typically much longer than the external one τ_{ext} (*oscillating regime*). In this case a full *quantum* treatment is required, in which the external coordinates $(\mathbf{x}, \mathbf{P})$ also have to be treated as quantum operators. The spectrum of energy eigenstates consists of bands, with bandgaps separating the tightly-bound states, and a quasi-continuum spectrum for free states. In the oscillating regime, laser cooling can be studied by diagonalizing the atom-laser Hamiltonian and treating the vacuum as a perturbation. The problem is analogous to the description of an electron moving in the periodic potential formed by ions in a solid crystalline structure. The difference is mainly due to the fact that the optical potential depends strongly on the internal state of the atom and because, in general, internal and external degrees of freedom are not separable. The eigenstates are then 'entangled' states of these variables. Generally, it is

possible to write the state of the atom as a $2F_g + 1$ component spinor. Each wave function can then be expressed in Bloch form as $|\psi\rangle = \sum_{m_g} e^{i\mathbf{q}\cdot\mathbf{x}}|u_q^{m_g}\rangle \otimes |m_g\rangle$, where $|u_q^{m_g}\rangle$ has the periodicity of the lattice. Results of band calculations for a far-detuned optical lattice are shown in the following chapter in figures 2.5 2.6, 2.3 and 2.4. The energy bands shown there exhibit curvature for higher energy states. This curvature arises because, in a lattice with $F_g \geq 1$, atoms can tunnel between neighboring wells associated with opposite light polarization. The band curvature becomes substantial as soon as the energy rises above the top of the lowest adiabatic potential well, but such bands do not have a completely free particle character.

1.2.2 Optical Lattice in one dimension

The simplest possible configuration for an optical lattice is in one dimension for an atomic transition with ground state $F_g = 1/2$ and an excited state with $F_e = 3/2$, as described in [17]. A standing wave is formed by a pair of linear cross-polarized laser beams, in the scheme represented in figure 1.4. This configuration is usually referred to as 1-D lin⊥lin. Choosing the quantization axis $\hat{z}$ along the direction of propagation of the beams, the total light field can be decomposed into two standing waves of σ^+ and σ^- polarization, with a spatial offset of $\lambda/4$, so that the antinodes of one coincide with the nodes of the other. The polarization of the total field changes along $\hat{z}$ from circular to linear (via elliptical) and back to circular, while the total intensity of the light is independent of z. In [5] the potentials for the states $F_g = \pm 1/2$, in the limit of low saturation, are given by:

$$\begin{aligned} U_{1/2} &= \frac{2}{3}U_0 \cos^2(kz) + \frac{1}{3}U_0 \\ U_{-1/2} &= \frac{2}{3}U_0 \sin^2(kz) + \frac{1}{3}U_0, \end{aligned} \tag{1.9}$$

where $U_0 = \frac{\hbar \Delta s}{2}$ is the maximum value of the light shift; the saturation itself is defined in terms of the parameter $s = 2\Omega^2/(4\Delta^2 + \Gamma^2)$, for the transition involved

at points of pure circular polarization, with Rabi frequency Ω. In the case of red detuning, this potential is represented in figure 1.5, where it is shown that the cooling occurs because of optical pumping between the atomic ground state sublevels, a mechanism that is called Sysiphus cooling and it is further described in section 1.1.4.2. In [5], [2] a semiclassical model is used to predict the temperature of atoms in an optical lattice, by estimating the averaged friction and diffusion coefficient. Atoms reach a temperature that corresponds to a mean kinetic energy which is of the order of magnitude of the depth of the potential, which means that a large fraction of the atoms can be trapped in individual potential wells. Near the bottom of the potential well, the atoms are localized in the Lamb-Dicke regime. In this regime the atomic center-of-mass motion can be approximated by a thermally excited harmonic oscillator. By expanding the optical potential around the minimum and taking the quadratic term in the displacement, it is possible to define the oscillation frequency

$$\hbar\omega_{osc} = K_{geom}\sqrt{U_0 E_R}, \tag{1.10}$$

where $E_R = \frac{\hbar^2 k^2}{2M}$ is the recoil energy of one photon and K_{geom} is a constant, which depends on the geometry of the lattice; in the 1-D lin$\perp$lin case this is $2\sqrt{2/3}$. Again, this treatment is meaningful only if the atom resides in a given potential well for a time comparable to or larger than the inverse of the vibrational frequency.

1.2.3 Optical lattices in two and three dimensions

1.2.3.1 2-D Optical lattice

It was suggested in 1993 by Grynberg et al. that it is not necessary to phase-lock the lasers in order to keep the topography of the lattice constant, provided that in order to generate an N-dimensional optical lattice, $N + 1$ beams are employed. Fluctuations of the N independent relative phases would then simply result in a

spatial translation of the lattice. Typically, the fluctuations of the relative phases are slow compared to the atomic response time, so that the atoms adiabatically follow the lattice translations. In figure 1.8 two possible configurations for the

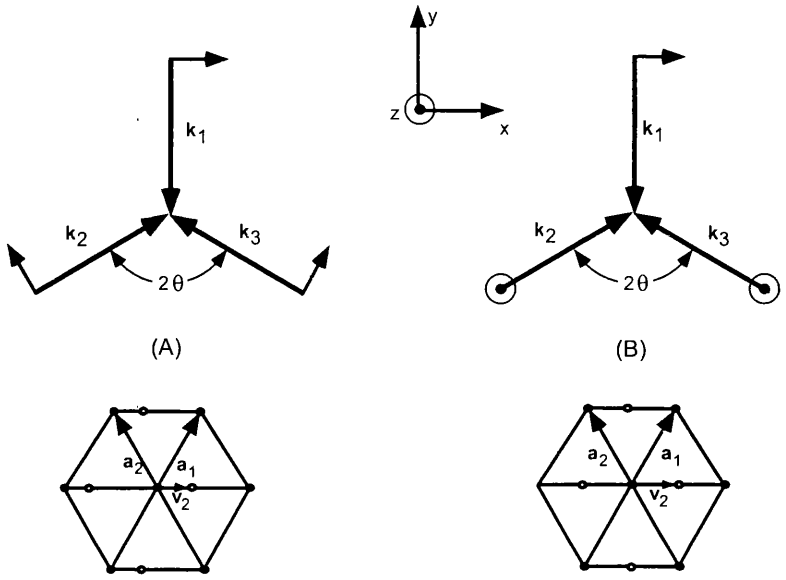

Figure 1.8: Two dimensional optical lattice configurations for $\theta = \pi/3$, with (A) all the beams polarizations lying on the lattice plane and (B) one of the beams polarization lying on the lattice plane and the two other orthogonal to the lattice plane.

2-D case (Grynberg [14]) are shown. Assuming $\theta = \pi/3$, as shown in the figure, the primitive cell is spanned by $\mathbf{a}_1 = (\pi/K_x)\hat{x} + (\pi/K_y)\hat{y}$ and $\mathbf{a}_2 = -(\pi/K_x)\hat{x} + (\pi/K_y)\hat{y}$, where $K_x = k\sin\theta$ and $K_y = k(\cos\theta + 1)$, k being the wave-number.

Different polarization choices in the two geometries change the relative position of σ^+ and σ^- sites, i.e. the basis of the unit cell. For configuration (A), the positive frequency component for the electric field is given by:

$$E_L(\mathbf{x}) = \frac{E_0 e^{-iky}}{\sqrt{2}}\left[-\mathbf{e}_+(1 + 2e^{iK_y y}\cos(K_x x)) + \mathbf{e}_-(1 + 2e^{iK_y y}\cos(K_x x - 2\theta))\right], \tag{1.11}$$

where the quantization axis is $\hat{\mathbf{z}}$, being perpendicular to the $x - y$ plane, and the relative phases are chosen such that there is a local maximum of the σ^+ polarized

component at the origin. A basis associated with each primitive cell consists of a σ^+ site at $\mathbf{v}_1 = 0$ (black dot) and σ^- site at $\mathbf{v}_2 = (2\theta/K_x)\hat{\mathbf{x}}$ (white dot).

For configuration (B), in figure 1.8, in order to obtain maximum light shift at points of pure σ polarization, it is necessary to choose different amplitudes for the three plane waves, $E_2 = E_3 = E_1/2$ (E_1 being the beam travelling along the y axis), and a convenient relative phase. The electric field in this geometry is then given by:

$$E_L(\mathbf{x}) = \frac{E_0 e^{-iky}}{\sqrt{2}} \left[-\mathbf{e}_+(1 + 2e^{iK_y y}\cos(K_x x)) + \mathbf{e}_-(1 + 2e^{iK_y y}\cos(K_x x))\right] \tag{1.12}$$

In this case, the quantization axis is chosen in the $x - y$ plane along $\mathbf{k}_1$. From equation 1.12 we can see that the basis of the primitive cell has σ^+ at $\mathbf{v}_1 = 0$ and σ^- at $\mathbf{v}_2 = (\pi/K_x)\hat{\mathbf{x}}$.

This second configuration has pure circular polarization at positions of maximum light shift for an arbitrary angle θ, while in geometry (A) this requirement was only fulfilled choosing an angle of $\theta = \pi/3$. But, because of the intensity imbalance of the three laser beams, the potential of configuration (B) presents a non-zero radiation pressure at the potential minima, making it less suitable for cooling and trapping than the potential of configuration (A).

1.2.3.2 3-D Optical Lattice

The discussion in the above two-dimensional case can be generalized also to three spatial dimensions. In order to create a lattice in N dimensions, N+1 laser beams should be used to achieve a constant topology. If more beams are used, they have to be phase locked. In the following, I discuss an example of a 3D lattice, generated by four beams, which can be viewed as a three dimensional extension of the 1D lattice discussed above, [14]. Let us start again with the one dimensional lattice, formed by two opposing beams with crossed linear polarization along the

$z-$axis. One of the two beams is split, in order to get two beams in the $x-z$ plane with equal intensities and linear polarizations along the $y-$axis. The other beam is split into two beams lying on the $z-y$ plane, with linear polarizations along the $x-$axis. The total field will generate a periodic potential with points of pure σ^+ and σ^- light; at these points all beams contribute with equal intensity and therefore the net radiation pressure is zero. This structure, shown in figure 1.9, gives rise to a simple tetragonal lattice. In [14] this configuration as well as other possible ones are studied; it is shown that, by changing the geometry and number of laser beams, one can construct other types of unit cells, such as face-centered-cubic and body-centered-cubic.

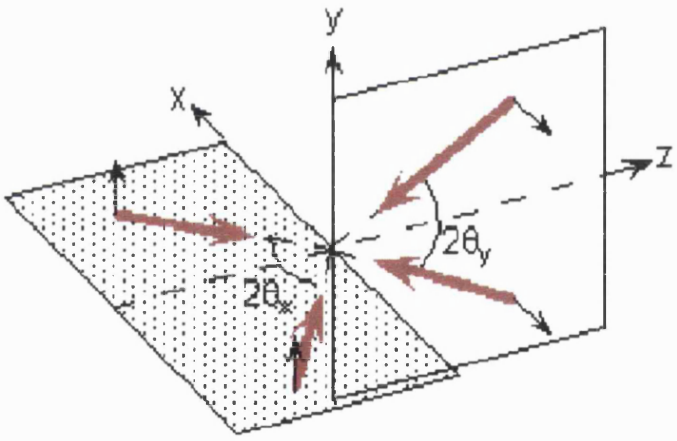

Figure 1.9: Three dimensional tetragonal optical lattice configurations generated with four beams.

1.3 Aims of this thesis and outline

Optical lattices induced by light detuned far from the frequency of an atomic resonance transition are ideal systems in which to develop techniques for the coherent control of atomic motional and internal states. They provide conservative poten-

tials, which can be engineered in order to achieve a wide variety of forms, through a careful choice of the geometry and polarization configuration of the optical field and the strength and orientation of supplementary static magnetic fields. Furthermore the decoherence arising from spontaneous emission can be suppressed to a high degree. The atoms trapped in such lattices are to a large extent isolated from environmental disturbances and from each other. The first step towards coherent control of atoms in a far-detuned lattice is their preparation in a single motional state.

In this thesis an extensive study of atoms in a 2-D non-dissipative optical lattice is presented. The main goal of the thesis is to achieve two-dimensional cooling of the atomic sample via resolved-sideband Raman-cooling. In this way the atoms can be prepared in the ground vibrational state of the light-shift potential surface corresponding to a single Zeeman sub-level. This is an ideal starting point for coherent control, as it is a minimum uncertainty state.

An understanding of the properties of the lattice is gained through theoretical modelling of the potential light-shift and band structure. A two-dimensional scheme for resolved-sideband Raman-cooling [18] is also modelled; these calculations offer us the possibility of estimating *a priori* the optimum parameters for the loading of the lattice and the Raman-cooling of the sample.

The loading of the far-detuned optical lattice is monitored and a series of experiments are run aimed at the optimization of the transfer of atoms from a super-imposed, near-resonance lattice. Experimental techniques are implemented in order to measure the population of vibrational bands and Zeeman states. These techniques are used in order to monitor and optimize the transfer of atoms, by ensuring that the increase in vibrational temperature during the transfer is minimized and that the maximum population in the desired stretched state is achieved. The possibility of resolving the populations of the single bands is also exploited

in order to study the mechanisms of loss in the far-detuned lattice and the effects of noise or spontaneous-scattering induced heating in the far-of-resonance lattice (chapter 4). Stern-Gerlach experiments (chapter 6) are used to monitor the population in the distinct Zeeman levels and to maximize the population of the $|m_F = -4\rangle$ state, in which the Raman cooling becomes efficient. Furthermore, this technique is employed for a study of the magnetization properties of the lattice as well as the spin-temperature of the ensemble of atoms in the lattice. In chapter 6 a thorough analysis of the variation of the Zeeman states' population as a function of a static magnetic field orthogonal to the lattice plane allows an investigation of the paramagnetic properties of the lattice and the determination of a spin temperature.

In chapter 5, experiments on parametrically excited atoms in the lattice, compared to simulations, allow us to investigate the heating induced by laser intensity fluctuations. Parametric excitation experiments and simulations permit also a study of the vibrational frequencies of the far-detuned lattice and allow the matching of the near-detuned vibrational frequency to the far-detuned one. Furthermore, a second order perturbation method, allows the investigation of the high degree of anharmonicity and of the non-uniformity of the potential depth along the trapping sites.

Following the optimization of the loading of atoms in the far-detuned lattice, sideband-Raman cooling experiments are performed, aimed at the preparation of atoms in a single motional state. Two-dimensional sideband Raman cooling is finally achieved (chapter 7), using a method first proposed by Jessen and Deutsch [18]. The method is based on coherent coupling, due to stimulated Raman transitions induced by the lattice field, with an irreversible step due to optical pumping.

CHAPTER 2

Non-Dissipative Optical Lattices

The spontaneous scattering of photons, which is an inherent part of the Sisyphus cooling that leads to localization of atoms in a near-detuned lattice, has the disadvantage of being responsible for decoherence effects and thus for a reduced lifetime of the vibrational coherences. While the spontaneous scattering rate is proportional to $\frac{I}{\Delta^2}$, the potential depth is proportional to $\frac{I}{\Delta}$. It is therefore possible to reduce the scattering rate by tuning the lattice light field very far from an atomic resonance (far-detuned regime), while keeping the potential depth constant by adequately increasing the intensity. The scattering rate can therefore be reduced from a typical value of $\Gamma_s = 500$ kHz in the near-detuned lattice to only $\Gamma_s \simeq 100Hz$ in the far-detuned optical lattice, while maintaining the vibrational frequency typically $\omega_{vib} = 40KHz$ in both cases. In this way we generate a far-detuned lattice, an almost dissipation-free potential, with longer-lived vibrational coherences.

In this chapter an in depth discussion of optical lattices in the far-detuned regime is offered. The form of the optical potential which may readily be accounted for using the concept of effective magnetic field presented in section 1. Section 2 details the calculation of the band-structure for our 2D lattice configuration

and presents results for a variety of potential depths. The last section of the chapter is entirely dedicated to a sideband-Raman-cooling scheme, first realized by Hamann et al. in 1998 [20], which was used to increase the population of the ground vibrational state over that obtainable by Sisyphus cooling alone in a near-resonant lattice.

2.1 Optical potential in the far-detuned regime and fictitious magnetic field

The potential for atoms in the ground state manifold interacting with a laser field is given by [18]:

$$\hat{U}(\mathbf{x}) = -\mathbf{E}_L^*(\mathbf{x}) \cdot \hat{\alpha} \cdot \mathbf{E}_L(\mathbf{x}) \tag{2.1}$$

where $\mathbf{E}_L$ is the electric field, $\hat{\alpha} = -\sum_e \hat{\mathbf{d}}_{ge}\hat{\mathbf{d}}_{eg}/\hbar\Delta_{ge}$ is the atomic polarisability tensor in the far-off resonance limit, with $\hat{\mathbf{d}}_{ge}$ being the electric dipole operator between the ground and excited hyperfine states; $\Delta_{ge} = \omega_L - \omega_{ge}$ is the detuning from the transition between the hyperfine levels $|g\rangle \rightarrow |e\rangle$.

The electric dipole operator is a sum of contributions from all the allowed transitions between Zeeman sublevels of the ground and excited states. By expanding the laser field [20], [21], [18] in the spherical polarization basis $(\sigma^+, \sigma^-, \pi)$, it is possible to show that the only non-zero elements of the matrix,

$$\langle F, m_i|\hat{U}(\mathbf{x})|F, m_j\rangle, \tag{2.2}$$

are only those which connect states with $\Delta m = 0, \pm 1, \pm 2$. Terms for which $\Delta m = 0$ lie on the diagonal of the matrix, while off-diagonal terms couple states for which $\Delta m = \pm 1, \pm 2$ and result from stimulated Raman transitions between different ground state sublevels, involving σ and π polarized light. The 'adiabatic' potential is found by diagonalizing this matrix taking into account off-diagonal terms which represent the Raman coupling. The new eigenstates will be a superposition of the

$|F, m\rangle$ basis functions. An adiabatic potential cannot be associated with a pure $|F, m\rangle$ state, but at locations of pure σ^+ or σ^- light, where the Raman coupling is almost non-existent, it is nearly identical to the 'diabatic' potential associated to the $|F, m = \pm 4\rangle$ state. The diabatic potential is obtained simply by neglecting the off-diagonal terms in matrix 2.2. As the atom moves away from regions of pure σ polarization, the contribution to the eigenstate of other magnetic sublevels is increased gradually and avoided crossings are created midway between a σ^+ and a σ^- site. In general, if the Raman coupling is significant, the adiabatic potential describes the lattice better, as long as the atoms move slowly enough through the avoided crossings to undergo Raman transitions. Fast moving atoms will follow the diabatic potential. For atoms tightly bound at σ locations, the adiabatic and diabatic potentials almost coincide.

An optical lattice with polarization gradients will, in general, establish coherences between the different magnetic sublevels of the ground state via stimulated Raman transitions. These coherences, in conjunction with the effects of external magnetic fields, can be exploited to control the atomic state. To study the coherent evolution of the atomic state, it is necessary to start in the dissipation-free regime, i.e. the lattice should be tuned very far from the atomic resonance. In this limit equation 2.1 can be simplified and the optical potential can be written as [18]:

$$\hat{U}(\mathbf{x}) = U_J(\mathbf{x}) + \mathbf{B}_{eff}(\mathbf{x}) \cdot \hat{\boldsymbol{\mu}}, \tag{2.3}$$

where

$$U_J = -\frac{2}{3} U_1 |\boldsymbol{\epsilon}_L(\mathbf{x})|^2 \tag{2.4}$$

and

$$\mathbf{B}_{eff} = \frac{i}{3} U_1 [\boldsymbol{\epsilon}_L{}^*(\mathbf{x}) \times \boldsymbol{\epsilon}_L(\mathbf{x})], \tag{2.5}$$

with U_1 being the single beam light shift and $\boldsymbol{\epsilon}_L$ being the polarization vector. It has been assumed that the lattice is generated by equally intense laser beams, so

that the single beam amplitude can be factorized. From equations 2.3 and 2.5 it can be shown that the light shift potential is equivalent to a shift, proportional to the local intensity of the field and independent of the hyperfine state of the atom ($U_J(\mathbf{x})$) and the effect of an effective fictitious static magnetic field, whose amplitude and direction depend on the local ellipticity of the polarization. This fictitious field is interacting with the magnetic moment $\hat{\boldsymbol{\mu}} = -g_F \mu_B \hat{\mathbf{F}}$, where $\hat{\mathbf{F}}$ is the angular momentum operator, g_F is the gyromagnetic ratio and μ_B is the Bohr magneton.

In the limit of infinite detuning coherences between states with $\Delta m = \pm 2$ go to zero (cf.[18]). If the polarization of the light field is linear at any location, the effective magnetic field vanishes, thus making the light-shift independent of the magnetic sublevel of the atom. For different ellipticity of the laser light, polarization in the plane of the lattice gives rise to longitudinal effective B fields. The combination of a π and σ component of the light gives rise to a transverse effective magnetic field. The great advantage of engineering B_{eff} through the light polarization is that it is possible to generate an effective magnetic field which is spatially varying on the scale of the optical wave-length.

2.2 Effects of static magnetic fields

Equation 2.3 can easily be generalized to take in account of the effect of a static magnetic field $\mathbf{B}$ can be taken in account, as shown in [18], by writing:

$$\hat{U}(\mathbf{x}) = U_J(\mathbf{x}) + (\mathbf{B}_{eff}(\mathbf{x}) + \mathbf{B}) \cdot \hat{\boldsymbol{\mu}}. \tag{2.6}$$

The introduction of a static magnetic field in directions parallel and transverse to the quantization axis (or the fictitious magnetic field itself) gives rise to different effects: a field parallel to the z-axis simply adds a Zeeman energy shift $\Delta E = g_F \mu_B m B_Z$ to the diagonal terms of the optical potential matrix 2.2. This

dependence on the m quantum number can be exploited in order to accumulate atoms in a preferential state in the near-detuned lattice, just by increasing the depth of the corresponding potential through the Zeeman effect.

A transverse magnetic field along the x or y direction creates off-diagonal terms in the optical matrix, which generate the coupling between magnetic sublevels which differ by $\Delta m = \pm 1$. This coupling between magnetic sublevels can be exploited in the near-detuned lattice in order to enhance the cooling efficiency and also to increase the localization of the atoms at the bottom of the potential well.

2.3 Band-structure of the 2-D far-detuned optical lattices

As discussed previously in section 1.2.1.1, the periodicity of the optical lattice allows us to use the methods of solid state physics in order to determine its energy spectrum [22]. For atoms in an optical potential, the Hamiltonian can be written as:

$$\mathbf{H} = \frac{\mathbf{P}^2}{2M} + \hat{U}(\mathbf{x}), \tag{2.7}$$

where $\hat{U}(\mathbf{x})$ is given by equation 2.3 and $\frac{\mathbf{P}^2}{2M}$ is the kinetic energy of the center-of-mass. The eigenvalues of this Hamiltonian form a discrete spectrum of energy levels, as discussed in section 1.2.1.1.

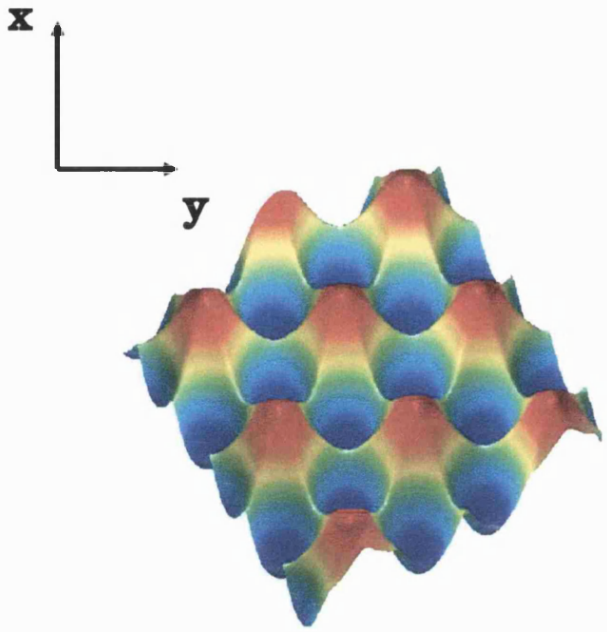

Figure 2.1: Lowest potential surface of a 2-D optical lattice associated with $m_F = \pm 4$ states. Adjacent lattice sites have opposite polarizations.

The band structure and energy levels were calculated for a two dimensional lattice with the geometry of figure 1.8(A). The employed laser beam configuration is shown in figure 6.3. It consists of three co-planar laser beams of equal intensity, propagating at angles of 120° with respect to each other and linearly polarized in the plane of the lattice. This configuration gives rise to a lattice of alternating σ^+ and σ^- sites. The two dimensional diabatic potential for the lower shifted states $m_F = \pm 4$ is shown in a 3D plot in figure 2.1 and as a 2D contour plot in figure 2.2 for just one of the two m_F states. The potential has hexagonal symmetry, with rings of six minima surrounding a potential maximum. Adjacent minima are at locations of opposite pure circular polarization.

A code was available to be used to calculate the vibrational bands of a periodic one-dimensional potential. I used the code to model the two-dimensional potential

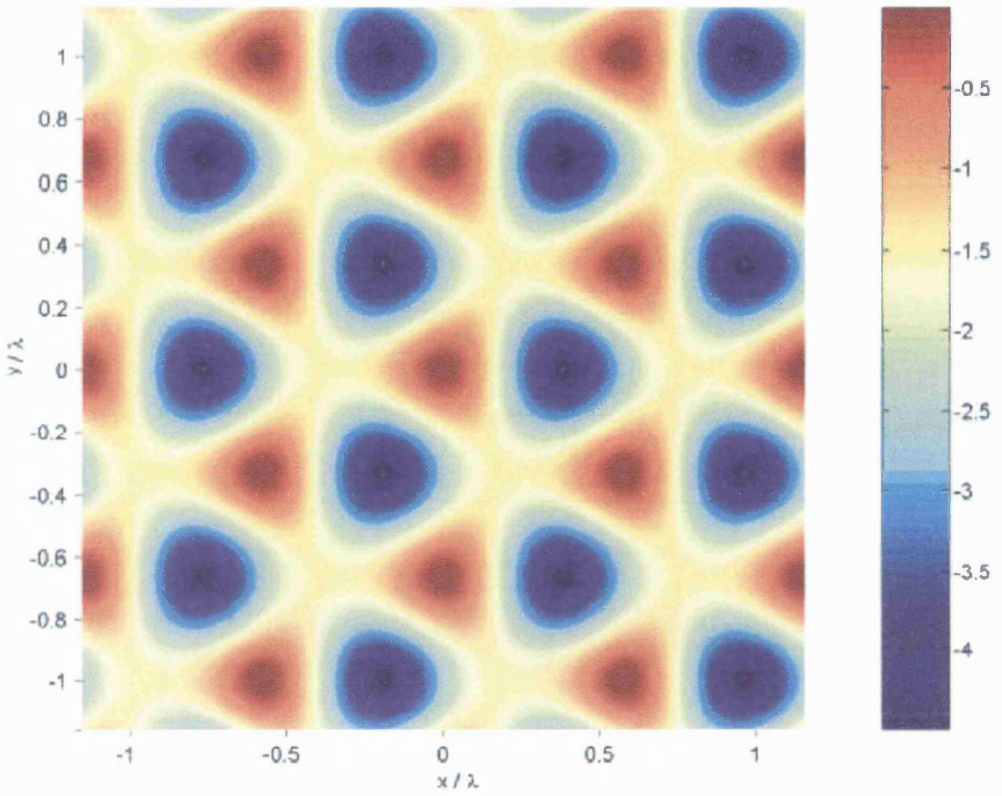

Figure 2.2: 2D contour plot of potential surface of a 2-D optical lattice associated with $m_F = -4$ state.

well by considering cuts along the two directions. As we will see, by using a one-dimensional model, the band structure results are symmetric only for the lower lying vibrational states. In this limit the band structure is independent of the direction chosen and it is therefore justified to assume a unique band structure and introduce the two-dimensional degeneracy for the energy levels. Referring to figure 1.8(A) and 2.2 for the axis definition and selecting one of the potential

wells corresponding to $|m_F = -4\rangle$, cuts along the x and y directions for the 2D potential of figure 2.1 yield the 1D x and y band structure in figure 2.3, 2.4 and 2.5, 2.6 respectively as a function of quasi-momentum q. Superimposed in the same figures is the spatially-varying potential depth, which refers to an arbitrary horizontal scale. In figures 2.3 and 2.4 the x-potential is plotted and the bands

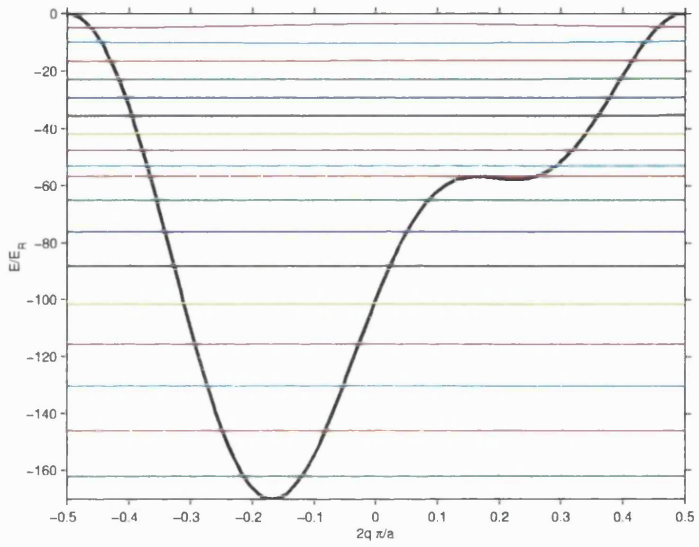

Figure 2.3: Band structure (coloured lines) for a potential depth of 170 E_R, cut in the x-direction, plotted versus the quasi-momentum q. Superimposed on this plot, employing the same vertical scale, is a cut through the potential energy surface in the x direction. The horizontal scale of this curve (black line) is arbitrary and is chosen so that one period of the potential fits into frame of the figure.

are calculated for the $|m_F = 4\rangle$ state for a maximum light shift of $170E_R$ and $250E_R$ respectively; these values represent the typical potential depth used for the experiments. In figures 2.5 and 2.6 the same is shown along the y-direction. It is important to notice that for the lower lying bands the two potentials are equivalent and the vibrational frequencies are the same along the two dimensions. For higher lying bands differences arise: along the x and y direction anharmonicity and asymmetry of the potential make the vibrational frequencies and number of bound states quite different. Since in the experiments the sample is always cooled

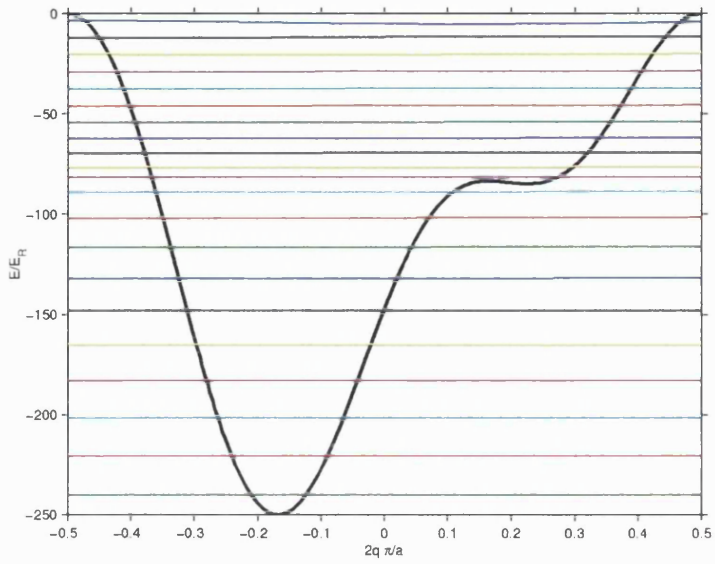

Figure 2.4: Band structure (coloured lines) for a potential depth of 250 E_R, cut in the x-direction, plotted versus the quasi-momentum q. Superimposed on this plot, employing the same vertical scale, is a cut through the potential energy surface in the x direction. The horizontal scale of this curve (black line) is arbitrary and is chosen so that one period of the potential fits into frame of the figure.

to very low temperatures, the population over the higher lying levels is in general negligible. It is then justified to assume that the potential for the lower lying vibrational states in the two dimensions is the same as the symmetric potential along the y-direction.

The different levels also present a certain band-width of allowed energy. The width of the bands, see section 1.2.1, is not shown in figures 2.5 and 2.6, but the results of band width calculations are shown in table 2.1, where the σ_n represents the width of the nth band. It is noteworthy that the spacing between the bands decreases with increasing band index n and at the same time the width of the bands increases with n, due to anharmonicity of the potential. In the tight binding regime, near the bottom of the potential well, the bands are well approximated by the vibrational energy levels of a harmonic oscillator; the band index n can

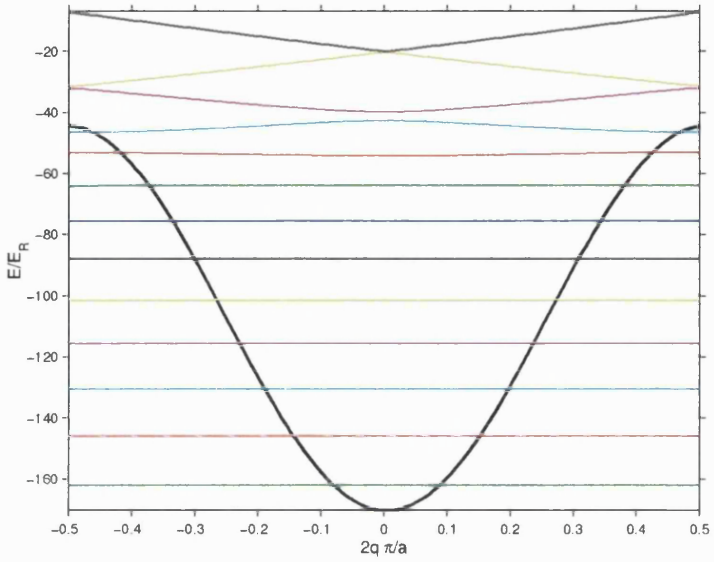

Figure 2.5: Band structure (coloured lines) for a potential depth of 170 E_R, cut in the y-direction, plotted versus the quasi-momentum q. Superimposed on this plot, employing the same vertical scale, is a cut through the potential energy surface in the y direction. The horizontal scale of this curve (black line) is arbitrary and is chosen so that one period of the potential fits into frame of the figure.

then be considered as the vibrational quantum number. The width of the bands in this regime is negligible, showing that no significant tunneling between wells occurs. Going to higher vibrational numbers, the bands get closer and they show a significant curvature and width. The curvature arises because, when an atom's energy is greater than that of the lowest adiabatic potential well, it can tunnel between adjacent potential wells, leading to a spread of the wavepacket. This can result in atoms being less localized and therefore diffusing through the lattice. In the x-direction the potential presents different periodicity and symmetry, but for low-lying bands, in the tight binding regime, the two cuts present similar characteristics of energy levels, curvature and width.

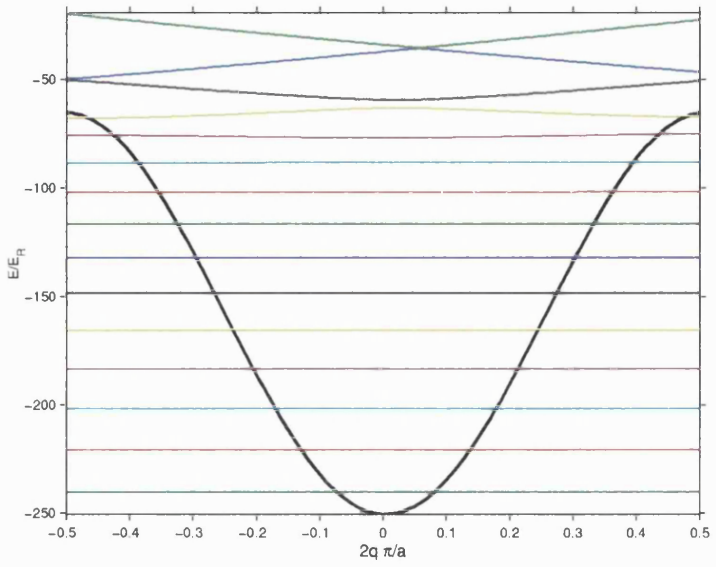

Figure 2.6: Band structure (coloured lines) for a potential depth of 250 E_R, cut in the y-direction, plotted versus the quasi-momentum q. Superimposed on this plot, employing the same vertical scale, is a cut through the potential energy surface in the y direction. The horizontal scale of this curve (black line) is arbitrary and is chosen so that one period of the potential fits into frame of the figure.

2.4 Theory of resolved-sideband Raman cooling

In this section I will describe the principle of the resolved-sideband Raman-cooling scheme used in our work, which was proposed for the first time by Jessen and Deutsch in [18] and experimentally demonstrated in 1998 [20].

In the previous section it was pointed out that, for atoms localized at the bottom of the potential well, in the tight binding regime, without any further perturbation, tunneling between neighbouring wells is negligible. This condition allows us to consider each lattice site as an independent potential well. At locations of maximum light shift the optical potential has pure helicity: the most deeply bound states have negligible mixture of Zeeman sub-states. But if the vibrational levels n of two $|m_F\rangle$ states become degenerate, then coupling between different m_F wells can be introduced as a transverse component of the fictitious magnetic

$U_{max} = 170E_R$			$U_{max} = 250E_R$		
n	σ_n(kHz)	$E_{n+1} - E_n$ (kHz)	n	σ_n(kHz)	$E_{n+1} - E_n$ (kHz)
0	0.0000	32.943	0	0.0000	40.204
1	0.0000	31.724	1	0.0000	39.005
2	0.0000	30.423	2	0.0002	37.743
3	0.0000	29.018	3	0.0012	36.409
4	0.0004	27.478	4	0.0070	34.988
5	0.0040	25.747	5	0.0028	33.464
6	0.0488	23.712	6	0.0907	31.813
7	0.3897	21.116	7	0.2300	29.981
8	2.3099	17.915	8	0.4848	27.832
9	7.9608	17.499	9	0.7831	24.979
10	16.2395	21.134	10	3.7082	21.696
11	22.6617	25.132	11	9.8553	20.313
12	26.6338	28.672	12	18.7859	27.588
13	30.1953	30.876	13	28.5801	28.368

Table 2.1: Energy separation between vibrational levels and levels widths (σ_n) for $U_{max} = 170E_R$ and $U_{max} = 250E_R$. For increasing n number anharmonicity becomes significant and the bands are broadened.

field and resonantly enhanced, thus leading to a mixture of states.

Sideband Raman-cooling is based on the exploitation of this coherent mixing of states, by controlling the coupling between different product states $|m_F\rangle \bigotimes |n\rangle$, or $|m_F, n\rangle$ states, in order to selectively transfer population from a state $|m_F = 4, n+1\rangle$ to a state $|m_F = 3, n\rangle$. Optical pumping then transfers the atoms back to the $m_F = 4$ state. When atoms are in the Lamb Dicke regime, $\frac{E_R}{\hbar\omega_{vib}} \ll 1$, which means that the energy separation of vibrational levels is much greater than the recoil energy; this implies that elastic scattering is favoured. In a typical

experiment the Lamb Dicke factor $\frac{E_R}{\hbar\omega_{vib}}$ is 1/20 so that to a good approximation optical pumping brings back the atoms to the $m_F = 4$ state without a further change in vibrational quantum number, thus decreasing the vibrational energy by one quantum.

The electromagnetic field can induce coherences between states $|m\rangle \rightarrow |m + \Delta m\rangle$, where $\Delta m = \pm 1, \pm 2$, through stimulated Raman transitions involving photons of polarization $\pi \leftrightarrow \sigma^{\pm}$ or $\sigma^{\pm} \leftrightarrow \sigma^{\pm}$ respectively. In the infinite detuning limit it is possible to show [18] that the $\Delta m = \pm 2$ coherence term goes to zero. Furthermore it has been proved [18] that, even at smaller detunings, the efficiency is very small, thus making the $\Delta m = \pm 2$ induced coherences not useful for coherent control. Coherences between states with $\Delta m = \pm 1$ can be induced by means of a magnetic field and stimulated Raman transitions, the interaction matrix being:

$$U_{m,m\pm 1} = \frac{\langle\{n'\}, m \pm 1|[B_x^{tot}(x) \mp iB_y^{tot}(x)]\hat{F}_{\pm}|\{n\}, m\rangle}{2F}, \tag{2.8}$$

where B_{tot} is the sum of the external and fictitious magnetic fields. An external transverse magnetic field does not couple states of different parity $|m, n\rangle, |m \pm 1, n \pm 1\rangle$, which are located at the same lattice site. It is however possible to exploit the effective magnetic field in order to generate both even and odd parity couplings. In the limit of infinite detuning equation 2.8 becomes, as shown in [18],

$$U_{m,m\pm 1} = -\frac{U_0}{3\sqrt{2}}\frac{\sqrt{F(F+1) - m(m \pm 1)}}{F}\langle\{n'\}|[\epsilon_{\pi}^*(x)\epsilon_{\sigma_{\pm}}(x) + \epsilon_{\sigma_{\pm}}^*(x)\epsilon_{\pi}(x)]|\{n\}\rangle, \tag{2.9}$$

where $\epsilon_{\sigma_{\pm}}$ and ϵ_{π} are the different components of polarization of the electric field and n are the vibrational quantum numbers. From equations 2.5 and 2.9 it follows that the Raman coupling terms are zero at locations of pure polarization ($\sigma_{\pm}$ or π).

In the 2-D configuration which we are using, figure 2.7, the coupling potential is introduced by slightly rotating the polarization of one of the beams out of the

lattice plane. This introduces the π component needed for Raman coupling at sites where the polarization would otherwise be entirely $\sigma_{\pm}$. Changing the polar-

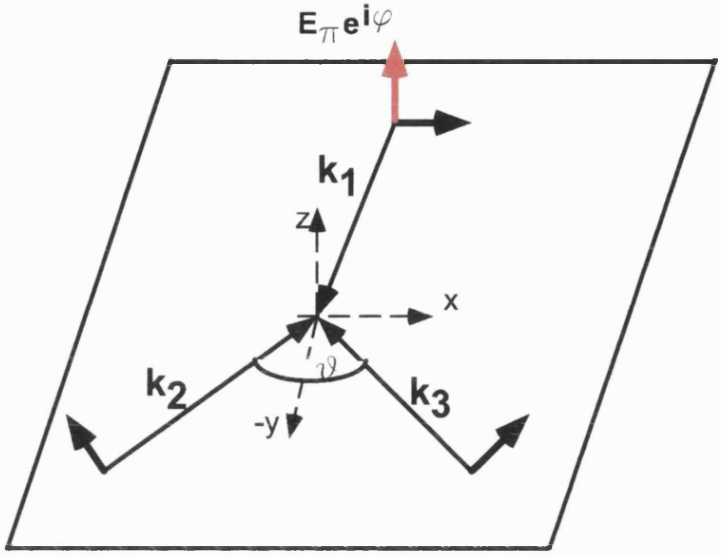

Figure 2.7: Experimental setup for resolved-sideband Raman cooling: Raman coupling is introduced by adding a πpolarized component (red) to the light field.

ization of one of the beams from linear to elliptical, corresponds to introducing a π polarized light with amplitude E'_π (figure 2.7) and relative phase $e^{(i\phi)}$ with respect to the beam propagating in the $-y$ direction. It can be shown [18] that the total electric field is then given by:

$$E_L(\mathbf{x}) = \frac{E'_1 e^{-iky}}{\sqrt{2}}\{-\mathbf{e}_+[1 + 2e^{iK_y y}\cos(K_x x)] + \\ +\mathbf{e}_-[1 + 2e^{iK_y y}\cos(K_x x - 2\theta)]\} + \mathbf{e}_\pi E'_\pi e^{-iky}e^{i\phi}, \tag{2.10}$$

where $K_x = k\sin\theta$ and $K_y = k(1 + \cos\theta)$. The effective magnetic field then becomes:

$$B_x^{eff} + iB_y^{eff} = -\frac{2U_1}{3}\frac{E'_\pi}{E'_1}[2\sin\theta\sin(K_x x - \theta)\cos(K_y y - \phi) \\ +2i\cos\theta\cos(K_x x - \theta)\sin(K_y y - \phi) - i\sin\phi], \tag{2.11}$$

where U_1 is the single-beam light-shift for a Clebsch-Gordan coefficient of 1. Equa-

tion 2.11 shows that the Raman coupling has both even and odd terms along both coordinates of the lattice plane and its effectiveness (i.e. amplitude and phase) can be adjusted through the ellipticity of the beam.

Using equation 2.8 and 2.11 and expanding around the minimum of the potential well in the harmonic approximation, it can be shown that maximum coupling for the odd parity states occurs for $\phi = \pi/2$. The efficiency of coherent transfer can be characterized by one parameter, or figure of merit [18], which depends on the ratio of π component to σ component, detuning and potential depth. For our lattice configuration, the figure of merit for coherent transfer of population is given by :

$$k = \frac{U_R}{\hbar\gamma_s} \approx \frac{0.0047}{\sqrt{F}} \frac{E_\pi}{E_1} \frac{|\Delta|}{\Gamma} \left(\frac{E_R}{U_1}\right)^{1/4}, \tag{2.12}$$

where $U_R = \frac{U_1}{2\sqrt{2F}} \frac{E_\pi}{E_1} \eta$, η is the Lamb-Dicke parameter and E_R is the recoil energy. The coupling introduced with π light induces transitions from $|m, n\rangle$ to $|m-1, n-1\rangle$. Relaxation back to the vibrational manifold of the $|m\rangle$ state with the loss of one quantum of vibrational energy is induced by optical pumping, as shown in figure 2.8, where the pumping beam tuned to the $|F = 4, m_F = 3\rangle \rightarrow |F = 4, m_F = 4\rangle$ transition is represented in blue. Also in the same figure a repumper beam (red) tuned to the $F = 3 \rightarrow F = 4$ transition is shown: this is used to replenish the hyperfine ground state on which the cooling happens. Raman coherences induced by π, σ light are represented in black.

For cooling to be efficient it is necessary that the heating rate, which is dominated by photon scattering, is well below the oscillation frequency, which means:

$$\left(\frac{\hbar\omega_{osc}}{E_R}\right)^2 \gg \frac{\hbar\gamma_s}{E_R}. \tag{2.13}$$

This also means that the time-scale for population transfer, $\hbar/U_R$, must be much shorter than the vibrational excitation rate:

$$\frac{|U_R|}{\hbar\overline{dn}/dt} = k \gg 1, \tag{2.14}$$

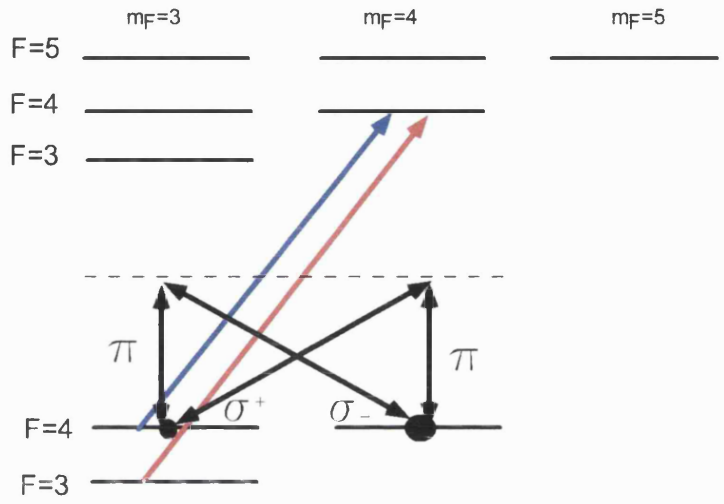

Figure 2.8: Experimental level scheme for resolved-sideband Raman cooling. The Raman pumper σ^+ polarized, tuned to $F = 4 \rightarrow F = 4$ transition is shown in blue, the repumper light σ^+ polarized, tuned to $F = 3 \rightarrow F = 4$ transition is shown in red and Raman coupling is represented with black arrows.

where k is the merit factor for the population transfer with optical pumping. The figure of merit is derived in [18] and is:

$$k_x \approx 0.17 \frac{E_\pi}{E_1} \frac{|\Delta|}{\Gamma} \left(\frac{U_1}{E_R} \right)^{1/4}; \qquad k_y = 3k_x. \tag{2.15}$$

In all the experiments performed, see chapter 7, the figure of merit was estimated to be $\gg 1$.

The Raman coupling introduced by changing the polarization of one of the lattice beams can be resonantly enhanced by bringing into degeneracy levels $|m_F = 4, n\rangle$ with $|m_F = 3, n-1\rangle$. In figure 2.9 the potential and band structure is shown for the $m_F = 4$ and $m_F = 3$ states, for $U_{max} = 200E_R$. A magnetic field along the quantization axis would Zeeman-shift the levels proportionally to their m_F quantum number. By adding a static magnetic field, states $|m_F = 4, n\rangle$ and $|m_F = 4, n-1\rangle$ can be brought in resonance, which is referred to as tuning to the first red sideband. In figure 2.10 the magnetic field necessary to tune to the first sideband is plotted versus the potential depth for the different pairs of levels

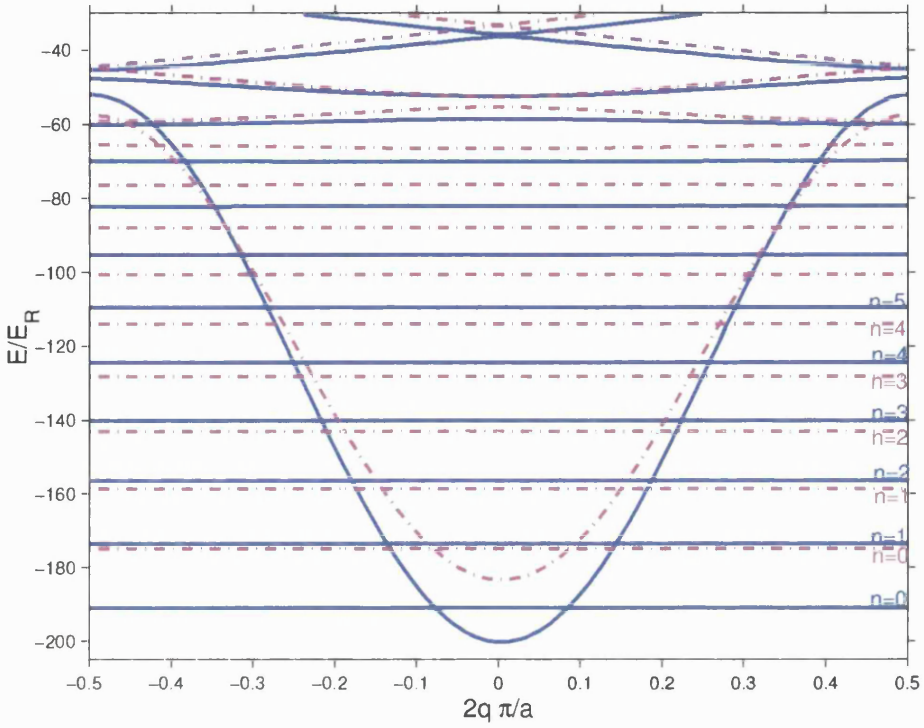

Figure 2.9: Band structure for the $m_F = 4$ (blue) potential and $m_F = 3$ (purple) potential.

involved $\{n, n-1\}$, with $n = 1 \rightarrow 5$. The various lines represent the values of magnetic field necessary so that $m_F = 4, n = 1, 2, 3, 4, 5$ levels can be brought into degeneracy with the corresponding $m_F = 3, n-1$ states, for different potential depths. Even for a fixed potential depth, from figure 2.10 it can be seen that different vibrational levels $\{n\}$ are brought into degeneracy with $\{n-1\}$ levels for different values of the magnetic field. This is due to anharmonicity and the fact that higher lying levels are more closely spaced than lower ones. The range of values of magnetic field necessary to go through all the resonances depends on the potential depth. It should also be noted that a similar plot to figure 2.10 but calculated for the potential cut along the y-direction would show almost identical values as those found for the x-direction. Differences however arise for higher lying vibrational states: the spread in values becomes quite large, especially in the x-

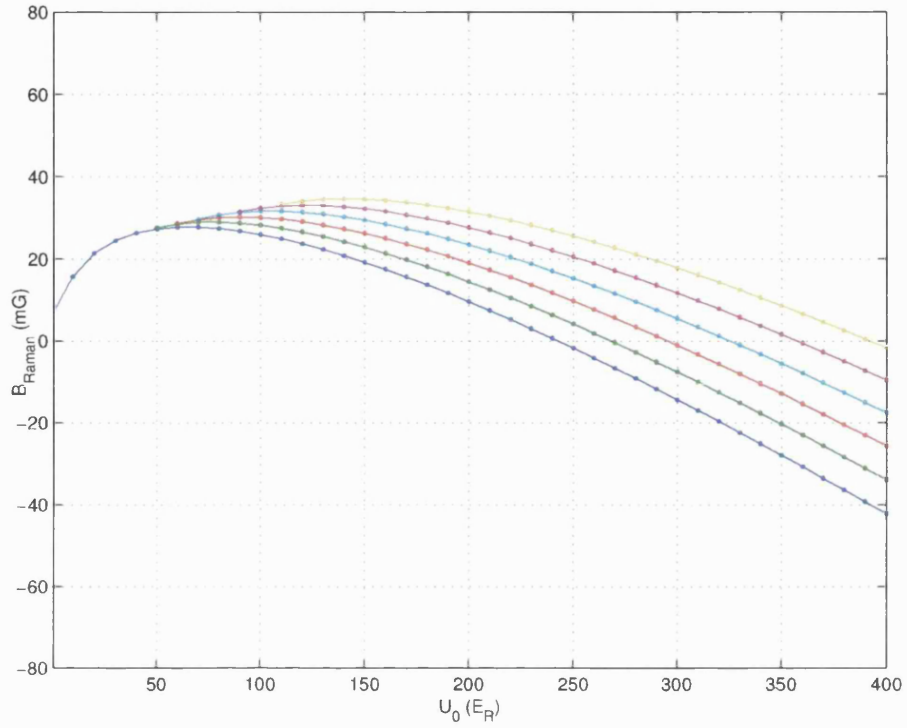

Figure 2.10: Magnetic field to tune to the first red sideband for different potential depths.

direction and their range becomes substantially different too. This indicates that in order to obtain efficient cooling in two dimensions, it is necessary to start with only the lower lying levels in the x and y directions appreciably populated, so that they are characterized by similar parameters and can be cooled simultaneously.

In conclusion, in this section I have explored the feasibility of a method to increase the population of the ground vibrational level of the potential well associated with one stretched state. This method is based on the addition of a π component of light to the lattice field, and necessitates the use of a pumper beam to repopulate the stretched state, as well as a static external magnetic field to Zeeman-shift and thus bring into degeneracy vibrational levels of potential wells corresponding to different magnetic substates.

2.5 Population distribution over vibrational levels

In this section I discuss the behaviour of atoms in a harmonic potential well and some quantities will be defined which are to be used in later chapters. The eigen-

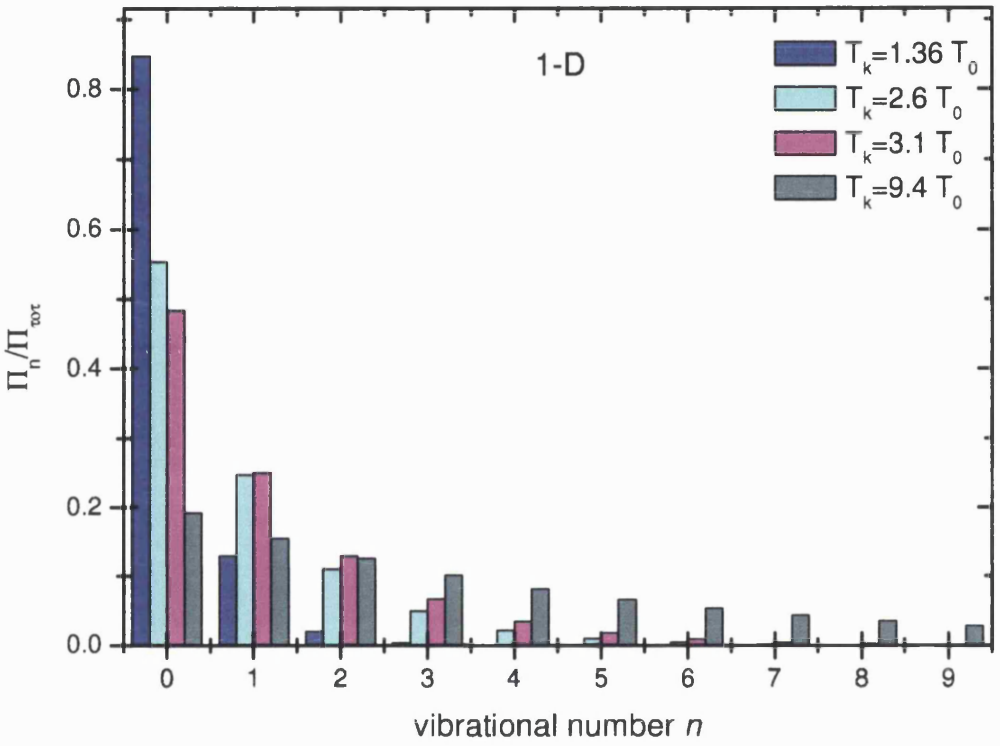

Figure 2.11: Block diagram for population of different vibrational levels at different temperatures for 1-D harmonic oscillator for ground state kinetic temperature T_0.

states of atoms trapped in an harmonic potential can be characterized as product states $|F, m\rangle|n\rangle$, where n is the harmonic oscillator quantum number. For an ensemble of atoms in thermal equilibrium, the population is distributed over different vibrational levels and this distribution defines the vibrational temperature T_v of the sample. For a two-dimensional harmonic oscillator the occupation probability for a vibrational level characterized by $n_x = 0, n_y = n$ is [23]:

$$\Pi_n = (1 - q_B)^2 q_B^n, \tag{2.16}$$

where

$$q_B = e^{-\frac{\hbar\omega_{osc}}{k_B T_{vib}}} = \frac{\Pi_n}{\Pi_{n-1}} \tag{2.17}$$

is the Boltzman factor. The mean vibrational excitation number is given by:

$$\overline{n} = \sum_n \Pi_n n = \frac{q_B}{1 - q_B}. \tag{2.18}$$

The kinetic temperature is defined in terms of the variance Δp, along one dimension, of the momentum distribution of the ensemble of atoms, as:

$$T_K = \frac{(\Delta p)^2}{M k_B}. \tag{2.19}$$

The momentum variance is related to the ground state momentum $p_0 = M\hbar\omega_{osc}/2$:

$$(\Delta p)^2 = p_0^2(2\overline{n} + 1). \tag{2.20}$$

Introducing the ground state kinetic temperature $T_0 = p_0^2/mk_B$ and combining equations 2.19 and 2.20 we get:

$$\frac{(\Delta p)^2}{p_0^2} = \frac{T_K}{T_0} = (2\overline{n} + 1). \tag{2.21}$$

It is also possible to rewrite q_B only in terms of T_K and T_0, as it comes from equations 2.17, 2.18, 2.21:

$$q_B = \frac{T_K - T_0}{T_K + T_0}. \tag{2.22}$$

Using equations 2.21 and 2.16 the population of the ground state (as well as the populations of all bound levels) are reconstructed by simply measuring the kinetic temperature of the sample after its release from the far-detuned lattice (FDL). In figure 2.11 the population distribution for a 1-dimensional harmonic oscillator is calculated, assuming a ground state temperature $T_0 = 0.956\mu$K for four different kinetic temperatures. As we are interested in the ground state population of a two-dimensional harmonic oscillator, in figure 2.12 a diagram of the population distribution over different vibrational levels for the same temperatures is shown, for a 2-D harmonic oscillator in the case $n_x = 0, n_y = n$. It has been assumed that the temperatures in both dimensions are the same.

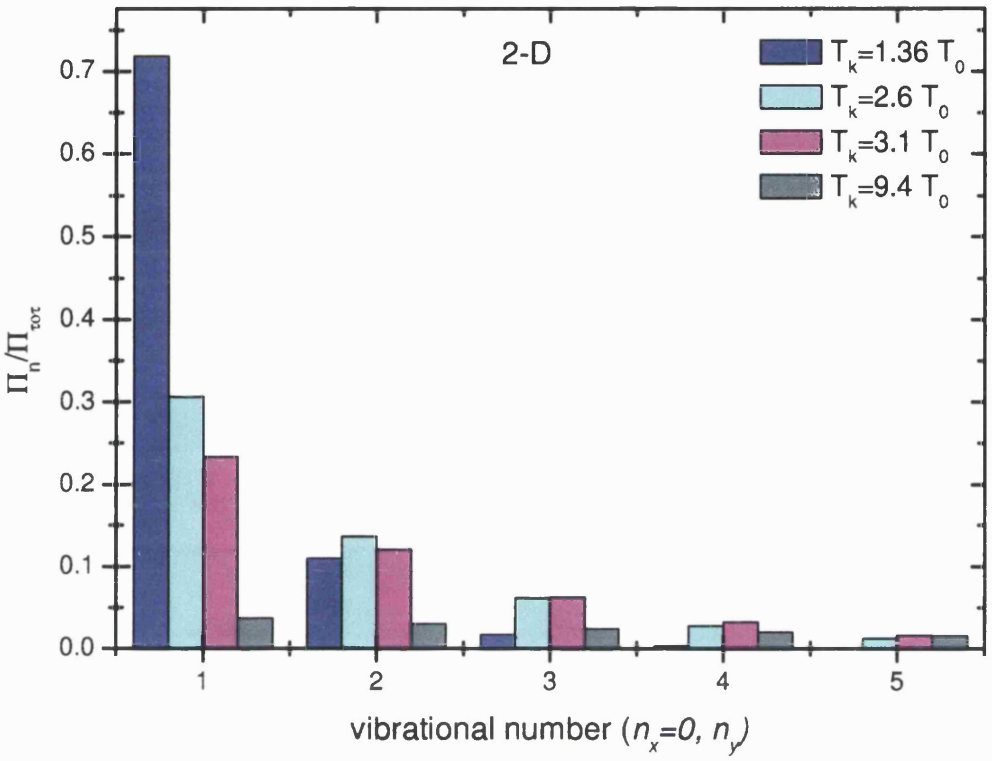

Figure 2.12: Block diagram for population of different vibrational levels at different temperatures for a 2-D harmonic oscillator with $n_x = 0, n_y = n$ and ground state kinetic temperature T_0.

2.6 Conclusions

In this chapter I have presented the theory for far-detuned optical lattices and the results of band calculations in this regime. A method for resolved-sideband Raman cooling was explored and the parameters required to tune the cooling to the first sidebands were calculated. Finally, the population distribution over the different vibrational levels was calculated for 1-D and 2-D harmonic oscillators.

CHAPTER 3

The Experimental Apparatus

This chapter reviews the experimental apparatus, which was set up during the first year of my PhD. The experiment was previously partially set up in Oxford but it was moved to London in coincidence with the start of this work. I have worked on rebuilding the experiment in London, particularly in implementing the set-up for the far-detuned optical lattice and all the experiments described in this thesis. I also computer-automated the experiment, through multiple input/output boards and the Labview programming language. The chapter begins with a description of the laser sources, placing particular emphasis on the techniques used to narrow the natural emission line shape and the fine control of the frequency tuning. These parameters are particularly crucial in a laser cooling experiment. The setup to control stray magnetic fields, as well as the magnetic quadrupole trap coils are then described. Most of the measurements presented in this thesis exploit a time-of-flight setup which is presented at the end of the chapter. All the parameters and characteristic times of the experiment were computer-controlled and the basics of the software and hardware tools used can be found in the last section of this chapter.

3.1 The caesium source

The gas of caesium atoms is contained in a cell of 132 × 72 × 52 mm, with 5 mm thick walls, antireflection coated on the outside for 852 nm wavelength light. The cell is kept at very low pressure, down to 10^{-9} Torr, using a ion pump. For a detailed description of the vacuum system I refer to [24].

The nuclear spin of the caesium atom is $I = 7/2$, and the hyperfine interaction splits the levels in the eigenstates of the total angular momentum F, according to the scheme in figure 3.1. The caesium transition used to cool and trap the atoms is the D_2 $6^2S_{1/2}, F = 4 \rightarrow 6^2P_{3/2}, F = 5$ at a wavelength of 852 nm. The lifetime of the excited level is 30 ns, corresponding to a natural linewidth $\Gamma/2\pi = 5.22$ MHz.

3.2 Laser frequency stabilization

A typical laser-cooling experiment requires several different laser sources tuned at different frequencies. In this section a brief description of the required tuning for the lasers is given, while referring to later sections for the techniques used.

The atoms are first collected and cooled in a magneto-optical trap (MOT), which consists of three pairs of counter-propagating laser beams, with opposite circular polarization, tuned to the low frequency side of the D_2 line, $F = 4 \rightarrow F' = 5$ transition. At the same time a repumper beam tuned to the D_2 line, $F = 3 \rightarrow F = 4$ transition is used to pump atoms lost to $F_g = 3$ back to the cooling transition. A further step in cooling is obtained by further detuning the trapping beam and switching off the magnetic field gradient, so that the atoms are left to cool further in an optical molasses. The atoms are then transferred to a 2-dimensional near-detuned optical lattice, composed of three co-planar light beams arranged at 120° with respect to each other, and linearly polarized in the plane

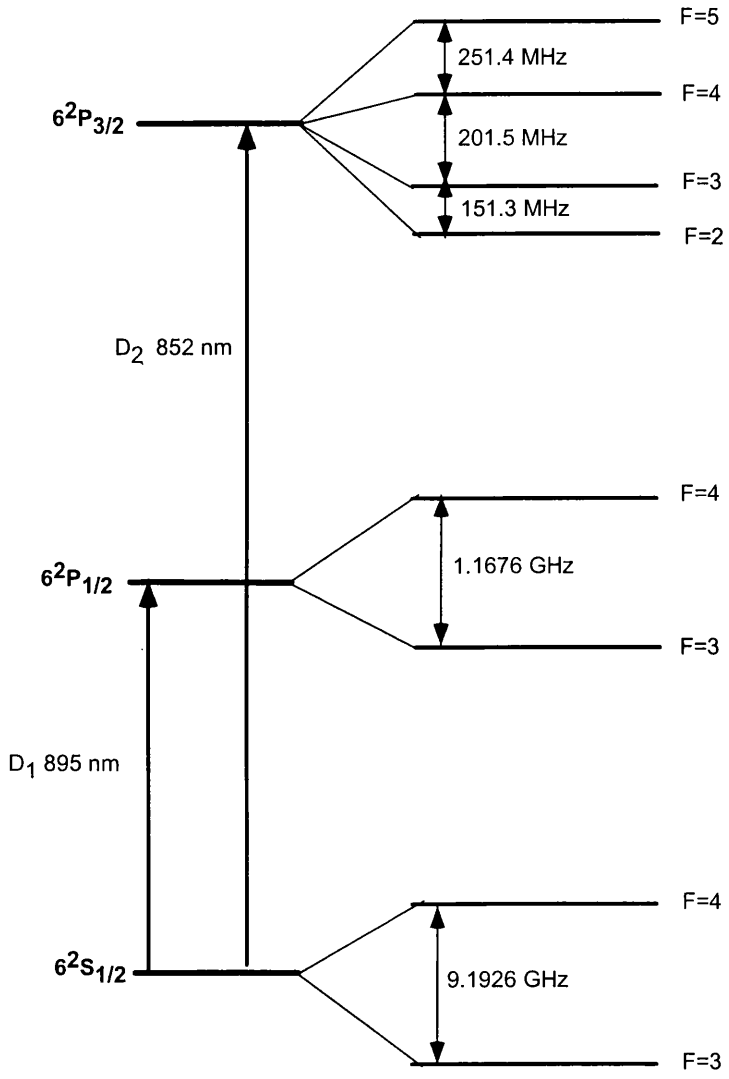

Figure 3.1: Scheme of the hyperfine structure for caesium atom.

of the lattice. This change of geometry makes it necessary to use a different laser source, tuned to the red of the $D_2, F = 4 \rightarrow F' = 5$ transition, which also allows a greater range of detunings. The next step is to generate a far-detuned lattice,

detuned up to 20 GHz to the red of the $D_2, F = 4 \rightarrow F' = 5$ transition, which means being well detuned to the low frequency side (*red*) of all the excited state hyperfine structure. Furthermore, the intensity needs to be increased by orders of magnitude, thus making necessary the use of another laser source. In what follows, I will explain how the different beam's frequencies are set and controlled, while in the subsequent sections I will explain the method which was used in order to create very narrow emission linewidths.

As will be discussed later, a diode laser is used as the master laser, providing a frequency reference to the trap and near-detuned lattice lasers, which are both injection-locked to the master. A part of the master laser output beam is routed to a saturated absorption setup (see next section), after being shifted in frequency through an acousto-optic modulator (AOM) used in a double pass. The saturated absorption signal is used to lock the master laser, as explained in section 3.4, on the crossover of the $F = 4 \rightarrow F' = 4, 5$ transitions. The master frequency can therefore be set to twice the frequency shift produced by the acousto-optic modulator (AOM) from the $F = 4 \rightarrow F' = 4, 5$ cross-over, see figure 3.2. The master output beam is then employed to inject the trap laser. Before being sent to the cell, the trap beam is further shifted toward the red of the $F = 4 \rightarrow F' = 5$ transition, as shown in figure 3.2.

The master laser also generates the beam that is used to inject the near-detuned lattice laser, but it is first double-shifted via an AOM used in a double pass. The output of the injected lattice laser, is then further shifted by a fixed 80 MHz acousto-optic modulator. A repumper beam is added, tuned to the D_2 $F = 3 \rightarrow F' = 4$ transition, locked on a saturated absorption signal. This laser only provides repumping light, needed to replenish the ground state $F_g = 4$ level on which the cooling processes happen. The far detuned optical lattice reference

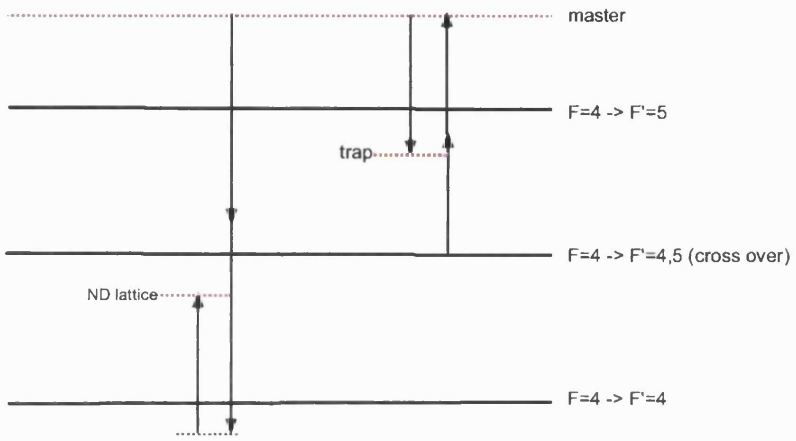

Figure 3.2: Scheme of frequencies for the near-detuned lattice and trap beam, as obtained by shifting the master-injecting frequency.

frequency is generated by a DBR laser diode, with very narrow emission linewidth. The DBR output is used to pump a single-pass tapered-amplifier (MOPA - Master Oscillator Power Amplifier) [25], [26], [27], capable of an output of up to 0.5W. A detailed description of this system can be found in section 3.6.

3.3 Grating-stabilized diode lasers

Diode lasers are very sensitive to optical feedback. The free-running laser has many different oscillation modes and the emission frequency ω is determined by the competition of the different modes. By increasing the number of photons at a specific frequency ω_f it is possible to support the gain of the mode at frequency ω_f while inhibiting the others, thus forcing the emission at ω_f and reducing the linewidth. In order to narrow the bandwidth of the laser and to select a particular frequency, optical feedback is used. The optical feedback is obtained by means of a diffraction grating, which allows us to select a specific wavelength to be retro-reflected into the laser cavity. The grating is placed in the path of the output laser beam in a Littrow configuration, forming an extended cavity resonator with the

back facet of the diode laser [28], [29], as shown in figures 3.3, 3.4. In the Littrow

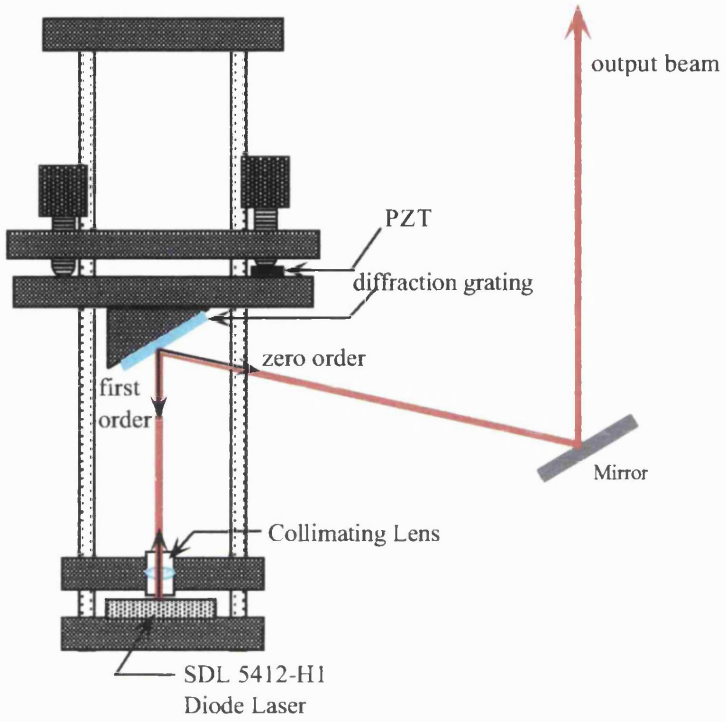

Figure 3.3: Scheme of the external cavity configuration.

configuration, represented in figure 3.4 when $\alpha = \beta$, the first diffracted order is reflected in the direction of the incident beam back into the laser cavity (which is now formed by the back facet of the diode and the grating), thus forcing the laser oscillation at the frequency of the reflected beam. By changing the grating's orientation with respect to that of the incident beam, it is possible to select a specific wavelength according to the dispersive law

$$2d\sin(\alpha) = m\lambda, \tag{3.1}$$

where d is the pitch of the grating, α is the incidence angle and m the diffractive order, see figure 3.4. The grating used here had 1200 lines/mm and $\lambda_{blaze} = 750$ nm. The grating is placed on a mount which allows rotations about two axes

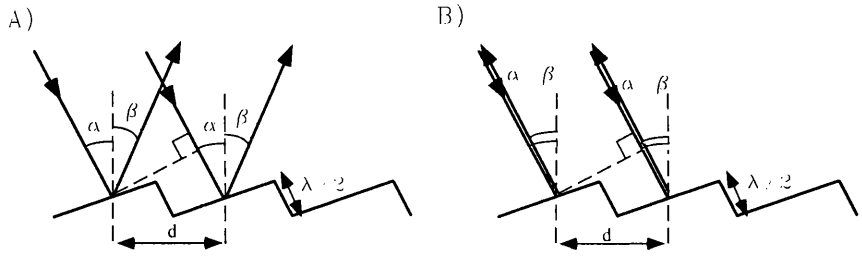

Figure 3.4: Scheme of the grating in the Littrow configuration.

in order to obtain alignment of the first order diffracted beam and also to select different wavelengths. The optimum alignment is obtained by minimising the threshold current.

With diode lasers in external cavity configuration it is therefore possible to control the emission wavelength. At the same time, a narrowing of the linewidth is also produced, due to the increased finesse of the cavity on which the radiation oscillates. In this way the linewidth of the laser may be reduced from some tens of MHz to a few tens of kHz only. The emission frequency can be tuned within the free spectral range of the resonator, by adjusting the cavity length. A variation ΔL in the length of the cavity gives a change in frequency given by:

$$\frac{\Delta\nu}{\nu} \simeq \frac{-\Delta \mathrm{L}}{L}. \tag{3.2}$$

The extended cavity configuration also has disadvantages, due to the increased mechanical and thermal instability, that can lead to an uncontrolled drift of the emission frequency. The cavity is therefore isolated from mechanical vibrations and air currents and the diode is thermally stabilized, by means of a Peltier element and feedback circuit.

3.4 Laser frequency stabilization on an atomic resonance

In order to lock the laser at a specific frequency, any drift must be controlled and corrected electronically. A correction signal must be generated and added to the driving current of the laser, or to the voltage that controls the piezo-electric element in the laser cavity. The error signal used to control the laser frequency is the derivative of the saturated absorption signal of caesium. A saturated absorption scheme is necessary because the spectrum generated by the absorption of a gas of atoms on a laser beam is broadened mainly because of the Doppler effect: atoms with different velocities are brought in resonance by the laser light for different values of the radiation frequency. This broadening would hide the hyperfine structure, being larger than the separation between the levels. With sub-Doppler spectroscopic techniques it is possible to remove this cause of broadening and resolve the hidden hyperfine structure. The scheme used in our experiment is that of saturated absorption (figure 3.5). Two counter-propagating monochromatic laser beams with frequency ω are sent into the gas sample. Because of the Doppler effect, atoms of different velocities will see a different frequency $\omega_D = \omega(1 \pm v/c)$, where v is the component of the atomic velocity in the direction of the beam propagation. Atoms can absorb a photon of frequency ω if their velocity $\mathbf{v}$ is such that

$$|\omega - \omega_0 - \mathbf{k} \cdot \mathbf{v}| \leq \frac{\Gamma}{2\pi}, \tag{3.3}$$

where Γ is the width of the excited level.

In general, the two counter-propagating beams will bring into resonance two different classes of atoms with equal and opposite velocities, unless they are tuned exactly to the resonance frequency, in which case they both interact with the same class of atoms of zero velocity. Therefore, one beam interacting with a group of atoms in a small range of velocities ($|\mathbf{k} \cdot \mathbf{v}| < \frac{\Gamma}{2\pi}$) will modify the population dis-

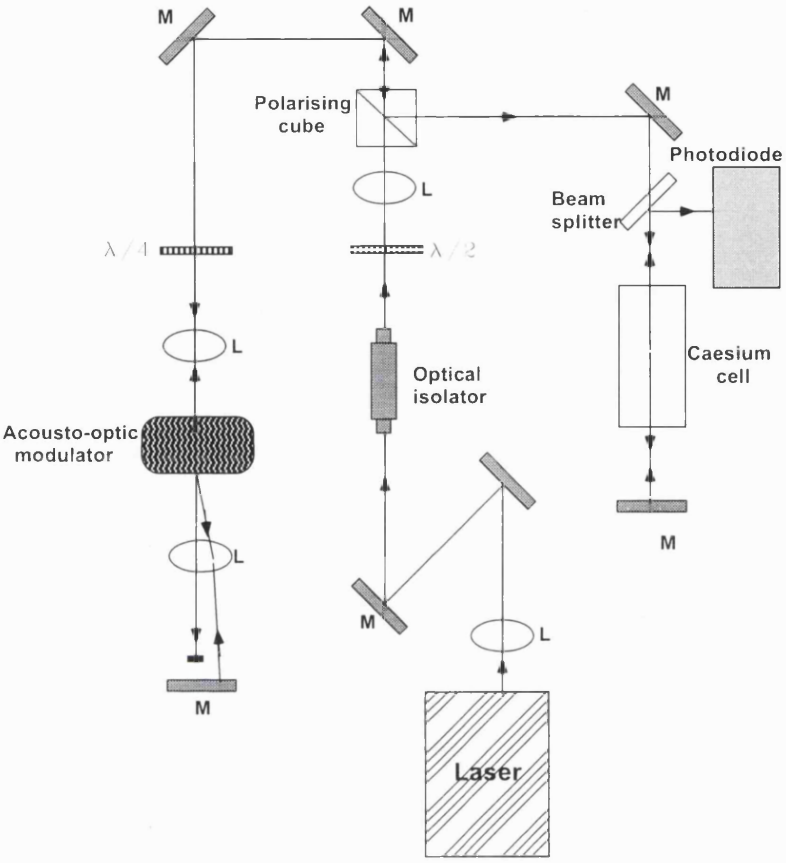

Figure 3.5: Representation of the saturation absorption scheme use to stabilize lasers frequency.

tribution of the ground state creating a *hole* in the distribution of velocities for which the atoms are brought in resonance. At the same time a peak is generated in the population distribution of the excited level corresponding to the same class of velocities (*hole burning*). The second beam therefore interacts with a modified population distribution. If the first beam has an intensity comparable to the caesium saturation intensity (1.12 mW/cm^2) and the transmission of the other beam is observed, the absorption profile shows a dip corresponding to the frequencies that bring in resonance atoms with velocities for which the *hole burning* happens.

Figure 3.5 shows the scheme that was used to obtain the spectrum shown in

figure 3.6 for the master laser. The output of the master laser is sent through a Faraday optical isolator, in order to avoid any unwanted feedback to the laser cavity. The beam is then sent to an acousto-optic modulator (AOM) set in a double pass configuration, in such a way that the first order diffracted beam is retro-reflected in the AOM, being overlapped with the in-going beam. The effect of this is a double shift in frequency as explained in section 3.2. A quarter wave-plate and a polarising cube are used to route the frequency double-shifted beam to the saturated absorption scheme (fig. 3.5). In figure 3.6 one can distinguish the absorption lines corresponding to allowed transitions between the hyperfine sub-levels of the excited state and the ground state. Also visible, are cross-over lines arising from atoms which have non-zero velocity and that are Doppler-shifted into resonance with two different transitions, giving rise to saturated absorption lines at the mean frequency of the two transitions. In figure 3.8 the caesium saturated absorption spectrum used for the repumper laser shows transitions from the $F = 3$ ground state to the excited hyperfine level $F = 4$. This signal was obtained with a similar scheme to the one described for the master laser. In order to use the saturated absorption scheme to frequency-lock the laser on an atomic line, it is necessary to transform the correction signal into an anti-symmetric signal which discriminates between the drift of the laser towards high or low frequencies. By frequency-modulating the laser light itself, it is possible to extract the first derivative of the saturated absorption signal and to use this to correct for the frequency drift of the laser.

If a signal $f(x)$ is frequency-modulated with a modulation amplitude m and modulation frequency ω, it is possible to show that the signal can be decomposed in the sum of terms which oscillate at different harmonics, multiples of the modulation frequency:

$$f(x + m\cos(\omega t)) = \Sigma_{n=0}^{\infty} A_n(x, m)\cos(n\omega t). \tag{3.4}$$

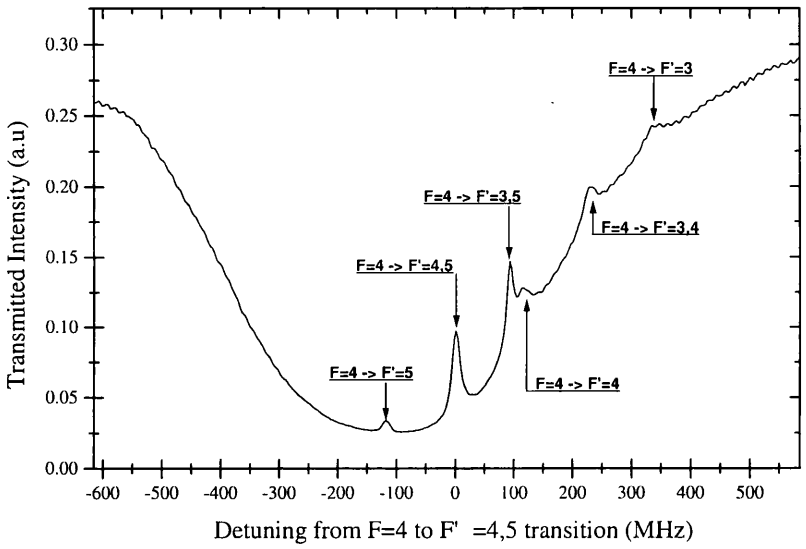

Figure 3.6: Caesium saturated absorption spectrum. Cooling transitions: $6S_{1/2}, F = 4 \rightarrow 6P_{3/2}, F'$.

A lock-in amplifier is used to extract the amplitudes of the different harmonics. The saturated absorption signal from the photodiode is fed to a lock-in amplifier, where a mixer is used to multiply all the Fourier components of the signal with a sinusoidal wave generated by an internal oscillator. The product of two sines with different frequencies is given by the sum of two sines, one oscillating at a frequency which is the sum of the two $(\omega_S + \omega_R)$ and one at a frequency which is the difference of the two $(\omega_S - \omega_R)$. When the reference signal generated by the oscillator has the same frequency as one of the harmonics of the input signal $(\omega_S = \omega_R)$, then one the two output sines oscillate at zero frequency while the other oscillates at $2\omega_R$. The output of the mixer is then sent to a low-pass filter which eliminates all the components oscillating at frequencies above the cut-off frequency of the filter. The output signal will then be proportional to the amplitude of the component at frequency ω_S through a coefficient which depends on the phase

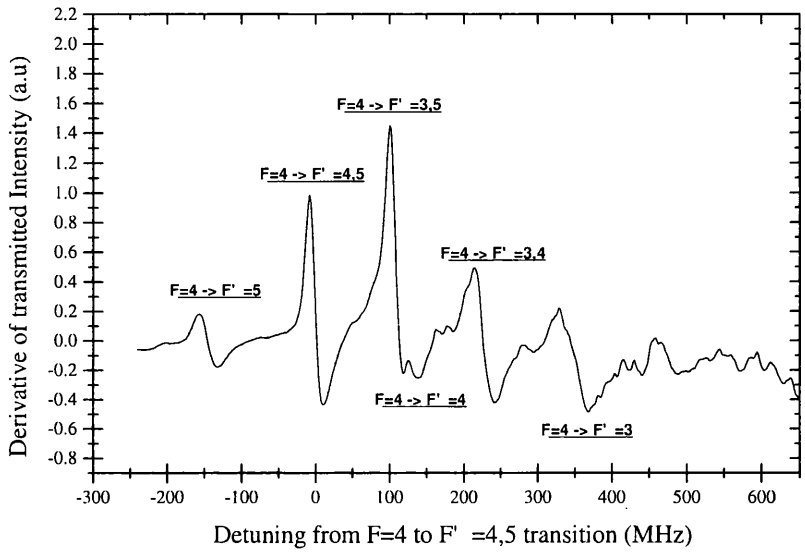

Figure 3.7: Derivative of caesium saturated absorption spectrum. Cooling transitions: $6S_{1/2}, F = 4 \rightarrow 6P_{3/2}, F'$.

difference between this component and the reference signal. By adjusting the lock-in phase it is possible to obtain a maximum correction signal and with the appropriate sign to oppose the frequency drifts of the laser source. For small values of m in equation 3.4 the output signal is the first derivative of the input signal, shown in figures 3.7 and 3.9 respectively, for the master laser and the repumper laser. The frequency modulation is obtained for the master laser through the acousto optic modulator and for the repumper by modulating the current. The saturated absorption signal is sent to a lock-in amplifier which outputs the first derivative of the input signal. The lock-in output is then sent to an integrating circuit which provides the correction to the laser. The correction is divided in a fast part which is added to the driving current of the diode and a slow part which is fed back to the piezo-electric transducer.

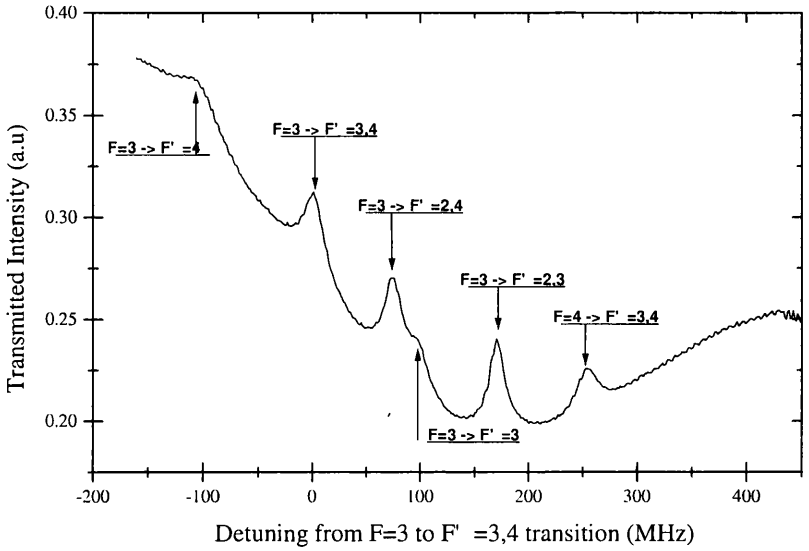

Figure 3.8: Caesium saturated absorption spectrum. Repumping transitions: $6S_{1/2}, F = 3 \rightarrow 6P_{3/2}, F'$.

3.5 Injection locking

The master laser, described in section 3.3, is frequency-locked to one atomic transition and is used to injection-lock two other 'slave' lasers, which will provide the trap light and near-detuned lattice light. The design of these lasers is shown in figure 3.10. The laser radiation is collimated, sent through an anamorphic prism pair to correct the ellipticity and then directed to an optical isolator. A slight misalignement of the anamorphic prisms generates a stray reflection which can be used as a monitor beam, as represented in the same figure.

It is possible to stabilize the emission frequency of a diode laser (slave) by injecting a small amount of light from another source (master) into the laser cavity. The master injecting laser forces the slave to oscillate at the same frequency and with the same spectral characteristics. The two oscillators are coupled so that

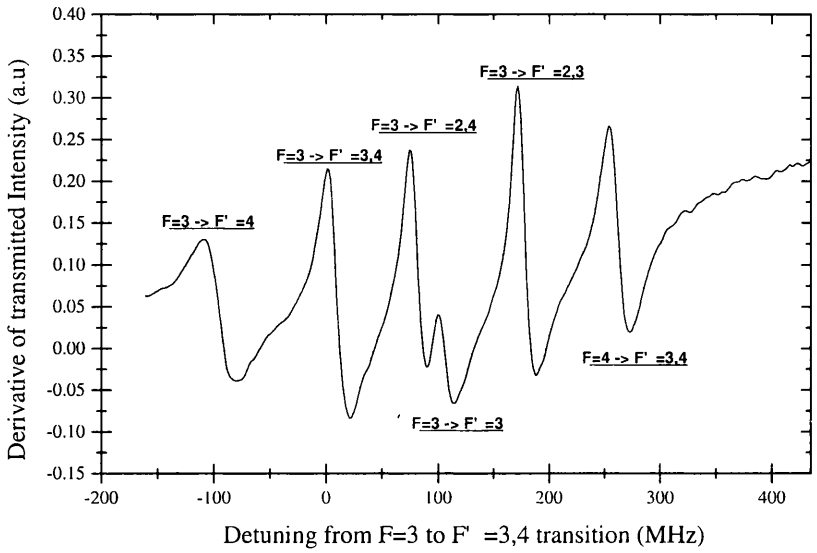

Figure 3.9: Derivative of caesium saturated absorption spectrum. Repumping transitions: $6S_{1/2}, F = 3 \rightarrow 6P_{3/2}, F'$.

the frequency and phase of their emitted radiation become strongly correlated. This technique is very useful since it generates a slave laser source stabilized in frequency without any loss in power, as no output light needs to be reflected back into the laser cavity.

The injection locking scheme is shown in figure 3.11. Each slave laser has an optical isolator on the output, which allows the injecting light into the diode cavity, but does not allow light from the slave laser to be coupled to the master cavity. The injecting beam is sent into the side entrance of the optical isolator with the right polarization, so that it is entirely transmitted into the slave cavity. In order to align the injection the input polarizer of the optical isolator was tilted a bit, so that a beam is emitted through the side output of the isolator. This beam was used to align the injection light to the slave beam. The stray reflection from the prisms shown in figure 3.10 is used to monitor the efficiency of the

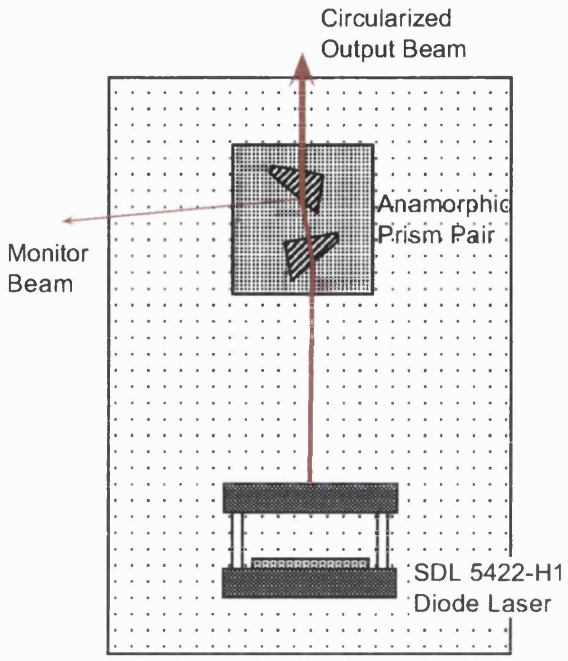

Figure 3.10: Slave laser design.

injection, by observing the variation of intensity transmitted through a caesium vapour cell as the current to the diode is ramped. When the injecting beam from the master laser is aligned, a dip in transmission of the monitor beam is recorded over a certain range of driving currents for the slave laser as it locks to the master frequency, which is tuned over a caesium absorption line, figure 3.12. The trap slave laser is injected directly from the master laser, whereas the near-detuned lattice slave laser has an acousto-optic modulator in a double pass configuration in the injecting beam (figure 3.11); this allowed us to reach larger detunings for the lattice light. In figure 3.2 the frequency scheme for the master, trap slave and lattice slave lasers is shown. In figure 3.13 a layout of part of the optical table shows how the trapping, repumper and near-detuned lattice beams are generated and locked to the desired frequency.

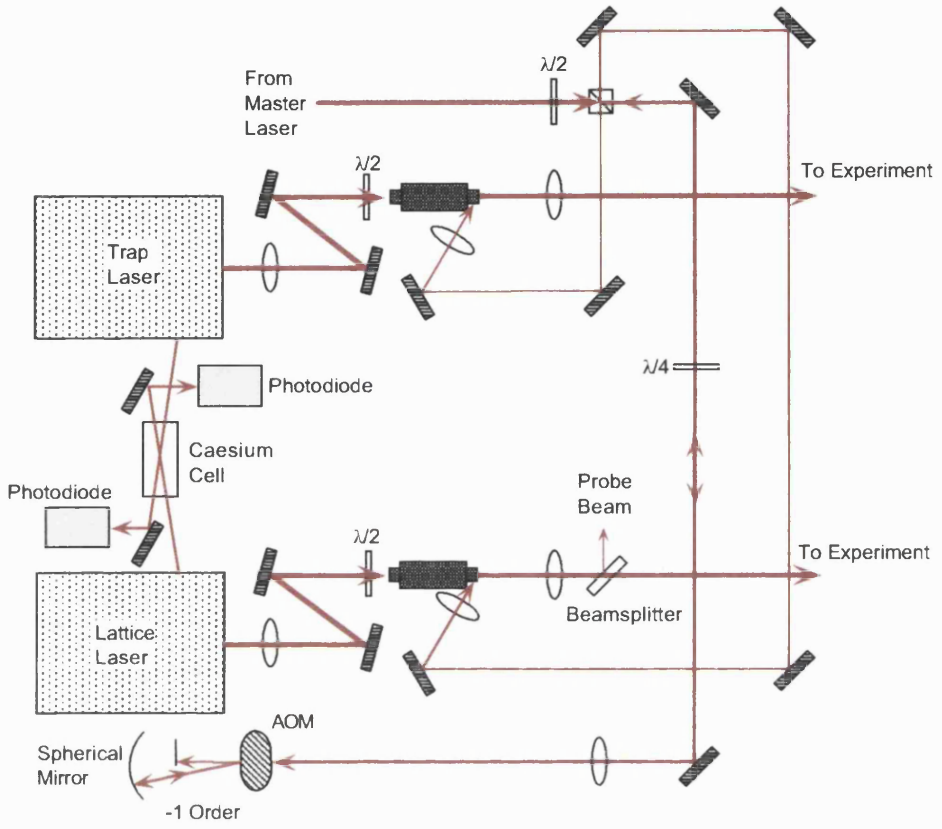

Figure 3.11: Injection locking scheme.

3.6 Master Oscillator Power Amplifier

In order to generate the intensity needed for the far-detuned lattice to have the same potential depth as the near-detuned one, while being hundreds of times further detuned, a Master Oscillator Power Amplifier (MOPA) was used [25], [26], [27]. A MOPA system is used to amplify the light coming from a narrow linewidth master oscillator, so that the output light has increased intensity and the same spectral features as the injecting light. A strained quantum well distributed Bragg reflector (DBR) laser diode was used as master oscillator. These lasers have a narrowed linewidth output, due to a grating structure which is grown

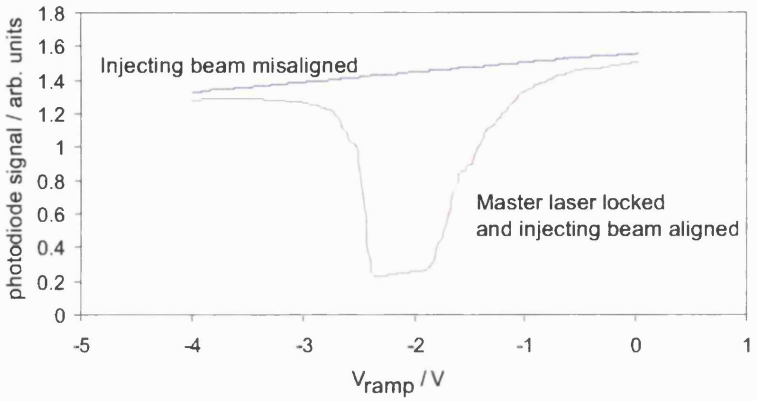

Figure 3.12: Injection locking signal. The upper trace shows the variation in the power transmitted through the caesium cell when the slave current is ramped but the laser is not injecting, the lower trace shows the absorbtion of the beam when the laser is injection locked

within the gain medium, which behaves as a high reflectivity surface, selective in wavelength. Therefore, only the wavelengths that satisfy the Bragg condition can oscillate in the laser cavity. At the same time they are continuously tunable over a range of several gigahertz, without having the mode-hops associated with an external cavity. The power amplifier consists of a tapered gain element which is pumped with high current, typically 1.5 A. The tapered amplifier output spectrum is typically very broad, but it can be narrowed by feedback from an external cavity or by injecting light from a narrow linewidth master laser, when it operates as a single pass optical amplifier (MOPA). In this way it is possible to achieve an output with the same spectral characteristics as the master laser at an intensity which can be up to two orders of magnitude greater, resulting in a power of up to 0.45 W.

The scheme of the mounts and optics needed for the tapered amplifier are shown in figure 3.14. Short focal length (3.1 mm), high numerical aperture (0.6) aspheric lenses are used to couple the injecting light in and the amplified light out. These lenses are placed on mounts to control x, y, z positioning. The whole

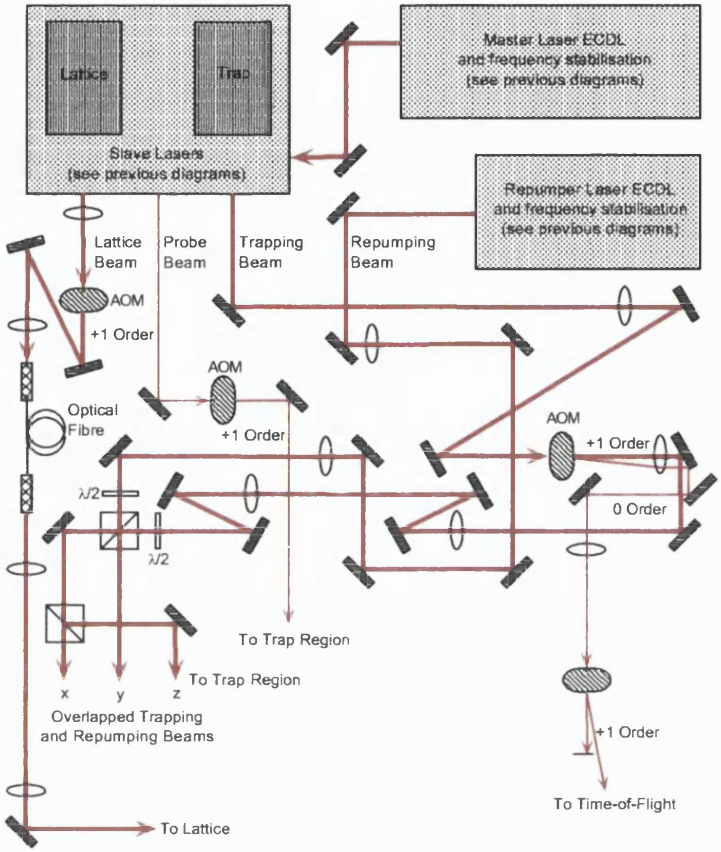

Figure 3.13: Layout of the optical bench.

mount is temperature stabilized by means of a control unit which drives a Peltier element positioned on a water-cooled heatsink.

The output of the front and back facets of the tapered amplifier (TA) were collimated by positioning the aspheric lenses in the three dimensions. The amplified spontaneous emission beam emitted from the back facet was retro-reflected into the TA and the output power was monitored to optimize the lens positioning; maximum output was achieved when the reflected light was best collimated and injecting the amplifier. The master light was then aligned to the spontaneously emitted light from the back facet. The injection was improved by ensuring that

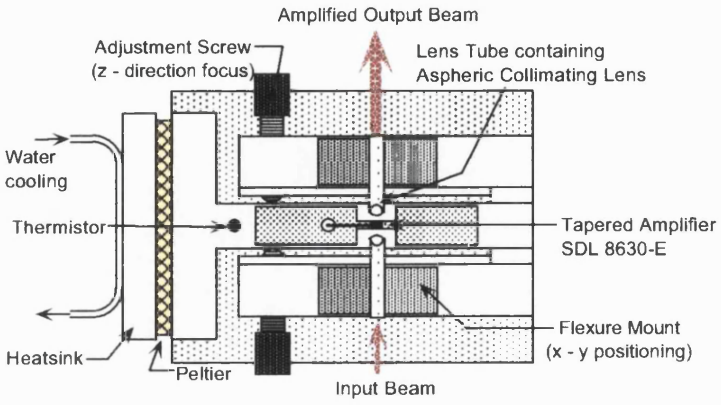

Figure 3.14: Tapered amplifier mount design.

the polarization is parallel to the plane of the taper of the amplifier and by correcting the shape of the injecting beam using an anamorphic prism pair, as shown in figure 3.15. The output of the tapered amplifier is highly astigmatic. The output coupling lens is used to collimate the beam in the vertical direction only. A cylindrical lens external to the mount is then used to correct the horizontal astigmatism. Optical isolators are used to provide 100 dB isolation between the TA and the DBR in order to prevent optical feedback into the master cavity.

3.7 Magnetic fields

To trap atoms in a magneto-optical trap a inhomogeneous magnetic field is needed, such that it is null at the center of the intersection region of the laser beams and increases linearly along each of the three cartesian directions. This field is generated by a pair of coils in an anti-Helmholtz configuration, i.e. with current flowing in opposite directions, which are placed around the cell with their common axis along the vertical direction. The coils are made of 150 turns of copper wire wrapped around a square support of 8 cm side. The coils are placed at a distance of 7 cm, which gives the most uniform field gradient at the center of the trap.

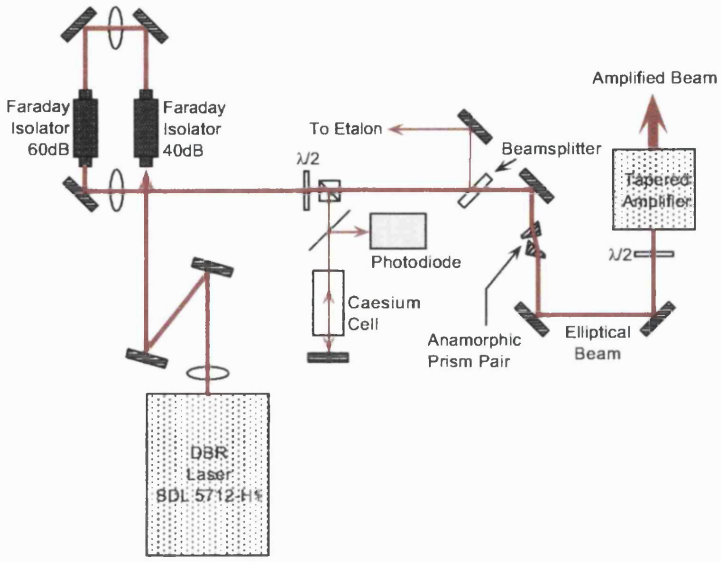

Figure 3.15: MOPA system consisting of a DBR and TA.

The magnetic field gradient along the vertical direction is $\partial B/\partial z \simeq 4 * I/A$ G/cm, where I is the current through the coils. The magnetic field gradient along x and y is half the value of the gradient along the z axis and of opposite sign.

To make sure that the magnetic field is null at the center of the intersection region of the laser beams, it is necessary to compensate for the terrestrial magnetic field and for all the stray fields which are present in the laboratory. This is achieved by using three pairs of square Helmholtz coils, all of the same dimensions, placed around the cell to form a cube of 50 cm side. These coils can provide a sufficiently uniform magnetic field in three directions, which can be finely tuned with an accuracy of a few milliGauss.

3.8 Time-of-Flight setup

The time-of-flight method described in [30],[31] was used to determine the temperature of the atoms when they are released from the lattice. This technique

consists of releasing the cloud of atoms from the lattice and letting it expand, due to the thermal motion of the atoms, and to fall under gravity. After 110 ms from their release the atoms pass through a thin probe beam which is placed 6 cm below the trap, orthogonal to the gravitational axis. A photodiode detects the absorption of the probe beam as the atoms pass and different arrival times can be recorded. This distribution can then be converted to a momentum distribution, from which the temperature can be inferred. The experimental setup

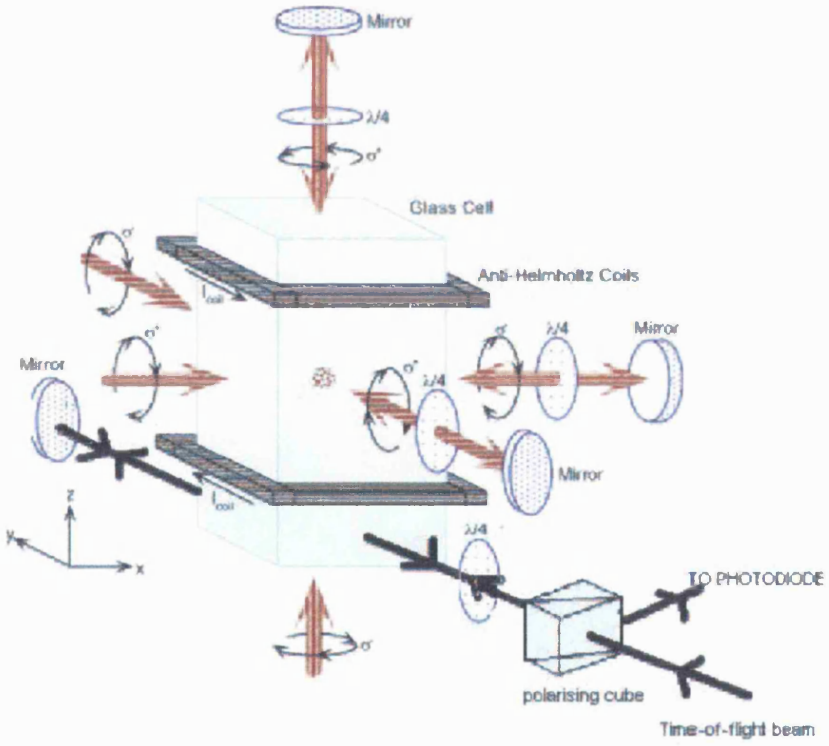

Figure 3.16: Layout of the cell in which the trap is formed, with trap beams, coils and the time-of-flight setup.

for a time-of-flight detection is shown in figure 3.16, where the layout of the cell in which the trap is formed and the position of the various coils are also shown. The time-of-flight setup consists of a near resonant beam, $\leq$ 1 mm thick and 1 cm wide, which is retro-reflected to avoid any systematic momentum transfer. A combination of polarising cube and two wave-plates allows the selection of the polarisation of the two counter-propagating beams. Typically this is set to be circular (σ^+/σ^+) polarized, but for the Stern-Gerlach experiments (see chapter 6), these were set to linear. The cloud of atoms, following its release from the lattice and its subsequent fall, passes through this layer of light and absorbs it. A typical signal generated with a time-of-flight measurement is shown in figure 4.2.

In determining the temperature it is assumed that the initial spatial density distribution of the cloud is a Gaussian function of the position

$$\rho_r(\mathbf{r}) \propto \exp\left(-\mathbf{r^2}/\sigma_\mathbf{r}^2\right)$$

and that the momentum distribution is a Maxwell-Boltzman

$$\rho_p(\mathbf{p}) \propto \exp\left(-\mathbf{p^2}/\sigma_\mathbf{p}^2\right) \propto \exp\left(-\mathbf{p^2}/(\mathbf{2m_{Cs}k_BT})\right)$$

with $k_BT = m_{Cs}v_{rms}^2$. Using kinetic theory it is straightforward to calculate the size of the atomic cloud after a time t from its release, while it is assumed that there is no change in the momentum distribution, i.e. no heating is present. Taking also into account the finite size of the probe beam, the solution for the temperature gives the following expression, as a function of the (temporal) $1/\sqrt{e}$ half-width w_{fin} detected from the time-of-flight signal:

$$T = \frac{m_{Cs}}{k_B}\left(g^2 w_{fin}^2 - \frac{\sigma_{ini}^2 + \sigma_{TOF}^2}{t_{drop}^2}\right), \tag{3.5}$$

where t_{drop} is the time it takes the atoms with zero velocity to reach the probe beam, σ_{ini} is the initial half-width at $1/\sqrt{e}$ of the cloud's spatial distribution and σ_{TOF} is the half width at $1/\sqrt{e}$ of the intensity distribution of the probe beam

along the vertical axis. From equation 3.5 it is possible to see that the resolution of the method is limited by the initial size of the cloud and the vertical thickness of the TOF beam. In the limit of infinite t_{drop} the second term of equation 3.5 goes to zero, but for finite dropping time (110 ms in our case) for a $\sigma_{ini} = 0.5$ mm and $\sigma_{TOF} = 0.5$ mm, the term yields a resolution limit of about 0.7μK. Thus no temperature below this limit can be measured. The initial size of the cloud as well as the size of the TOF beam are measured by imaging using a CCD camera. These measurements have significant errors, which result in an uncertainty on the temperature determination of 0.2μK. Furthermore the fitting procedure leading to the determination of w_{fin} is usually limited by noise, but the error associated with it is usually an order of magnitude less then the one in determining the size of the cloud and TOF beam by imaging.

3.9 Computer-automation of the system

Due to the typical time-scales involved in the various trapping and cooling cycles, a laser-cooling experiment necessitates a fully electronic control. Strict control of the timing of the different stages of the experiment is required, down to the typical time-scales of the system under investigation and this has to be done in a highly reproducible fashion. I therefore designed and developed a computer program to control all the devices through the channels of an AT-AO-10 and PCI-6800 data acquisition boards (National Instruments). The two boards are synchronized through an RTSI connector. I used Labview software packages which provides a graphical programming language (G) and many libraries for instrument control and data acquisition.

The main function of the program is to write an array of values to the analogue channels which are then output at a specified rate. In this way it is possible to control the signal sent to each channel with a resolution of 10 μs. At the moment

fourteen different devices can simultaneously be controlled, which allow us to change the frequency of the lasers, their intensities, the current of the magnetic coils and to control mechanical shutters. A user interface allows the setting of the duration of each phase of the experimental sequence as well as the setting of the different parameters at the beginning of each session. The code has been revised several time during the course of these three years, but it now allows the setup of experiments involving the control of up to eighteen channels simultaneously and to programme up to fifteen different phases from the front panel. It is therefore very flexible and easy to use.

3.10 Conclusions

In this chapter I described the experimental apparatus which was used for the experiments presented in this thesis. An overview of the methods used to frequency-stabilize the lasers and to narrow their bandwidth was presented. The different laser sources are also described, as well as the coils which were used to produce static magnetic fields. Finally, I gave a description of the computer program that I developed in order to automate the experiment.

CHAPTER 4

Atoms in a Far-Detuned Optical Lattice

In this chapter I will describe the preparation of atoms in a nearly dissipation-free optical potential, which is obtained by using light tuned a few thousand linewidths to the low frequency side of the D_2 atomic resonance of caesium. In the near detuned regime, the scattering rate involved in cooling is also responsible for decoherence effects and a reduced lifetime of the vibrational states. Cold neutral atoms in a far-detuned optical lattice may offer a long coherence time because of the reduced spontaneous scattering rate and their weak coupling to the environment. In principle it is possible to reduce arbitrarily the scattering rate by increasing the detuning of the laser beams. In the limit of large detuning, in fact, the scattering rate is proportional to $\frac{I}{\Delta^2}$, while the potential depth results to be proportional to $\frac{I}{\Delta}$. By simultaneously increasing the detuning the intensity of the laser beams forming the lattice in an appropriate manner, it is possible to almost completely suppress the scattering rate, while maintaining a deep enough potential well. For the typical parameters of the far-detuned lattice used in our experiment, the spontaneous scattering rate is in the range of 50 – 1000 Hz, for

a characteristic vibrational frequency of $\simeq 30 - 40$ KHz, which has to be compared with the typical scattering rate in a near-detuned lattice of $\simeq 500KHz$ for the same potential depth. Therefore the atoms trapped in the potential wells of a far-detuned optical lattice, can oscillate several periods before a spontaneous scattering event occurs. The non-dissipative nature of such lattices should allow the preparation and manipulation of pure quantum states, thanks to the increased life-time of the vibrational states. At the same time, the reduced scattering rate in a far-detuned lattice (FDL) leads to absence of built-in laser cooling and makes it necessary to load a sample of atoms previously prepared in a near-detuned lattice (NDL). In the NDL the features of the periodic structure are built. In the first section of this chapter the loading of the near-detuned lattice is presented. Following the characterization of the near-detuned lattice, atoms are transferred to a super-imposed lattice induced by light tuned far from resonance, in which they can be tightly bound in a dissipation-free potential. An analysis of the transfer efficiency and storage times is performed, to optimize the loading. Experiments are also performed to gain information on the population distribution over different vibrational levels.

4.1 Preparation of a cooled sample in a near-detuned optical lattice.

The sample of atoms is firstly collected by a magneto-optical trap (MOT), as described in section 3.2. The magnetic field gradient typically used for the MOT is 6 G/cm, the intensity of the laser beams typically (3.5 ± 0.1) mW/cm^2 with a detuning of 2.5Γ from the $F = 4 \rightarrow F' = 5$ transition. The magneto-optical trap configuration is typically left on for 2 sec, which was found to be the characteristic loading time to collect a sample of $\simeq 8 \cdot 10^8$ atoms. The magnetic field gradient is then switched off, the detuning increased and the intensity decreased. The atoms

are left to cool further in an optical molasses, typically tuned $\sim 6\Gamma$ from resonance and with reduced beams intensity, which is set to $\simeq 1.8$ mW/cm^2 per beam. These parameters were chosen in order to minimize the temperature and maximize the number of atoms trapped. The temperature of the atoms was measured with the time-of-flight method, described in section 3.8, and was found to be typically $\leq 10\mu$K.

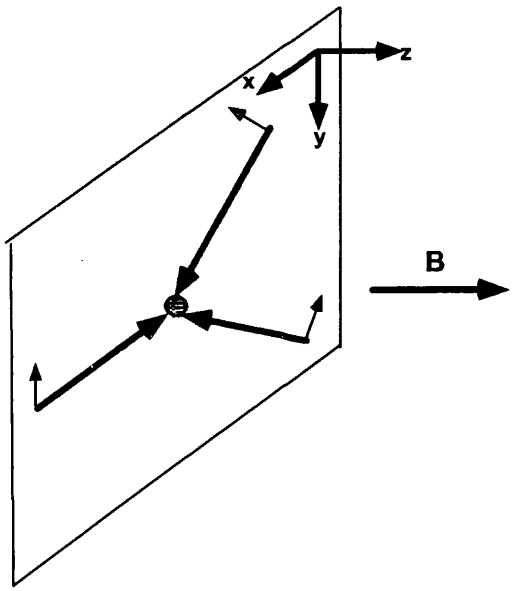

Figure 4.1: Representation of the lattice plane and quantization axis.

Atoms so prepared, were then transferred to a 2D near-detuned lattice. The configuration used was the one described in section 1.2.3, and consists of three co-planar laser beams, all with linear in-plane polarisation, propagating at 120° with respect to each other. The gravity axis lies on the plane of the lattice, as shown in figure 4.1. This allows us to measure the kinetic temperature along one of the two lattice dimensions. The intensity and detuning were varied to achieve a colder sample and to better transfer the atoms to the far-detuned lattice. In figure 4.2 the TOF spectrum for a near detuned lattice is shown: the single beam

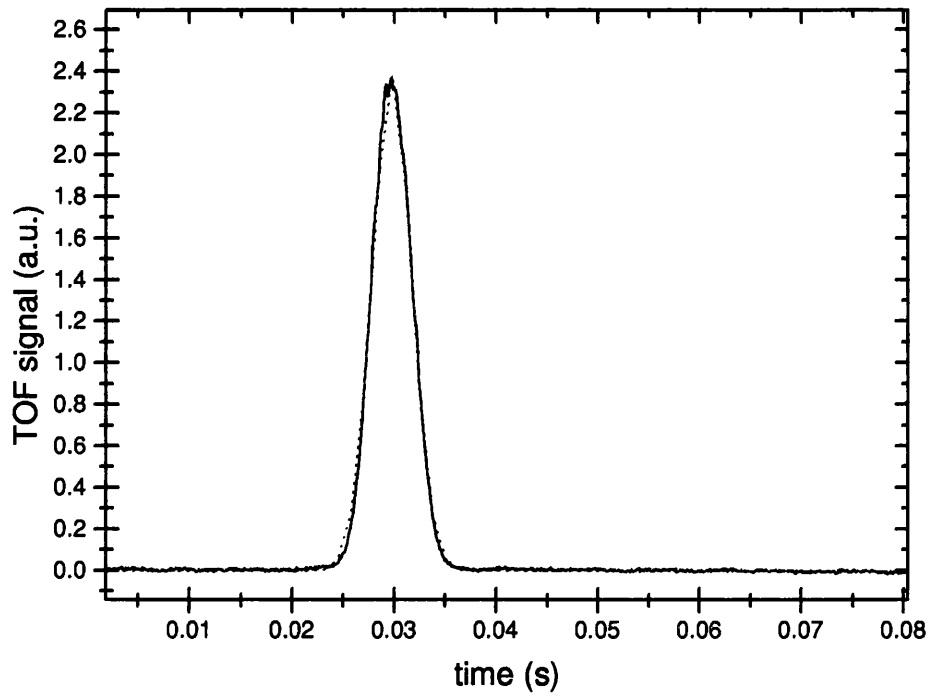

Figure 4.2: TOF signal of the near detuned lattice and Gaussian fit (dotted line) to extract the temperature.

intensity was set to 3 mW/cm^2 and the detuning was set to 26Γ to the red of the $F = 4 \rightarrow F' = 5$ transition. A Gaussian fit of the signal was performed in order to estimate the temperature of the sample, using equation 3.5. The measured temperature extracted from the spectrum in figure 4.2 was found to be (3.5 ± 0.2) μK. Lower temperatures were found to be achievable, down to the lower limit of $\simeq 3$ μK. A careful adjustment of the current to the compensation coils was found to be very crucial in order to minimize the temperature, as discussed in [32].

To gain an insight into the localization of the atoms and the quantization of the vibrational modes in the potential wells generated by the ND lattice, probe transmission spectra were taken. A weak probe beam, with a typical intensity of 0.2 mW/cm^2, is sent through the optical lattice, at a small angle with one of the

lattice beams, with a polarisation parallel to that of the nearly co-propagating lattice beam. The frequency of the probe beam is swept by ramping the RF to an acousto-optic modulator, and the transmitted intensity is recorded.

An atom confined in a potential well should exhibit a discrete spectrum of vibrational energy levels, like a harmonic oscillator. The lattice beam (acting as a pump light) together with the probe beam can induce stimulated Raman transitions among such levels. When the difference in frequencies between these two stimulating sources corresponds to the separation between two vibrational levels, Raman resonances arise. For i) $\omega_{probe} - \omega_{lattice} < 0$, this corresponds to a net gain in the transmission of the probe, while for ii) $\omega_{probe} - \omega_{lattice} > 0$, it results in a net absorption of the probe. In any case the probing light is both absorbed and emitted, but the net effect depends on the population of the levels involved. In case i) if the pump beam excites the population of level n the probe has to stimulate the emission and decay to $n+1$ ($\omega_{probe} < \omega_{lattice}$) or if it is the probe to excite from level $n+1$, then the pump has to stimulate the de-excitation to n. As level $n+1$ is less populated than level n, this would result in a net gain for the probe beam, as shown in figure 4.3. A similar argument explains the absorption of the probe when its frequency exceeds that of the lattice light.

From these considerations, we should expect to see simmetric resonances in absorbtion and gain when the difference in frequency between pump beam and probe beam equates the separation between the vibrational levels in the lattice. In figure 4.3 the probe transmission intensity is plotted versus the detuning of the probe beam with respect to the lattice beam. This spectrum was taken for a detuning of the lattice $\Delta_{latt} = -4.4\Gamma$, and an intensity $I_{latt} = (2.0 \pm 0.1)$ mW/cm^2 per beam. Two peaks can be distinguished at $\delta_{probe} = \pm 70$ kHz, which correspond to the vibrational frequency associated with the lattice potential. A small Rayleigh feature is also visible at $\delta_{probe} = 0$. This was regarded as a proof of the localization

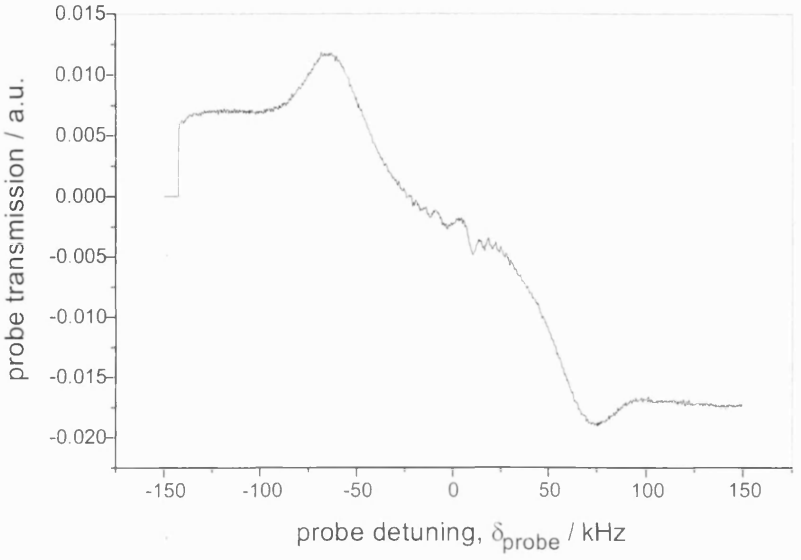

Figure 4.3: Probe transmission spectrum through a 2D lattice. The intensity of the lattice beams was $2.0 \pm 0.1 \mathrm{mWcm}^{-2}$, of the probe beam $0.2 \mathrm{mWcm}^{-2}$, detuning -4.4Γ, and the duration of the scan 4ms. The resonances at $\pm 70kHz$ correspond to the main vibrational frequency.

and of the existence of quantized vibrational levels for the atoms in the optical lattice. It was also used as a tool to measure the frequency of oscillation of the atoms at the bottom of the potential wells.

4.2 Loading the Far-detuned Optical Lattice

In a near-detuned optical lattice, control of the center-of-mass motion is limited by heating processes which occur at a rate determined by the scattering of photons. It is possible to create a new kind of lattice where the heating processes are almost completely suppressed. In the limit of large detuning the scattering rate is proportional to $\frac{I}{\Delta^2}$ and it is therefore possible to reduce the dissipative processes by increasing the detuning Δ of the laser source to be very far from resonance. At the same time, in order to generate a deep enough potential well, the intensity of the

laser source must be adequately increased, as the potential depth is proportional to $\frac{I}{\Delta}$. Particular care has to be taken during the transfer from the near-detuned lattice, where the atoms are first cooled and localised, in order to guarantee that a good degree of localization is maintained. For this reason it is necessary to finely control the intensities of the two sets of beams in order to ensure a matching of the vibrational frequencies of the near-detuned and far-detuned lattice and to adjust the difference in path length for the both lattices beams, in order to guarantee a matching in the the relative spatial phase of the lattices beams. In this section I will describe the experimental setup and the loading technique which was employed to transfer the atoms from the near-detuned lattice to the far-detuned one.

4.2.1 Far-Detuned Optical Lattice Setup

Shown in figure 4.4 is the setup that was used to overlap the far-detuned lattice beams with the beams of the near-detuned one. A combination of polarising cubes and quarter-wave plates are used to create three equally intense beams for the near detuned and far-detuned lattice. In section 1.2.3 I discussed how changes in the relative phases of the laser beams can produce a translation of a N-dimensional lattice, generated by $N+1$ beams. For a good transfer among the lattices, it is very important that the maxima and minima of the near-detuned and far-detuned lattice overlap, a mismatch resulting in heating and loss of the atoms. This means that the spatial phase difference among the beams must be the same in the NDL and FDL: this can be guaranteed if the difference in path length between different beams is matched at the two optical frequencies . If two beams of the lattice traverse path lengths l_1 and l_2 before intersecting in the lattice region, then the spatial phase difference, which determines the position of minima and and maxima of the potential, of the near-detuned (ND) and far-detuned (FD) lattice beams at the point of intersection is $\delta\phi_{ND} = k_{ND}(l_2 - l_1)$

and $\delta\phi_{FD} = k_{FD}(l_2 - l_1)$. In order to guarantee a good overlap between the two potential wells, it is necessary to ensure that $\delta\phi_{ND} - \delta\phi_{FD} \ll \pi$. It follows that $\delta l \ll \frac{c}{2(\nu_{ND}-\nu_{FD})}$ must be satisfied. For the typical values of the experiments $\nu_{ND} - \nu_{FD} \simeq 10$ GHz, which gives an upper limit on δl of only a few millimeters. In order to match this requirement, the two retro-reflecting mirrors in the beam paths are mounted on micrometer adjustable translation stages, as shown in figure 4.4, which can be adjusted monitoring the number of atoms loaded and their temperature for optimization. The intensities of the near-detuned and far-detuned

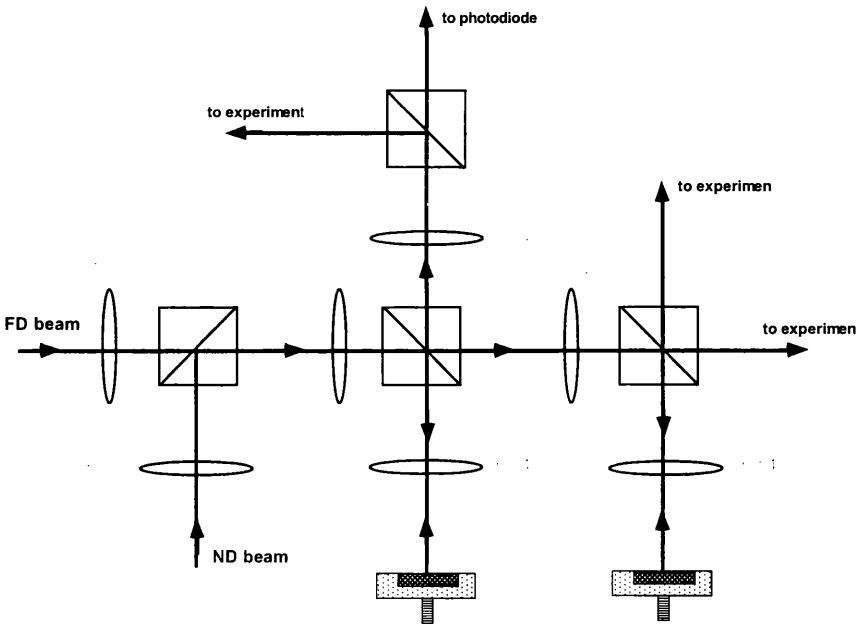

Figure 4.4: Experimental setup to overlap far-detuned and near-detuned beams to form the lattice.

beams are controlled separately by two acousto-optic modulators. For the near-detuned lattice the first order diffracted beam allows the continuous variation of the intensity of the beam, while, for the far-detuned case, the zero order non-deflected beam is chosen, thus necessitating the use of a mechanical shutter to completely extinguish the light. In this way it is possible to finely change the

intensity from I_{max} down to approximately $0.2 \cdot I_{max}$ and use the shutter to turn the light completely off.

The far-detuned lattice is generated by a MOPA system pumped by a DBR laser, described in section 3.6. This is capable of an output power of up to 0.45 W. The output beam, though, has a poor spatial quality and a pinhole was used to spatially filter the beam and correct its profile. This causes 50% of the power to be lost. Other sources of power loss are the various optics placed in the laser path, the acousto-optic modulator, used to control the intensity of the beams, and the optical isolator, placed at the laser output to avoid feedback. As a result, the maximum single beam power obtainable is 25 mW. This constitutes the greatest limitation of the experimental setup, and it will be found to affect most of the measurements presented in the following sections. Ideally, in order to have a well working lattice, with isotropic properties over all spatial extent, the light intensity should be uniform over the spatial region where the lattice is built, so that atoms at different locations experience the same potential depth. This could be achieved by expanding the lattice beam and selecting the central most uniform intensity region, but this would have caused further loss of power, which could not be allowed. The profiles of the far-detuned lattice beams were imaged along both the two dimensions and were, in fact, found to be non-uniform over the cloud spatial extent. As it is shown in figures 4.5, 4.6 the full width at 90% intensity is $\simeq (1.0 \pm 0.1)$ mm in the horizontal direction and $\simeq (0.45 \pm 0.06)$ mm in the vertical direction, which was smaller than the extent of the cloud released from the near-detuned lattice. As it will be shown in the next chapter, this causes inhomogeneity on the potential depth and a spread in the characteristic vibrational frequency of the atoms trapped at different lattice sites, as the measurements revealed when the lattice was parametrically excited (see chapter 5). This will also affect the efficiency of resolved-sideband Raman cooling, where the spread in

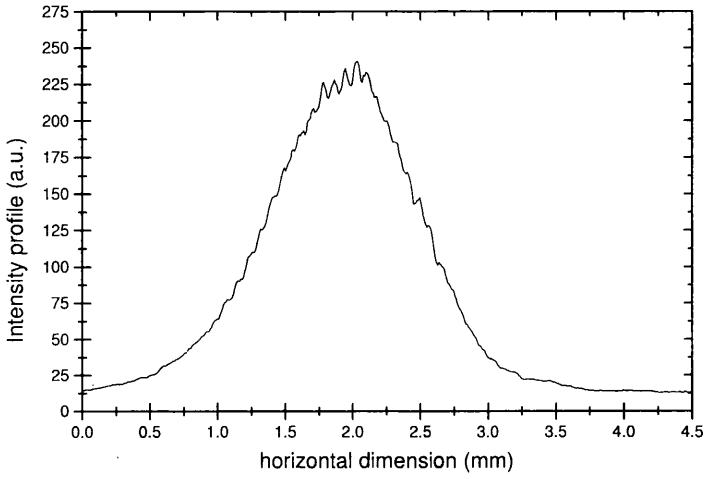

Figure 4.5: Intensity profile of the far-detuned beam along the horizontal direction.

vibrational frequencies is expected to broaden cooling resonances such that they are no longer resolved, see chapter 7. In the Stern-Gerlach experiments (chapter 6) a reduction in the net fictitious field experienced by the ensemble of atoms was partly attributed to the inhomogeneity of the potential depth. A more powerful laser source is therefore needed for the optimization of the experiment.

A typical sequence for the far-detuned lattice loading proceeds as follows: the atoms are first loaded in a near-resonant lattice where they are cooled down to a few microKelvin and trapped in the wells of the optical lattice. Typically, the near-detuned lattice is generated by light tuned up to $\Delta = -26\Gamma$ to the red of the $F = 4 \rightarrow F' = 5$ transition, with a maximum intensity of 3 mW/cm^2 per beam, the size of the beams being $\simeq$ 1 cm^2 . The intensity and detuning were varied in order to control the potential depth, according to the fact that the light shift is proportional to $\frac{I}{\Delta}$ (see previous paragraph). The far-detuned super-imposed lattice must generate the same light shift in order to keep the strong confinement and the same degree of localization as the near-resonant potential; therefore, while

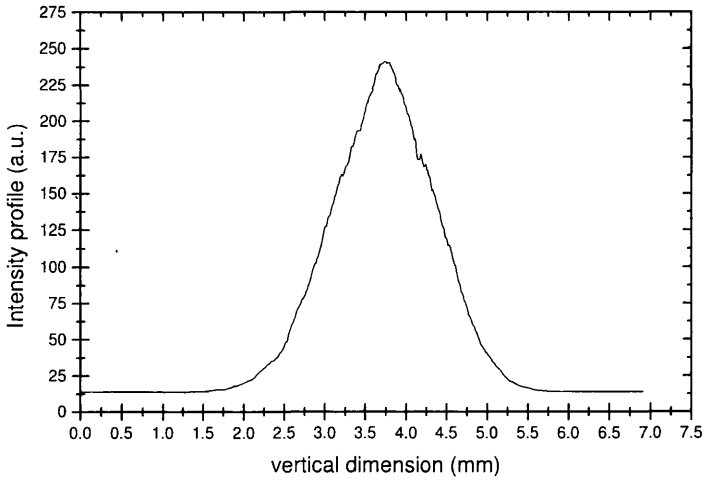

Figure 4.6: Intensity profile of the far-detuned beam along the vertical direction.

increasing the detuning in order to decrease the scattering rate, the intensity of the beam must be raised to maintain the same potential depth. The detuning was varied in the range $1000 - 4500\Gamma$, the maximum equivalent intensity achievable in our setup being $\simeq 500$ mW/cm^2 per beam. This equivalent intensity is obtained by considering the intensity distribution as uniform and assuming an equivalent area given by the product of the FWHM of the intensity profile along the two dimensions.[1] The typical vibrational frequencies for these values of intensity and detunings were in the range $30 - 45$ kHz and the scattering rate below 1000 Hz. The far-detuned lattice parameters were first theoretically estimated in order to match the potential depth and vibrational frequency of the near-detuned lattice and were afterwards tested by using the parametric excitation method, described in chapter 5. The transfer of atoms from the near-detuned to the far-detuned lattice is accomplished by simultaneously controlling the intensities of the two laser beams. This is done in order to ensure the tight binding of the atoms for the

[1] I will use this parameter to characterize the lattice from now on and, when possible, I will include the full spatial profile of the beams

whole duration of the transfer. By linearly changing the intensities of the NDL and FDL in a way that the sum of the depths of the two potentials is approximately the same during the transfer, the atoms would feel no variation in the apparent potential, thus maintaining localization. The duration of the transfer was typically $400 - 500$ μs. The duration was varied in order to optimize the transfer efficiency, by monitoring the temperature and number of atoms in the loaded sample.

4.2.2 Studies of transfer efficiency and losses in the far-detuned lattice

A typical sequence of the experiment starts with the loading of the atoms in a near-resonant lattice where they are prepared in the lower states of motion by Sisyphus cooling processes. The near-detuned lattice is typically left on for 5 ms, which is enough to cool the atoms down to a few μK in the two dimensions of the lattice and at the same time short enough for the atoms not to escape in the direction orthogonal to the lattice plane, due to their velocity in the z-direction. Following that the intensities of the two beams are simultaneously ramped, in order to ensure tight binding transfer. The intensity and detuning of the far-detuned lattice were varied in order to match the potential depth of the near resonance potential.

In figure 4.7 two time-of-flight spectra are shown for two different durations of a far detuned lattice, $t_{FD} = 10$ ms and $t_{FD} = 70$ ms. The intensities of the beams were set to (400 ± 50) mW/cm^2 and the detuning $\Delta = (-4500 \pm 100)\Gamma$, giving a scattering rate of $\Gamma_s \simeq 50$ Hz. In these spectra, two peaks are evident, separated in time by $\Delta t = 10$ ms and $\Delta t = 70$ ms, i.e. times equivalent to the far-detuned lattice duration. The first Gaussian peak is very clear in the spectrum taken for a 10 ms duration of the far-detuned lattice. Due to the smaller spatial extent of the FD beam with respect to the ND one, a fraction of the atoms which were stored in the near-detuned potential are never trapped by the FD light; these

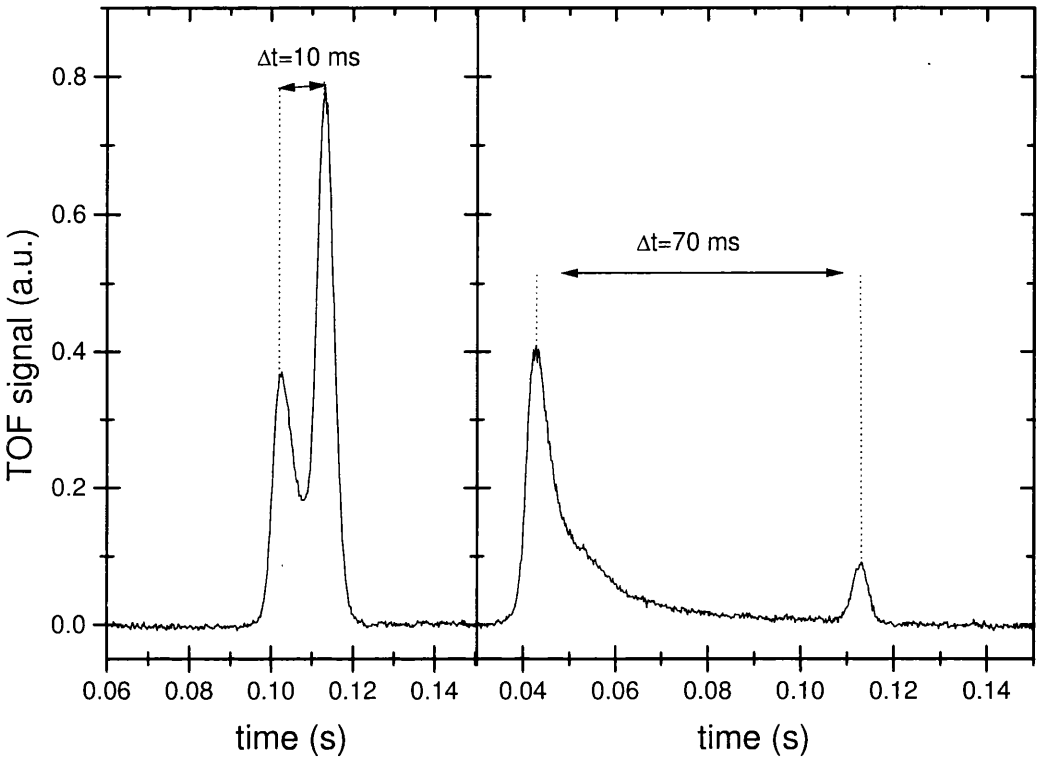

Figure 4.7: TOF signal obtained for two different loading times for the far-detuned lattice.

atoms start falling as soon as the ND light is replaced by the FD. The separation of the two peaks corresponds in fact to the duration of the FD lattice. Further losses of atoms are detected as a decaying tail between the two peaks. Thus atoms leaking out of the far-detuned lattice at later times are detected as a decreasing tail between the two Gaussians.

Measurements were performed in order to determine the lifetime of the FD lattice, by measuring the number of atoms trapped for different time durations. In figure 4.8 the decay is reconstructed by plotting the area under the Gaussian peak for different storage times. This curve is characterized by an initial fast decay followed by a slower decay. The trend is best fitted with a sum of two exponential

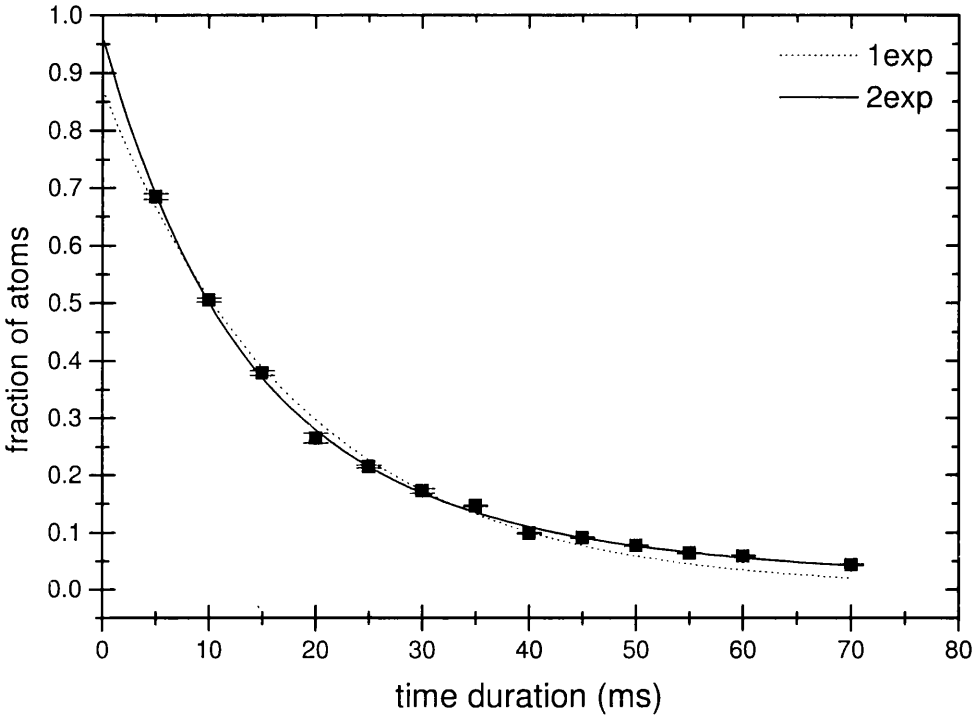

Figure 4.8: Life-time measurement for the far detuned lattice. The dotted curve represents the fit to a single exponential and the solid curve represents the fit to a sum of two exponentials, which gives two characteristic times $t_1 = (13 \pm 2)ms$ and $t_1 = (50 \pm 10)ms$.

decays, which betray the existence of two characteristic times: a short one of (13 ± 2) ms and a longer one of (50 ± 10) ms.

These losses can be attributed to several mechanisms, also found responsible for losses in 3-D blue detuned optical lattices [33]. At long times, transverse motion of the atoms in the lattice plane, which is increased by scattering of spontaneously emitted photons, allows the escape from the trapping region. At shorter times, highly energetic atoms, which are not tightly bound, diffuse through the lattice to regions of shallower wells and can be excited out of the lattice, due to heating induced by laser beams intensity fluctuations.

Spontaneous emission as well as laser noise heat the atoms, so that atoms

in bound vibrational levels are transferred to higher energy, nearly free states, and are therefore lost after some time. The low scattering rate for these lattice parameters, $\Gamma_s \simeq 50Hz$, suggests that the effect of spontaneous scattering is relevant at long times. The 'long' characteristic time was found to slightly decrease by decreasing the detuning of the laser source, which is consistent with attributing the losses to heating induced by scattering. Another mechanism of escape is linked to the diffusion of unbound atoms towards regions of shallower light-shift potential. The non-homogeneous spatial profile of the beam intensity over the lattice region suggests that this may be contributing to the loss of atoms. Furthermore, if the cooling during the near-detuned phase was not efficient atoms which are too hot tend to populate the higher lying vibrational levels, which, as discussed in chapter 2, have a significant curvature and broadening. This curvature in the bands means that the atoms are not tightly bound and can therefore be excited out of the lattice more easily. As said above, excitation may be provided at short times by intensity fluctuations of the laser source. Such phenomenon will be discussed in section 5.4, where an estimate of the noise induced heating is given. It will be shown that intensity noise only produces a small heating of the sample at short times ($\simeq$ 10 ms), which is however enough to excite out of the lattice the most energetic atoms. This would also suggest that at short times the atoms from the higher bands are more easily lost, making the loss mechanism band-dependent. This idea found support from the analysis of the temperature of the sample at different storage times, see section 4.3.

In order to investigate further the loss mechanisms, the temperature of the sample was also monitored, for different durations of the far-detuned lattice. In figure 4.9 the variation of the temperature as a function of storage time is reported. The decay of temperature with time provides evidence for the band-dependence of the loss mechanisms, which causes the population of the excited bands to die

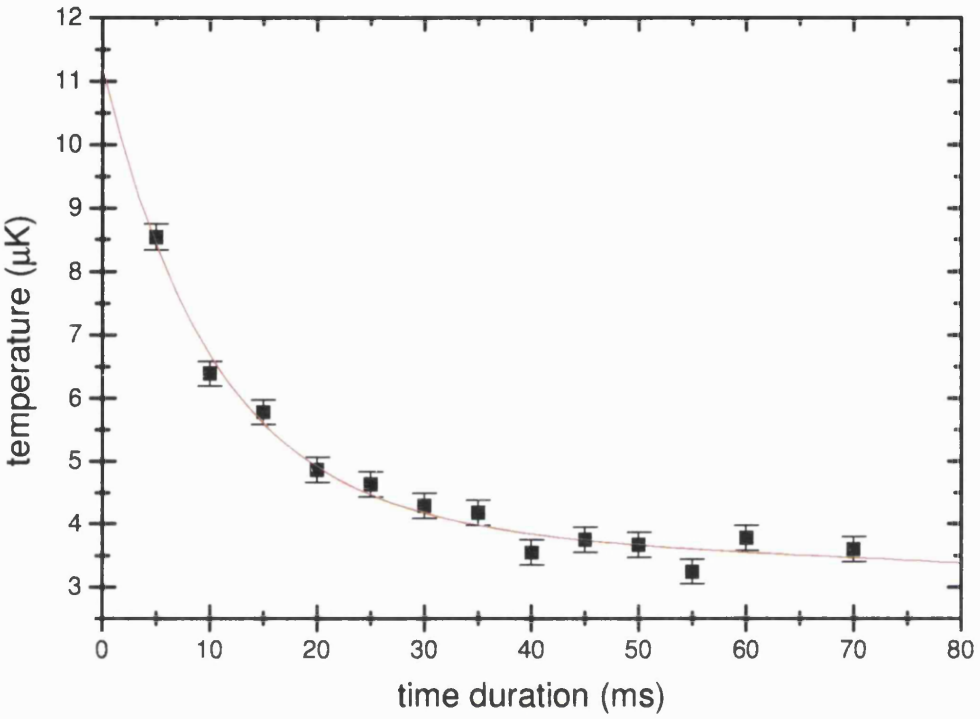

Figure 4.9: Temperature decay of far-detuned lattice versus time duration.

out faster. The temperature decays rapidly (consistent with the assumption that atoms escaping from states close to the top of the potential are responsible for the fast decay), and it reaches a steady value of $\simeq 3\mu$K. This steady value for the temperature is given by the balance between the loss of highly energetic atoms and the heating of atoms in lower lying states induced by scattering or noise, which becomes relevant at long times. At the same time it shows reduced loss rates for lower lying bands.

It is very difficult to isolate without ambiguity the different causes of loss. A major cause of loss of atoms is, in fact, linked to the non-uniform spatial profile of the FD beams over the lattice region. As a consequence, some of the atoms are never bound in the FD potential, while others are bound in a region of shallower

potential, which allows energetic atoms to be easily excited out of the lattice. The option of expanding the FD beam further to select an almost uniform section of the intensity profile was ruled out due to the fact that the available laser power was limited. A compression of the cloud, as suggested in [34], before loading the near-detuned lattice was attempted resulting in an increased loading of the far-detuned lattice, but significant losses were still detected.

4.3 Band population measurements

Several experiments were performed in order to further investigate the storage of atoms in the far-detuned optical lattice and to acquire an understanding of the band population distribution. Experiments were run that were aimed at the selection of the lower lying bands. Similar band selection techniques were used in [35], [36], and [37] for quantum state preparation or simply used as a diagnostic instrument. The typical sequence of a band selection experiment proceeds as follows. The atoms were firstly loaded in the far-detuned lattice with a laser intensity I_{max}. After a certain storage time the atoms in the higher lying vibrational levels were released by ramping down the laser intensity to a value I_{min} for which high energy atoms are not bound anymore. The intensity was typically ramped down to I_{min} in 500μs and the I_{min} value was kept constant for variable times. The laser light was then switched off by ramping the intensity to zero. It has to be pointed out here that due to a limitation of the experimental setup, it was only possible to ramp continuously the laser intensity down to 20% of the maximum intensity. This was due to the fact the the lattice beam was generated by the zero order beam of an acousto-optic modulator and even at maximum first order diffracted light, the intensity of the zero order was up to 20% of the maximum intensity. The light was completely disrupted by means of a mechanical shutter.

In figure 4.10 a sequence is shown for an initial storage time of 10 ms and

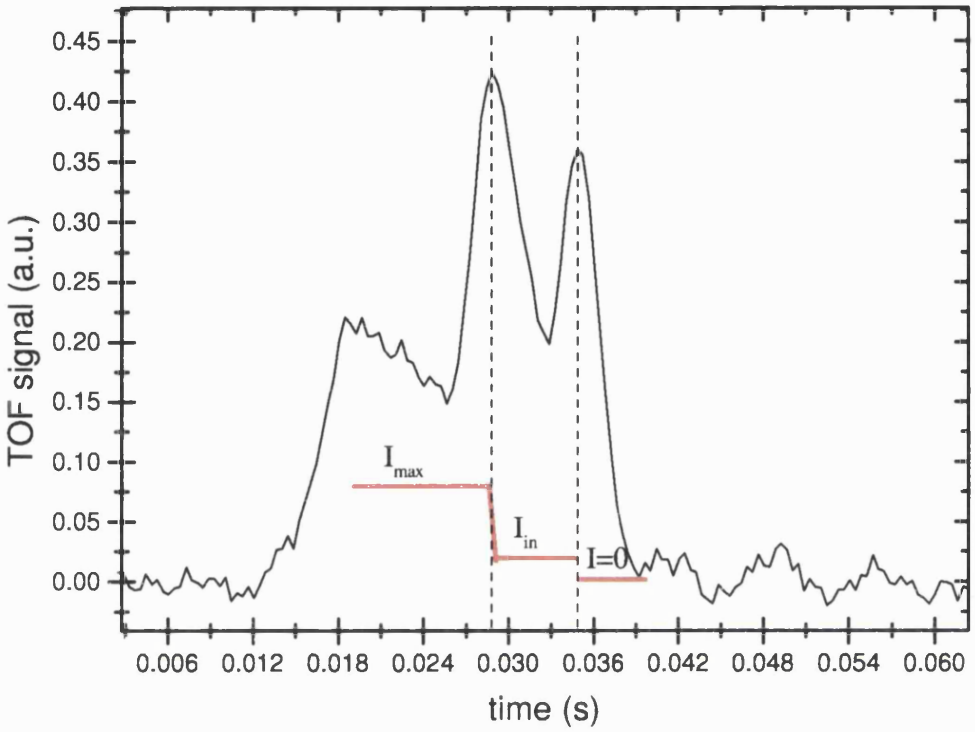

Figure 4.10: Selecting the lower bands for quantum state preparation.

$I_{min} = 0.2 \times I_{max}$ kept on for 5 ms before the light was completely switched off. The peaks corresponding to the higher and lower lying bands are very well separated, therefore it is possible to reconstruct the population of the different vibrational levels. In the case examined in figure 4.11, the starting potential had $U_{max} = 140E_R$ and the sample kinetic temperature was 5 μK. The calculated bands for these parameters are shown in figure 4.12. The first six bands correspond to bound states for the atoms, while the levels $n = 8$ and $n = 9$ show a significant curvature and broadening, which means that the corresponding wave-function is not localised. By reducing the laser intensity we see that the losses start to be significant for $I = 0.6I_{max}$, i.e. when the maximum light shift is reduced to $80E_R$

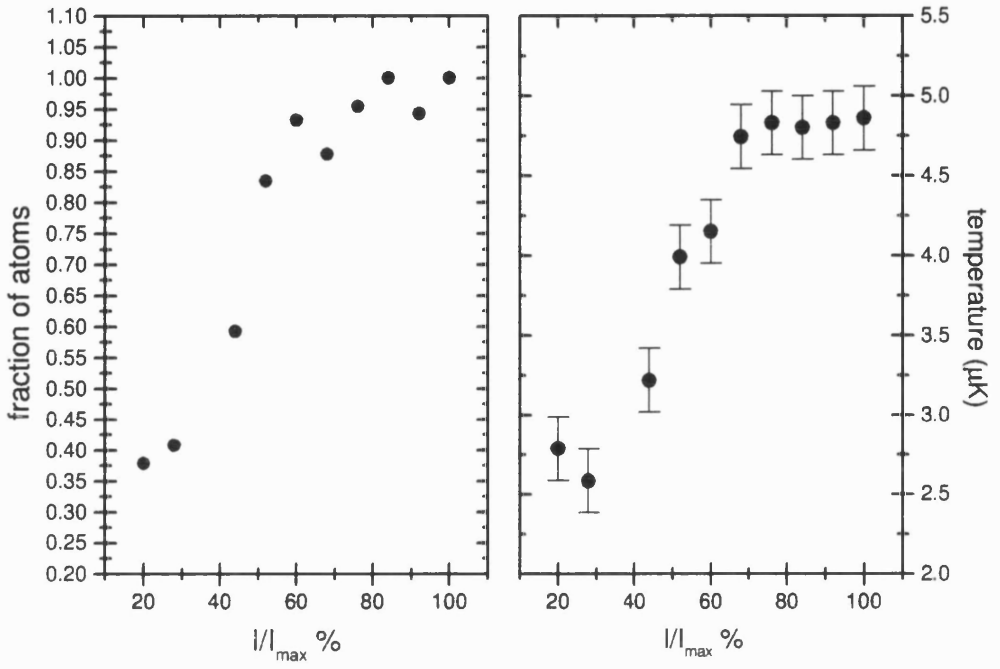

Figure 4.11: Measurement of population and temperature variation for selected bands.

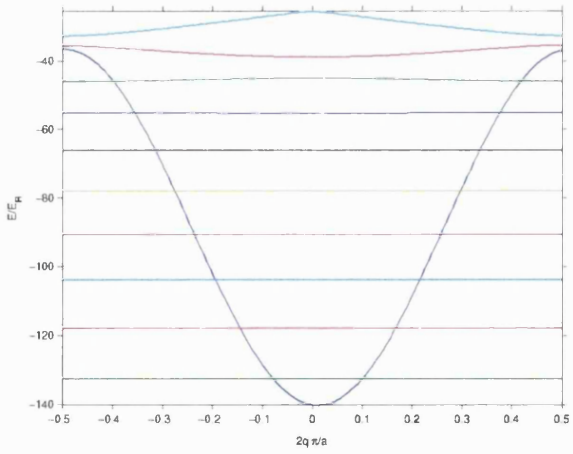

Figure 4.12: Results of band calculations for $U_{max} = 140E_R$. Superimposed on this plot, employing the same vertical scale, is a cut through the potential energy surface. The horizontal scale of this curve (black line) is arbitrary and is chosen so that one period of the potential fits into frame of the figure.

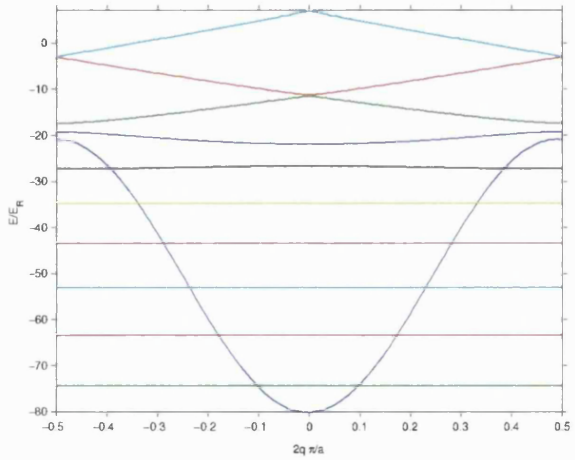

Figure 4.13: Results of band calculations for $U_{max} = 80E_R$. Superimposed on this plot, employing the same vertical scale, is a cut through the potential energy surface. The horizontal scale of this curve (black line) is arbitrary and is chosen so that one period of the potential fits into frame of the figure.

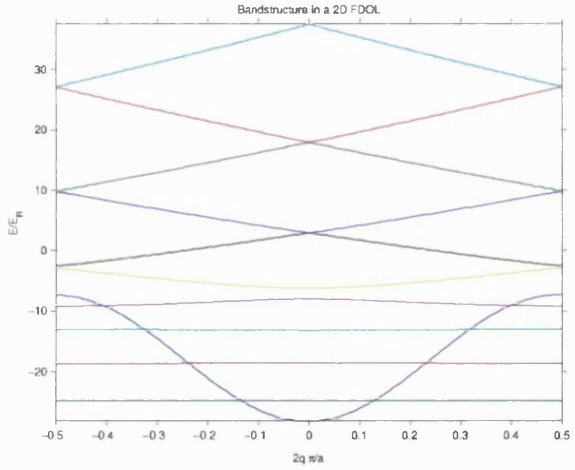

Figure 4.14: Results of band calculations for $U_{max} = 28E_R$.Superimposed on this plot, employing the same vertical scale, is a cut through the potential energy. The horizontal scale of this curve (black line) is arbitrary and is chosen so that one period of the potential fits into frame of the figure.

(see figure 4.13). The kinetic temperature starts dropping as well, due to the reduced momentum spread associated with lower lying bands. It was possible to control the intensity down to about $0.2 \times I_{max}$, which corresponds to $U_{max} = 28E_R$.

As shown in figure 4.14 and by analyzing the broadening of the bands, the three lower states correspond to bound states. Data plotted in figure 4.11 show that at $I = 0.2I_{max}$ the fraction of atoms that remained trapped in the reduced potential is $\simeq$ 37% of the initial population. This was found to be in good agreement with the calculated total population of the first three bands of a 1-D harmonic oscillator, when the starting temperature of 5 μK was assumed.

This was a preliminary study of band population measurements. To overcome the limitation imposed by the far-detuned lattice intensity control, the experiment has been now improved by introducing an electro-optic modulator, which is also used to finely control the intensity of the far-detuned lattice. This new set-up should allow us to investigate further the band population distribution and resolve even the lowest lying bands.

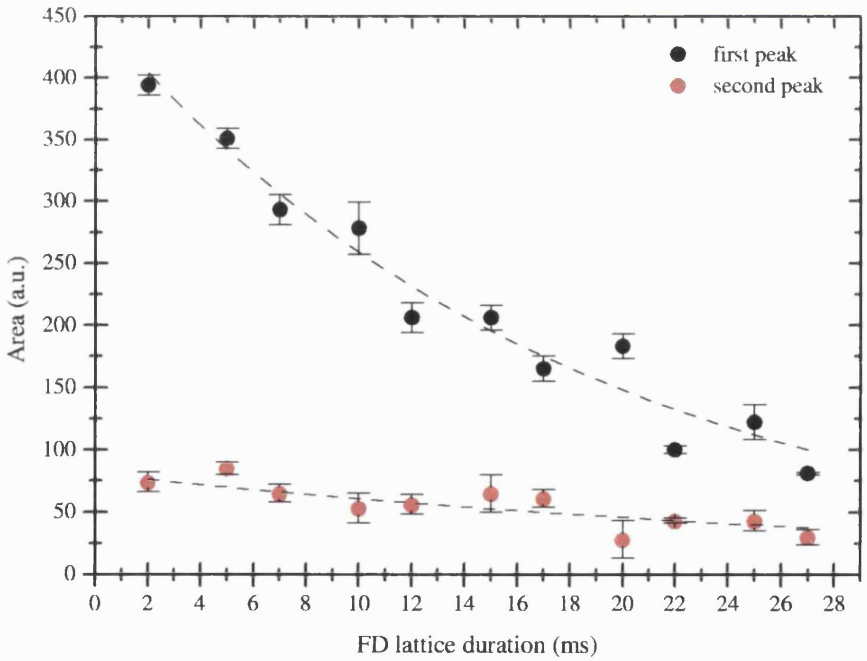

Figure 4.15: Band-dependent losses versus storage time.

In order to sustain the hypothesis that the losses of atoms, as reported in the previous section, are indeed band-dependent, a simple experiment was run. The sequence was identical to the one previously described for band populations resolution. The changes in the areas of the two peaks, see figure 4.10, were monitored, this time at varying the storage time at maximum intensity. The atoms were stored in the far-detuned lattice for variable times and then the populations of the higher lying and three lower lying bands were simultaneously measured. Therefore, if the losses are really band-dependent, it should be possible to see that the first peak's area, which counts the atoms populating higher lying bands, start decreasing at shorter storage time, or decreases more rapidly than the area of the second peak, which arises from lower energy atoms.

The variation of the areas of the two peaks versus the storage time at maximum intensity are shown in figure 4.15. To estimate and compare the characteristic decay times of the two sets of measurements, two exponential decays were fitted to the two sets of data, resulting in a characteristic decay time of $\simeq (15 \pm 4)$ ms for the first peak and of $\simeq (40 \pm 12)$ ms for the second one. These fits are not meant to prove an exponential behaviour of the decay of the population in different vibrational levels, neither do they constitute an accurate measurement of the decay times; they only constitute a way of defining and quantifying the two different decay rates. These lend further evidence for the band-dependence of the loss mechanisms.

The measurements and experiments reported in this section are not meant to constitute a detailed analysis of the problem. The limitations of the experimental setup, mainly the non-uniform potential depth of the far-detuned lattice, the low laser power available and the coarse control on the laser intensity would not allow a more accurate treatment. However it was important to study the loading efficiency and the losses mechanisms to understand the importance of improving

the experiment and the modifications that were required.

4.4 Conclusions

In this chapter I described the experimental setup and techniques used for loading atoms into a 2-D far-detuned optical lattice, by transferring them from a super-imposed near-detuned lattice. The efficiency of the transfer was studied and experiments revealed that a significant fraction of atoms was lost at the time of the loading, while more atoms were leaking out of the lattice at later times. Experiments aimed at measuring the populations and temperature of the different vibrational states were performed, which demonstrated the feasibility of resolving the different band populations and proved that the loss of atoms from the lattice is band-dependent. A study of the population's decay versus storage time led to the evaluation of two distinct decay times; it was also possible to attribute as main causes of loss the heating induced by spontaneous scattering for the long decay time and, as it will be extensively discussed in the next chapter, laser intensity fluctuations, that could be responsible for the short decay time. All the qualitative analysis presented in this chapter revealed the limitations of the experimental apparatus and suggested possible changes for its optimization.

CHAPTER 5

Parametric Excitation

The parametric excitation method is a useful tool for the investigation of the features of the far-detuned lattice and has been pursued both experimentally and theoretically in previous works [38], [39], [40], [41]. The excitation caused by resonant intensity fluctuations has been proposed as a major cause of heating in far-off resonant traps [40], [41]. In [38] the parametric excitation method was first used in order to characterize the lattice structure. In [42] parametric heating in harmonic potentials is studied both non-perturbatively and perturbatively. The former approach establishes an explicit connection between the classical and the quantum description. The latter gives an alternative insight into the problem and can be directly extended to take into account the anharmonicity, which becomes relevant for shallow traps. The perturbative model was also used in order to investigate the characteristics of the far-detuned lattice, i.e. the effective vibrational frequency, potential depth and anharmonicity.

In this chapter an overview of the results found in [42] will be presented. The implementation of a code based on the model presented in [42], used to simulate losses and heating in a parametrically excited lattice is described. The model is then compared with the experimental results, which are presented in section 5.3,

and the characteristic lattice features are evaluated. This model is particularly useful to understand the effects of anharmonicity of the potential and of the non-uniformity of the laser profile over the lattice region, which was found to affect our experiment. In the last section of this chapter, results from simulations run to evaluate the importance of noise-induced heating are reported. These represent only an estimate of the maximum heating rate, as, due to the high noise floor of the diagnostic electronics, the laser noise could not be measured accurately; they led to the reasonable conclusion that the heating rate due to stochastic intensity fluctuations should not be significant on the timescale of typical experiments.

5.1 Perturbative treatment of parametric excitations

I will outline the theoretical approach introduced in [40], [39],[42]. The non perturbative approach to parametric heating, discussed in [42], is only valid for quadratic potentials and cannot take into account anharmonicity effects. When the confining potential is shallow, however, anharmonicity effects become significant and a simple method that can take them into account is the high order perturbative approach to parametric heating presented in [42]. The purpose of the method is to study some high order perturbative effects due to a variation of the strength of the confining potential, while also taking into account the anharmonicity and inhomogeneities of the laser beam's profile.

Parametric excitation is obtained by applying a small modulation to the intensity of the lattice light. The Hamiltonian of the system can then be written as:

$$H = \frac{p^2}{2m} + V[1 + \epsilon(t)], \tag{5.1}$$

where the first term is the kinetic energy, the second term the potential energy and $\epsilon(t) = \frac{I(t)-I_0}{I_0}$ is the fractional modulation induced on the potential by varying

the light intensity;

$$V(\mathbf{x}) = -\frac{\mathbf{1}}{\mathbf{4}}\alpha\,|\mathbf{E_L}(\mathbf{x})|^{\mathbf{2}} \tag{5.2}$$

is then the effective potential, where α is the effective atomic polarizability and E_L is the radiation field amplitude.

Following the time-dependent perturbation theory, the unperturbed Hamiltonian is defined as:

$$H_0 = \frac{p^2}{2m} + V(x) \tag{5.3}$$

while the equation of motion of the state $|\Psi(t)\rangle$ is ruled by:

$$i\hbar\frac{d|\tilde{\Psi}(t)\rangle}{dt} = \epsilon(t)\tilde{V}(x,t)|\tilde{\Psi}(t)\rangle, \tag{5.4}$$

where

$$|\tilde{\Psi}(t)\rangle = e^{iH_0t/\hbar}|\Psi(t)\rangle. \tag{5.5}$$

The interaction operator is:

$$\tilde{V} = e^{iH_0t/\hbar}V(x)e^{-iH_0t/\hbar} \tag{5.6}$$

and the evolution operator is given by:

$$\tilde{U}(t) = 1 - \frac{i}{\hbar}\int_0^t \epsilon(t)\tilde{V}(x,t)\tilde{U}(t')dt'. \tag{5.7}$$

The transition probability between two states of the unperturbed Hamiltonian can be written, using equation 5.7 as:

$$\langle n|\tilde{U}(t)|m\rangle = \delta_{nm} - \frac{i}{\hbar}V_{nm}\int_0^t dt'\epsilon(t')e^{i\omega_{nm}t'} \tag{5.8}$$
$$-\frac{1}{\hbar^2}\sum_n V_{nk}V_{km}\int_0^t dt'\epsilon(t')e^{i\omega_{nk}t'}\int_0^{t'} dt''\epsilon(t'')e^{i\omega_{km}t''} + ...,$$

with $\omega_{nk} = (E_n - E_k)/\hbar$ and

$$V_{nk} = \langle n|V|k\rangle = E_n\delta_{n} - \langle n|\frac{p^2}{2m}|k\rangle. \tag{5.9}$$

If it is assumed that the changes in the wave-function induced by $\tilde{U}(t)$ are small in the interval (0,t), then it is possible to estimate the average rate of transitions from a state $|n\rangle$ to a state $|m\rangle$ in a time t:

$$R_{n\to m} = \frac{1}{t}|\langle n|\tilde{U}^{(n)}(t)|m\rangle|^2. \tag{5.10}$$

If the heating is induced by a modulation of the confining potential:

$$\epsilon(t) = \epsilon_0 \cos(\omega t) \tag{5.11}$$

then up to the second order in ϵ_0, the transition probability is given by:

$$\begin{aligned}\langle n|\tilde{U}^{(2)}(t)|m\rangle = \delta_{nm} + \frac{i}{2\hbar}\epsilon_0 t V_{nm}[\zeta((\omega_{nm}+\omega)t) + \zeta((\omega_{nm}-\omega)t)] \\ - \left(\frac{\epsilon_0}{2\hbar}\right)^2 t \sum_k V_{nk}V_{km}\Big[\frac{1}{i(\omega_{km}+\omega)}[\zeta((\omega_{nm}+2\omega)t) + \zeta(\omega_{nm}t) \\ -\zeta((\omega_{nk}+\omega)t) - \zeta((\omega_{nk}-\omega)t)] + \frac{1}{i(\omega_{km}-\omega)} \\ [\zeta((\omega_{nm}-2\omega)t) + \zeta(\omega_{nm}t) - \zeta((\omega_{nk}+\omega)t) - \zeta((\omega_{nk}-\omega)t)]\Big],\end{aligned} \tag{5.12}$$

where $\zeta(x) = e^{ix/2}\frac{\sin(x/2)}{x/2}$. It has to be again emphasized that this expression is only valid for small changes induced in the time t.

For a harmonic oscillator with frequency ω_0, the matrix elements V_{nm}, can be written as [42]:

$$V_{nk} = \frac{\hbar\omega_0}{4}[(2k+1)\delta_{nk} + \sqrt{n(n-1)}\delta_{n,k+2} + \sqrt{(n+1)(n+2)}\delta_{n,k-2}] \tag{5.13}$$

From an examination of the various terms in equation 5.12, it is possible to see that the following $V_{nk}V_{km}$ products are combined to give a non zero contribution for:

(i) $V_{n,n\pm2}V_{n\pm2,n\pm4}$ – the resonant terms appear in the combination $\zeta((4\omega_0 \pm 2\omega)t) - \zeta((2\omega_0 \pm \omega)t)$, so that such transitions are highly suppressed

(ii) $V_{nk}V_{kn}$ – the resonant terms appear for $\omega = 0, 2\omega_0$. For $\omega \sim 2\omega_0$ the amplitude of the transition is proportional to

$$\frac{\epsilon^2 t}{2\hbar\omega_0}\left[|V_{n,n+2}|^2\left(\frac{\zeta(0)-\zeta((\omega-2\omega_0)t)}{i(\omega-\omega_0)}\right)+|V_{n,n-2}|^2\left(\frac{\zeta(0)-\zeta((2\omega_0-\omega)t)}{i(\omega-\omega_0)}\right)\right]; \tag{5.14}$$

(iii) $V_{n,n\pm2}V_{n\pm2,n\pm2}$ and $V_{n,n}V_{n,n\pm2}$ – these transitions can be viewed as a combination of two virtual transitions $n \to m \to m$ or $n \to n \to m$. According to equation 5.12, the corresponding resonance frequency is the fractional frequency $\omega = |\omega_{nm}|/2 = \omega_0$. The transition probability for $\omega \sim \omega_0$ is then:

$$\begin{aligned}\left(\frac{\epsilon}{2\hbar}\right)^2\frac{t^2}{\omega_0^2}|V_{nm}|^2(V_{nn}-V_{mm})^2\frac{\sin^2(\omega-\omega_0)t/2}{(\omega-\omega_0)^2t^2/4} \\ \simeq \frac{\epsilon^4\omega_0^2t^2}{1024}(n-m)^2[n(n-1)\delta_{n,m+2} \\ +(n+1)(n+2)\delta_{n,m-2}]\frac{\sin^2(\omega-\omega_0)t/2}{(\omega-\omega_0)^2t^2/4}.\end{aligned} \tag{5.15}$$

In all the above cases, the non resonant terms $\zeta(\omega' t)$, with $\omega' \neq 0$, give rise to oscillations of the transition probability, which is consistent with the results found by the exact evaluation of the transition probability discussed in [42]. For long times, such that $t\omega' \gg 1$, then the resonant terms only give a significant contribution.[1] In that limit the transition rates $R_{n\to m}$ are constant.

The dominant transition probability of a fractional frequency resonance $\omega = 2\omega_0/n$, arises at n-th order perturbation theory. It can be viewed as an n-steps procedure consisting of n-steps virtual transitions, where $n-1$ of them do not change the state but one does change it. Thus it is expected that equation 5.15 describes approximately the transition probabilities $n \to n \pm 2$ when the source has a frequency $\omega = \omega_0$.

[1] keeping in mind the δ-function representation as $\delta(\omega) = \frac{2}{\pi}\lim_{t\to\infty}\frac{\sin^2(\omega t/2)}{t\omega^2}$

5.1.1 First order perturbation theory

As shown above, within the first order perturbation theory the additional varying potential induces transitions between states n and m with an average rate:

$$R_{n\to m} = \frac{1}{T}\left|\frac{-i}{\hbar}\int_0^T V_{nm}\epsilon(t)e^{(i\omega_{nm}t)}\right|^2 = \frac{\pi}{2\hbar^2}\left|V_{nm}\right|^2 S(\omega_{mn}), \tag{5.16}$$

where V_{nm} is the matrix element of the space part of the perturbation, defined in equation 5.13,

$$S(\omega) = \frac{2}{\pi}\int_0^T \cos(\omega\tau) < \epsilon(t)\epsilon(t+\tau) > d\tau \tag{5.17}$$

is the one-sided spectrum of the fractional intensity modulation and $< \epsilon(t)\epsilon(t+\tau) >$ is the correlation function for the fractional intensity fluctuations.

If the confining potential can be approximated by a harmonic well [2], the only terms which are non-zero for the transition rates are

$$R_{n\to n} = \frac{\pi\omega_0^2}{16}S(0)(2n+1)^2 \tag{5.18}$$

and

$$R_{n\to n\pm 2} = \frac{\pi\omega_0^2}{16}S(2\omega_0)(n+1\pm 1)(n\pm 1). \tag{5.19}$$

As shown in [40] and [41], from equations 5.18, 5.19 it is possible to deduce the exponential character of the heating rate and its dependence on $2\omega_0$, typical of the parametric nature of the excitation process. Assuming that the atoms are occupying the $|n\rangle$ state with probability $P(n,t)$ at time t, the average heating rate is given by the sum of the contributions of processes involving a change of vibrational level; therefore, according to equation 5.19:

$$\left\langle \dot{E} \right\rangle = \sum_n P(n)2\hbar\omega_0(R_{n\to n+2} - R_{n\to n-2}) = \frac{\pi}{2}\omega_0^2 S(2\omega_0)\left\langle E\right\rangle, \tag{5.20}$$

where the average energy $\langle E\rangle$ is

$$\langle E(t)\rangle = \sum_n P(n,t)(n+\frac{1}{2})\hbar\omega_0. \tag{5.21}$$

[2] Assuming that the anharmonicity effects are negligible

The heating rate is therefore proportional to the average energy itself and depends on the vibrational frequency of the lattice. From equation 5.20 it is possible to deduce the exponential behavior of time evolution of the average energy. By introducing the characteristic time t_e, the time to increase $\langle E \rangle$ by a factor of e, it follows that:

$$t_e = (\pi^2 \nu_0^2 S_\epsilon(2\omega_0))^{-1} \tag{5.22}$$

In the classical regime, parametric oscillators exhibit resonances not only at $2\omega_0$ but also at $2\omega_0/n$ with n any integer. Resonances corresponding to $n = 2$ have been observed for far-detuned optical lattices , as shown in [38], [43]. In order to reconstruct the processes which lead to $2\omega_0/n$ resonances it is necessary to appeal to the nth-order perturbation theory. Furthermore, some general features of the optical lattice are lost in the harmonic model: the energy-band structure and spread of transition energy are not taken into account in the previous model. In the following sections I will discuss a model, which is based on the results found in [42] and similarly to [39], attempts to account for higher order heating rates and the anharmonicity of the potential wells in our lattice. Our model was developed independently on the work done in [39] and their differences and similarities will be highlighted during the following sections.

5.1.2 Second order perturbation theory and anharmonicity

In section 5.1 the parametric excitation was studied in the harmonic approximation and according to first order perturbation theory. In [39] the model was extended to second order perturbation theory and the anharmonicity was introduced semi-empirically as a broadening of the vibrational levels involved in the transition.

The second order correction to the transition rate between states $|n\rangle$ and $|m\rangle$ is given by:

$$R^{(2)}_{n\to m} = \sum_k \left(\frac{-i}{\hbar}\right)^2 V_{nk} V_{km} \int_{t_0}^{t} e^{i\omega_{nk}t'} \epsilon(t') dt' \int_{t_0}^{t} e^{i\omega_{km}t''} dt''. \tag{5.23}$$

The transition process can be described as a two step procedure: a first step $|n\rangle \rightarrow |k\rangle$ and a second $|k\rangle \rightarrow |m\rangle$. In the previous section it was shown in equations 5.18, 5.19 that the only non-zero matrix elements for the space part of the perturbation are the terms involving transitions $|n\rangle \rightarrow |n\rangle$ or $|n\rangle \rightarrow |n \pm 2\rangle$. Then for a first step in which the final state is the same as the initial $|n\rangle \rightarrow |n\rangle$, followed by a second transition $|n\rangle \rightarrow |n \pm 2\rangle$, the net energy change is $2\hbar\omega_0$. Therefore, a resonance occurs when the total energy of the two excitation processes coincides with the net energy change, i.e for $\omega = \omega_0$. The probability $P(n)$ of finding an atom in the level n is then given by:

$$P(n,t) = P(n,t_0) + \sum_m R^{(1)}_{n\rightarrow m}(P(m,t_0) - P(n,t_0))(t-t_0) + \sum_m R^{(2)}_{n\rightarrow m}(P(m,t_0) - P(n,t_0))(t-t_0)^2, \quad (5.24)$$

which is valid in the limit $t \sim t_0$.

All these considerations can be extended to the anharmonic potential case. The difference is that the anharmonic transition matrix elements $T(n,m)$ are non-zero for a wider set of pairs n, m and the transition energies will have a broadened distribution. To form an idea of the frequency spread in an anharmonic potential, I refer to Table 2.1, where the energy spectrum obtained for a $U_{max} = 170E_R$ and $U_{max} = 250E_R$ as well as the bandwidth for the different levels are shown.

In order to estimate the inter-band transitions driven by parametric excitation a phenomenological broadening must be taken in account. The broadening arises not only from anharmonicity of the band structure but also from other sources, such as laser intensity and pointing fluctuations and, more important, intensity inhomogeneities along the lattice region. In fact, in section 4.2 it was shown that the laser profile is not homogeneous so that the trapped atoms experience different potential at different lattice sites. This leads to a large variation of the vibrational frequency of atoms at different lattice sites. Furthermore, each of the vibrational bands in a single potential well exhibit a finite width, which is negligible for

low lying levels but becomes significant for higher energy states. We can try to take in account for this spread of frequencies considering each level involved in the transition as a Gaussian density distribution of states, centered at ω_0 with a width σ_n representing the frequency spread. Broad spectral lines can be introduced in the model by defining, as suggested in [39], an effective spectral density $S_{eff}(\omega)$, obtained by the convolution of the two Gaussians associated to the levels involved and with the excitation source with spectral density given by 5.17:

$$S_{eff}(\omega) = S_0 \exp \frac{(\omega - \omega_{eff})^2}{2\sigma_{eff}}, \tag{5.25}$$

where $\sigma_{eff}^2 = \sigma_m^2 + \sigma_n^2 + \sigma_0^2$, with $\sigma_{m,n}$ the widths of the levels involved and σ_0 the width of the excitation source and ω_{eff} is $\omega_{mod} - (\omega_m - \omega_n)$. At the moment all the sources of broadening can be semi-empirically included in the model as constant level widths. A future very useful improvement of the code will be the introduction of an energy dependent level width and trying to adapt the model to the experimental data in order to find out the relation of the level broadening with the vibrational number.

5.2 Parametric Excitation Simulations

Following the guidelines of the two previous sections, a simple model was developed, in order to simulate the parametric excitation experiment.

An initial Boltzmann distribution of atoms in the vibrational levels of a one-dimensional harmonic oscillator is assumed. The use of a one-dimensional model is justified considering the vibrational motion independent in the x and y directions. The rate-equations for the populations of each level are written according to equations 5.18, 5.19. Instead of using the harmonic approximation as in [39], the full matrix elements V_{nm} were calculated and included in the code; in this way, for each level involved in the transition the corresponding calculated frequency

(see table 2.1) was introduced, thus improving the accuracy of the model. Nevertheless a S_{eff}, as defined in equation 5.25, was still used in order to consider other broadening effects. The effective width takes into account the linewidth of the levels involved and the broadening due the fluctuation of the spring constant caused by the modulation of the potential depth. In this way the transitions from one level to another were simulated, taking into account anharmonicity effects, the linewidth of the resonances and the broadening caused by the modulation. Effects of other broadening sources, such as inhomogeneities of the potential, will be taken into account as a broadening in the transition linewidth.

Once the excitation processes have been considered, the loss of atoms excited out of the potential have to be simulated. It was further assumed that atoms excited to high-energy levels at the top of the potential well with width bigger than E_R (see table 2.1) are unbound and therefore lost. Evaluating the excitation and decay rates as well as the loss mechanisms, the population distribution over vibrational levels is modelled. The mean vibrational energy is then calculated as the population-weighted average of the vibrational energy of each level. The energy increase with time, for a fixed modulation frequency of $\simeq 2\omega_0$, was shown to be non-exponential; a fast energy growth at short times is followed by saturation at longer times. This can be explained by linking the energy increase at short times to atoms from the lower lying levels being excited to higher lying ones, whilst, at longer times, when the higher lying levels are mostly populated, the modulation source is no longer resonant with the excitation process, thus reducing the number of atoms excited per unit time.

In figure 5.1 an example of the results of the parametric excitation simulation is shown. The fraction of trapped atoms is plotted versus the excitation duration at different excitation frequencies. In this simulation the potential depth is considered uniform over the lattice region and equal to $200E_R$, which correspond to $\omega_0 = 36$

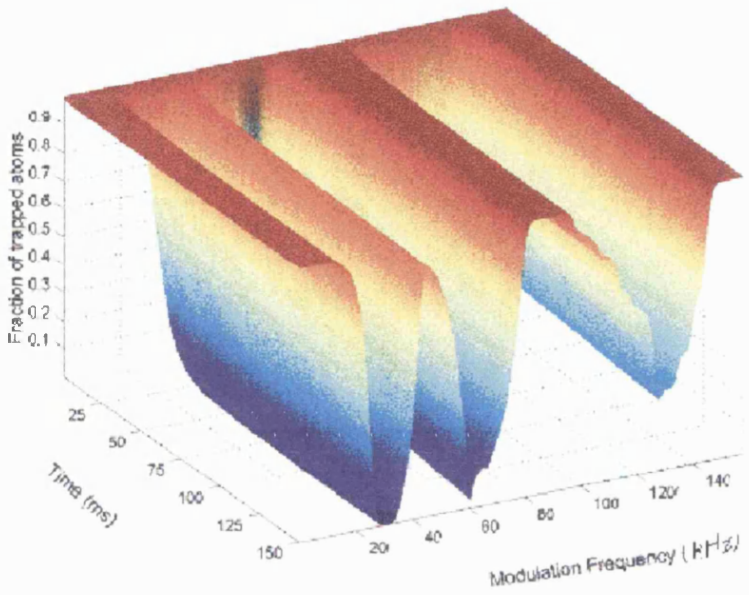

Figure 5.1: Simulation of parametrically induced losses versus modulation frequency and time for: $U_{max} = 200E_R$, $m_F = -4$, $T_{in} = 3\mu$K, $\epsilon_0 = 0.1$, $\sigma_0 = 1.5E_R$. The first resonance can be seen at 36 kHz, which corresponds to the characteristic vibrational frequency.

kHz and the initial kinetic temperature of the sample is assumed equal to 3μK. The plot shows several features corresponding to the main $2\omega_0$ resonance and higher order resonances. It has to be pointed out that the main resonances occur at a frequency slightly smaller than the vibrational frequency of the lower lying levels. This shows that a significant fraction of atoms in the potential wells would have a different characteristic vibrational frequency from the lowest lying ones, due to the anharmonicity. So by estimating the shift of the resonance frequency it is possible to give an estimate of the anharmonicity of the potential or of the inhomogeneity of the well depth.

In figure 5.2 the corresponding kinetic energy is plotted, which shows that it is possible to induce heating and cooling of the sample by parametrical excitation

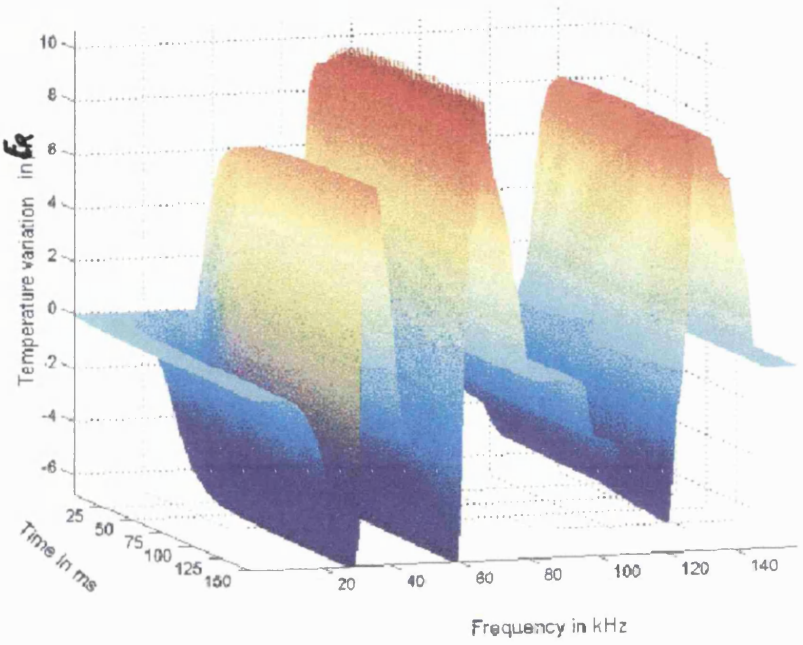

Figure 5.2: Simulation of parametrically induced temperature variation versus modulation frequency and time for: $U_{max} = 200E_R$, $m_F = -4$, $T_{in} = 3\mu$K, $\epsilon_0 = 0.1$, $\sigma_0 = 1.5E_R$.

of the vibrational modes, depending on the chosen excitation frequency. At a frequency for which the higher lying states are mostly excited, a parametric excitation sequence would result in loss of high energetic atoms, therefore in a net cooling of the remaining trapped sample. When the lower lying energy levels are stimulated, the excitation would result in an increased population of the higher lying ones, thus in a net heating of the atomic sample.

In the next two sections I will discuss how the model was used in order to simulate the parametric excitation and the noise induced heating. The model's contribution towards our understanding of the effect of anharmonicity, Zeeman population distribution and non-uniform laser intensity on the broadening of resonances is detailed. It will also be shown that the noise induced parametric excitation effect produces significant heating only at times much longer than the

typical duration of the experiment.

5.3 Parametric Excitation Measurements

A sample of atoms was prepared in the far-off resonance lattice with a detuning of $\Delta = (-2000 \pm 100)\Gamma$ and a single beam intensity of $I_{1beam} = (400 \pm 50)$ mW/cm^2. The potential induced on the trapped atoms therefore had a maximum light shift of $U_{max} = 170E_R$, corresponding to $\omega_{vib} = 35$ kHz. A modulation of 10% was then

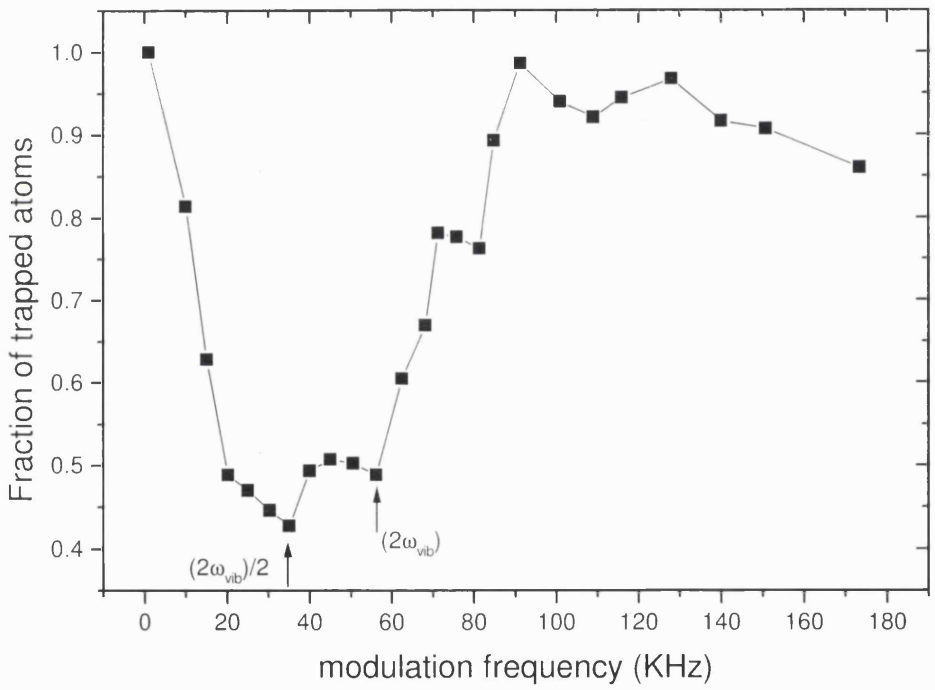

Figure 5.3: Experimental spectrum of the losses induced by parametrically exciting the lattice vibrational modes. The fraction of trapped atoms remaining in the lattice after the parametric excitation is plotted versus the excitation frequency.

introduced in the lattice potential depth (through an acousto-optic modulator used to control the laser intensity), which was left to parametrically excite the vibrational modes for 25 ms. At the end of the excitation time, the atoms were

released from the far-detuned lattice and let free to fall through the time-of-flight probe beam. In this way it was possible to estimate the number of atoms still left trapped at the end of the modulation, as well as the mean kinetic energy of the sample of atoms. Measurements were taken at various excitation frequencies.

In figure 5.3 the measured fraction of atoms left in the lattice is plotted versus the modulation frequency. According to section 5.1 a main resonance in the losses of atoms was expected at twice the vibrational frequency, and a secondary resonance at ω_{vib}. The data in figure 5.3 show a broad band for losses, with a width comparable to the resonance frequency itself.

In figure 5.3 two resonances seem to be resolved, despite the evident broadening, for $\omega_{mod} = 35$ kHz and 58 kHz. These resonances do not agree with the predicted resonances within the harmonic approximation, but are in good agreement with the prediction of the anharmonic model. Invoking anharmonicity effects it is also possible to explain the fact that resonances occur at frequencies slightly different from the expected harmonic vibrational frequency and, partially, the observed broadening. The major causes of broadening, though, were found to be due to inhomogeneities in the potential depth experienced by the atoms. This is in part caused by the inhomogeneous spatial intensity profile of the FDL beams, as discussed in section 4.2. Furthermore, with the use of Stern-Gerlach experiments (see chapter 6), it was also found that the atoms also populated several Zeeman states. Potentials associated with different Zeeman states have different depth and therefore the trapped atoms oscillate at different frequencies, depending on their m_F number. It was found that the Zeeman state population distribution plays a major role in the broadening of the resonances. The parametric excitation was modelled for different Zeeman-state potentials and the weighted average was then performed, after the populations of different Zeeman-states had been estimated with a Stern-Gerlach experiment.

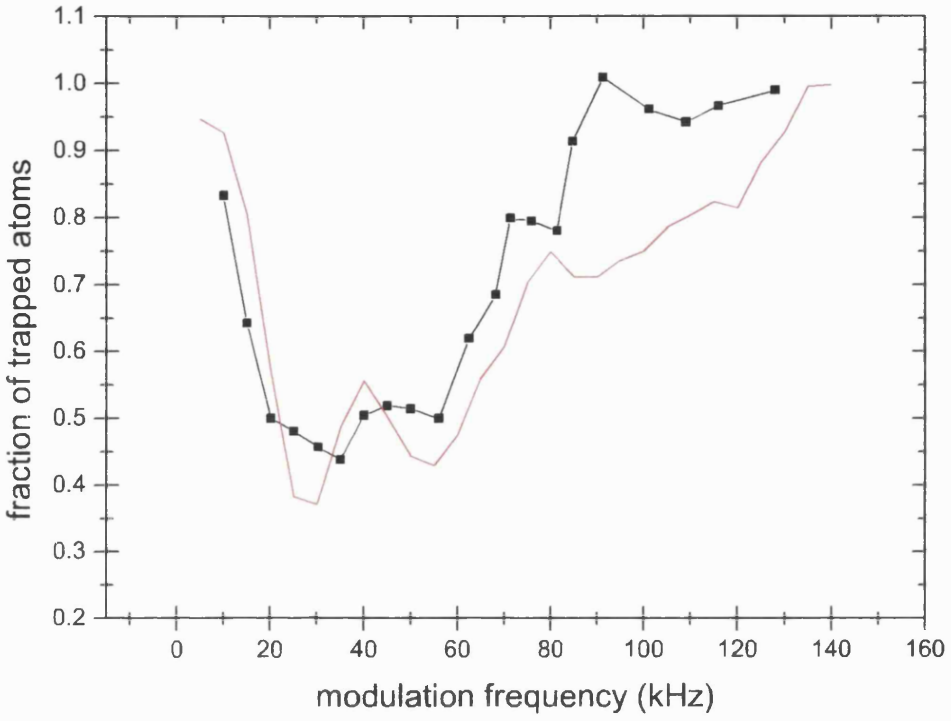

Figure 5.4: Comparison between experimental and theory data for population losses. The data plotted in black represent the measured number of atoms that remain in the lattice after a parametric excitation of the sample at different frequencies for 25 ms. The red line is the result of simulations.

In figure 5.4 the experimental data are plotted and compared with the results from the model. The model is in good qualitative agreement with the experimental data, allowing also the estimation of an effective vibrational frequency and therefore the maximum potential depth. The principal resonance of the trap seems to occur at $1.66\,\omega_0$, rather than $2\omega_0$. This follows from the fact that atoms in the lowest levels are partly excited to higher lying levels but are not lost (as would happen for a harmonic potential), while the most energetic atoms, which have a smaller excitation energy due to anharmonicity and are therefore more resonant

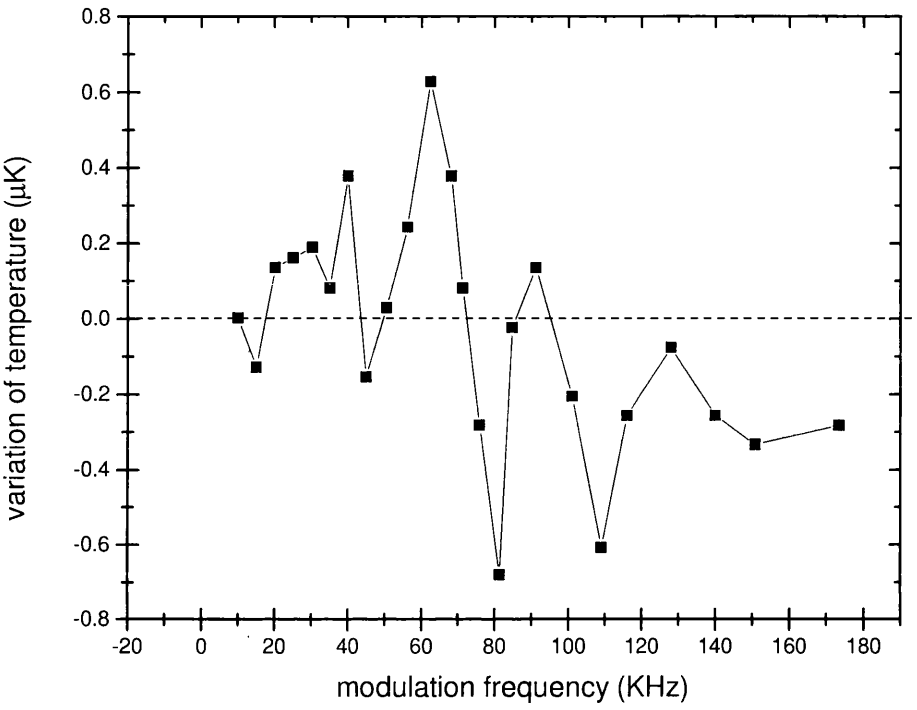

Figure 5.5: Experimental spectrum of the change in kinetic temperature induced by parametrically exciting the lattice vibrational modes at different frequencies for 25 ms.

with a lower excitation frequency, are immediately excited out of the lattice. This explains why the predicted main resonance at $2\omega_0$ actually occurs shifted to the low frequency side. The asymmetry of the resonances is also well reproduced by the model and reinforces the role of anharmonicity in the loss of atoms. Higher harmonic resonances are also predicted by the model, leading to the broad feature seen in figure 5.4, at $\simeq 3\omega_0$, not in very good agreement with the data, where this resonance is shown to be almost suppressed.

The mean kinetic energy of the sample was also measured and the variation in temperature is plotted versus the excitation frequency in figure 5.5. It is shown

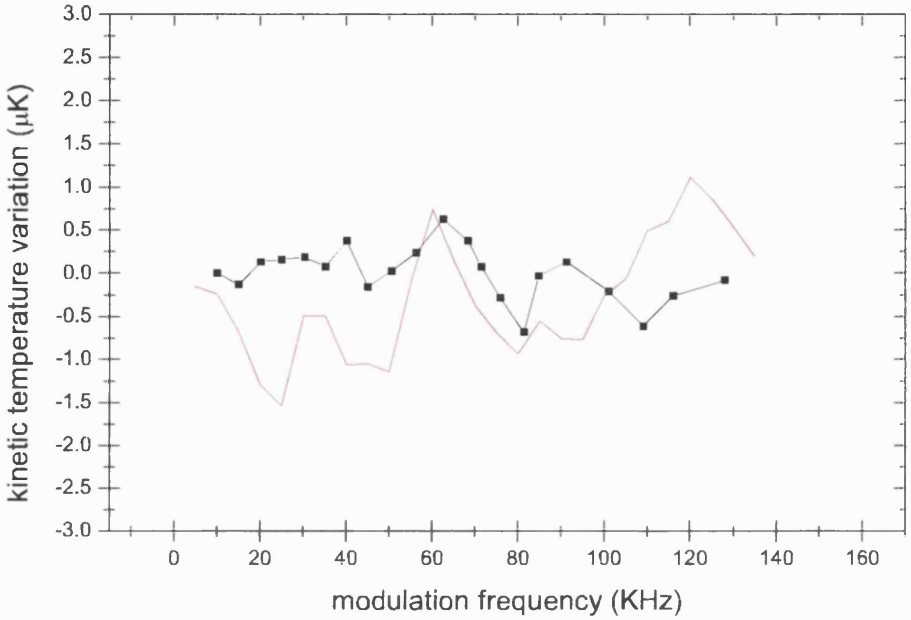

Figure 5.6: Comparison between experimental and theory data for kinetic temperature variations. The data plotted in black represent the experimental result of temperature measurements for the atoms left in the lattice after a parametric excitation experiment at different driving frequencies for 25 ms. The red line represents result of simulation.

there that both cooling and heating of the sample can be achieved depending on the excitation frequency: energy selective excitation processes can result in either cooling or heating, depending on whether lower or higher lying states are mostly excited. If the potential was homogeneous, it would be straightforward to deduce that at lower frequencies atoms in higher lying vibrational states are excited and expelled from the trap, thus resulting in a cooling of the sample. At higher frequencies, on the other hand, transitions involving lower lying states are mostly brought into resonance, thus heating the atoms. These results are in agreement with [44], where the exploitation of anharmonicity in shallow traps through parametric excitation processes was proposed as a method to boost evaporative

cooling. The situation presented in figure 5.5 shows definite regions of net cooling or heating, but the competition between the two phenomena cannot be simply attributed to different vibrational levels of the same potential; different potential depths and consequent spread in vibrational frequencies should also be taken in account. This cannot be simulated well with the present model. The model also does not take in account any other source of heating apart from the one introduced by the parametric excitation, thus only partially representing the true situation. Our model is not expected to fully reproduce the features of figure 5.5; it serves only to show that, due to inhomogeneities and anharmonicity, there are frequency ranges for which the net effect of parametric excitation is a cooling of the sample (higher lying modes are mostly excited) and regions where the heating dominates (lower lying modes are mostly excited). The predicted order of magnitude of such temperature variations was also shown to be consistent with the measured one, as it is shown in figure 5.6.

5.4 Noise-induced heating rates

In the previous sections it was shown that a modulation of the potential depth could selectively excite atoms in different vibrational bands out of the lattice. This would result in the remaining sample being heated or cooled. A code was developed which can simulate the losses of atoms excited out of the well and the net kinetic temperature of the sample of atoms which remain trapped. The anharmonicity of the potential depth played a basic role in the possibility of selectively exciting atoms in different bands by simply choosing an excitation frequency. If there was no anharmonicity or if the excitation source was composed by a broad band of frequency, then all the vibrational bands could be excited simultaneously. Laser intensity noise can cause atom heating, while losses linked to heating can limit the maximum storage time. Far-off-resonance optical lattices can be very sensitive to

intensity fluctuations and beam pointing variation [40]. An attempt was made to estimate of the upper limit to the heating rate induced by power fluctuations of the laser source. A measure of the noise spectrum of the laser was not possible, as the noise floor of the detection system electronics was above the noise level of the laser. An estimate of the noise-induced heating was therefore determined assuming a laser noise as high as the electronics noise, this constituting an upper limit for the power fluctuation induced heating. Therefore, by assuming a fractional variation with rms of $\epsilon_0 = 0.001$ at 410 mW total laser output power, the real noise level has certainly been overestimated. In case of noise-induced parametric excitation we have stocastic fluctuations of the laser power, instead of sinusoidal modulation. In this case we expect the energy to increase exponentially with time , as explained in [45] and not to saturate, as a broadband fluctuation would simultaneously excite the atoms in all the vibrational levels.

An estimate of the characteristic time of the heating process due to stocastic fluctuations driving the center of mass motion can be reached by using equation 5.22: for $\nu_0 = 35$ kHz typically and $S_\epsilon(2\nu_0) = 1 \times 10^{-6}$ Hz^{-1} a characteristic time of 80 ms was found. This is indeed a significant cause of heating, but only at times longer than the typical duration of a far-detuned lattice phase (typically 10 ms or less). Considering the long characteristic time and the fact that the laser noise is overestimated, the noise induced parametric excitation is not expected to play a significant role in our experiment for atoms in lower lying vibrational states. However atoms initially in highly energetic vibrational levels may be easily excited out of the lattice even at short time, due to intensity noise, as discussed in chapter 4. Thus in conclusion, we do not expect the noise-induce heating to significantly affect and limit the sideband-Raman cooling experiment. However intensity fluctuations of the laser are probably responsible for the reduced lifetime of the far-detuned lattice and the band-dependent losses, as high energetic atoms

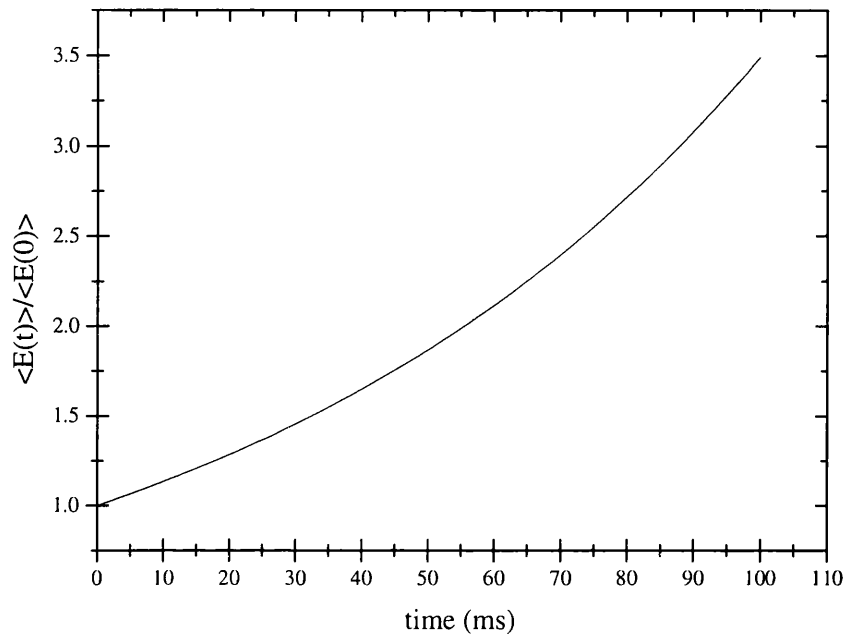

Figure 5.7: Mean energy growth due to intensity noise in the far-detuned lattice beam

in the lattice require minimal heating to be excited out of the well, as discussed in chapter 4.

5.5 Conclusions

A model of atom losses in an optical lattice induced by parametrically modulating the potential depth was developed, based on the theory presented in [42]. Experiments were run to monitor the escape of atoms from the lattice, when the laser beam was intensity-modulated. A comparison of the experiments with the model lent us insight into the band structure and the degree of anharmonicity of the potential. The temperature variation was also monitored and it was found that by parametrically modulating the lattice depth at a suitable frequency, it

was possible to selectively excite out of the lattice the most energetic atoms, thus cooling the remaining trapped sample. The clear effect of the non-uniformity of the potential depth along the trapping region was also demonstrated, which was due to the restricted dimensions of the far-detuned laser beams. An analysis of noise-induced heating suggested that intensity fluctuations may be partly responsible for the band-dependent losses of the far-detuned lattice, studied in chapter 4. However, the noise-induced heating is not expected to affect significantly the sideband-Raman cooling experiments (see chapter 7).

CHAPTER 6

Stern-Gerlach Analysis of Zeeman-state Populations

In the absence of static external magnetic fields, the atoms are distributed equally between the σ^+ and σ^- wells in the lattice. By adding a static magnetic field along the direction orthogonal to the lattice plane, the Zeeman levels are differently shifted, according to their m_F number. It is therefore possible to increase the population in the wells corresponding to the lowest energy shifted sub-lattice. As discussed in chapter 2, the sideband-Raman cooling scheme that we used in this work exploits coherences induced between the vibrational states of the potentials associated with the $|m_F = -4\rangle$ and $|m_F = -3\rangle$ states. A σ^--polarized pumping beam populates the stretched state in which the cooling is efficient. By spin-polarizing the near-detuned lattice it is possible to increase the initial population of the $|m_F = -4\rangle$ state in the far-detuned lattice, thus reducing the necessary interaction with the pumping beam. This would improve the cooling efficiency by reducing the heating rate due to photon-scattering.

In this chapter I will describe the Stern-Gerlach experiments that were implemented in order to perform a Zeeman analysis of the sample of atoms in the

lattice and an investigation of spin-polarization of the lattice. These experiments exploited the state-dependent magnetic dipole force induced by a magnetic field gradient, which was used to separate the time of flight signals of the individual magnetic sublevels. An optical lattice of the type described in chapter 3, in the configuration shown in figure 1.8B, presents, in fact, a geometry which associates with each lattice site a σ^+ or σ^- light polarization. The atoms are distributed over different lattice sites, each capable of trapping in different m_F states. When the atoms are released from the lattice they present a magnetic moment along the axis orthogonal to the lattice plane. The interaction of the atomic magnetic moment with a non-uniform magnetic field is exploited to accelerate the atoms differently according to their m_F state; hence the time-of-flight (TOF) signals for different Zeeman states can be time-separated. This method allows a measurement of the relative populations of the Zeeman states as well as the different temperatures associated with different lattice sites. This technique was used in [12] to prove the efficiency of local Sisyphus cooling in lattices for atoms with a large F. The interaction between the atomic magnetic moment and magnetic field gradients has been used extensively to tailor atomic beams. Several experiments on magnetic atom optical components, such as mirrors or refractive systems [46], [47], exploited the state-dependent magnetic dipole force induced with a varying magnetic field. More recently Stern-Gerlach experiments on caesium atoms were used to demonstrate a method to measure the quantum state of an atom with an arbitrarily large angular momentum [19].

The following sections will give a brief summary of the interaction of a magnetic moment with a magnetic field and of the analytical model that was used to simulate the Stern-Gerlach experiment. The experimental set-up and results are then shown for atoms released from the lattice and also for a spin-polarized ([48]) and an optically σ-pumped sample. The final section of this chapter discusses

the magnetization induced by means of a constant magnetic field, parallel to the lattice axis, and the consistency of the experimental data with the concept of a spin temperature; the results are in agreement with previous studies presented in [48], [12].

6.1 Atoms interacting with a magnetic field

The magnetic moment of an atom with angular momentum F is given by:

$$\boldsymbol{\mu} = \gamma \mathbf{F} = -g\frac{\mu_B}{\hbar}\mathbf{F}, \tag{6.1}$$

where γ is the gyromagnetic ratio, g is the Landé factor for the $|F, m_F\rangle$ state and μ_B is the Bohr magneton.

If a magnetic field $\mathbf{B}$ is introduced the magnetic moment interacts with it and the interaction potential becomes:

$$W = -\boldsymbol{\mu} \cdot \mathbf{B}. \tag{6.2}$$

The force interacting with the atom can be expressed as the gradient of the potential, that is equal to:

$$\mathbf{F} = -\nabla W = (\boldsymbol{\mu} \cdot \frac{\partial \mathbf{B}}{\partial x})\mathrm{i} + (\boldsymbol{\mu} \cdot \frac{\partial \mathbf{B}}{\partial y})\mathrm{j} + (\boldsymbol{\mu} \cdot \frac{\partial \mathbf{B}}{\partial z})\mathrm{k}, \tag{6.3}$$

where $(\mathbf{i}, \mathbf{j}, \mathbf{k})$ is the basis of the cartesian axes. If the magnetic field is uniform the magnetic moment precesses around the direction of $\mathbf{B}$ at a frequency (Larmor frequency) which is directly proportional to the magnitude of the magnetic field

$$\omega_L = |\gamma||\mathbf{B}|; \tag{6.4}$$

the net force over a Larmor period $T_L = 2\pi/\omega_L$ is zero. This means that the projection of the magnetic moment along the direction of the magnetic field remains constant. If the magnetic field $\mathbf{B}$ is inhomogeneous, from equations 6.2, 6.3 it can

be deduced that the net force is no longer zero and that it is proportional to the magnitude of the magnetic moment.

In a quantum description of an atom placed in a spatially uniform, constant magnetic field directed along the z-axis, $\mathbf{B} = B_z\mathbf{k}$, the system has stationary states which are eigenstates of $\mathbf{F}^2$ and F_Z with energies [49]:

$$E_m = \mu_B g m_F B_z. \tag{6.5}$$

The time evolution of one of the stationary states

$$|\Psi_m(t)\rangle = \sum_m c_m(t)|\Psi_m\rangle \tag{6.6}$$

is shown to be [49]:

$$|\Psi_m(t)\rangle = A\exp(-iE_m t/\hbar)|\Psi_m\rangle = A\exp(-i\omega_L m t)|\Psi_m\rangle. \tag{6.7}$$

From equations 6.6 and 6.7 it follows that the coefficients c_m can be expressed as

$$c_m(t) = \exp(-im\omega_L t)c_m \tag{6.8}$$

The populations of the stationary $|\Psi_m\rangle$ states $\pi_m = |c_m(t)|^2$ are therefore time-independent: the populations along the direction of the magnetic field, which we chose as the quantization axis, remain invariant.

The change in $\mathbf{B}$ during a small time interval can be decomposed to parallel and transverse components with respect to z. Any change in B_z has the sole effect of changing the Larmor frequency. A variation in the transverse direction of $B_\perp$ has the effect of introducing couplings with other Zeeman substates, [49]. The populations π_m are no longer constant in time, unless the variation in the transverse field over a Larmor period is much smaller than $|\mathbf{B}|$. This requires:

$$B \gg \frac{dB_\perp}{dt}\frac{2\pi}{\omega_L}. \tag{6.9}$$

In the case where ω_L is much bigger than the rate of change of the magnetic field, the internal and external degree of freedom decouple and the angular momentum

can adiabatically follow the variation of the magnetic field, while maintaining the component of magnetic moment along the initial direction of **B**. This means that the projection of the magnetic moment along **B** is constant over a Larmor period, so time averaged $\langle\mu\rangle$ has only a constant component along **B**. From equation 6.3 and the previous condition follows that:

$$\mathbf{F} = \langle\mu\rangle\nabla|\mathbf{B}(r)|, \tag{6.10}$$

i.e. the force depends only on the magnetic field strength.

6.2 Stern-Gerlach simulations

An analytical model was developed to simulate the different arrival times of atoms in distinguished m_F levels, when they are in the presence of a magnetic field gradient.

It was assumed that the condition of equation 6.9 is fulfilled, so that the internal and external degree of freedom of the atoms decouple and the angular momentum can adiabatically follow the slow changes of the magnetic field. In this case the force acting on an atom depends on the time averaged magnetic moment (which is constant) and the gradient of the magnetic field strength, from equation 6.10. The model is then used to calculate the acceleration of the atoms along the vertical axis, which leads to nine separate clouds corresponding to different atomic m_F states. By modelling the different trajectories along the vertical axis, it was possible to estimate the different arrival times of the nine clouds of atoms at the location of the TOF probe beam, situated 6 cm below the initial cloud position. A typical sequence of the experiment was then simulated with the code, in order to calculate the parameters which optimize the resolution of the nine peaks.

A cloud of cold caesium atoms is released and left free to fall under gravity for a variable time. After some time the magnetic field gradient is switched on and

left to interact with the atoms also for various durations. It was possible to vary both time durations as well as the magnetic field gradient to simulate the TOF signal produced by the falling clouds and to elect the right parameters in order to optimize the resolution.

It was realised that it is very important not to let the atoms pass the region of zero magnetic field (i.e. the middle point in the coils axis), in order to avoid a change in the orientation of the spins[1] and an inversion of the acceleration for individual m_F states, which would result in decreasing separation among the peaks. Therefore it is important to let the atoms fall freely until they are distant enough from the zero field point, that even during the subsequent acceleration none of the nine clouds passes again through that point. Assuming that there is no heating overall in the Stern-Gerlach measurement process (i.e. no increase in the mean velocity of the atoms), the duration of the free-fall has to be set depending on the duration of the interaction with the magnetic field gradient. This latter time scale has to be set in order to achieve the maximum resolution. Both durations are conditioned by the distance of the time-of-flight beam from the cloud. By running the code it was found that the best resolution was achieved when the atoms were let to fall freely for 30 ms. Following this, a magnetic field gradient of 40 G/cm was introduced for 25 ms. The result of the simulation for these parameters is shown in figure 6.1, where all m_F levels are equally populated. The code does not include a fitting routine to the experimental data, but it was, however, possible to vary the population of the magnetic levels in order to match the predicted curve to the measured Stern-Gerlach spectrum. In figure 6.2 a simulation of the Stern-Gerlach experiment after optical pumping the sample with σ light is shown, which showed that as much as 40% of the atoms are in the $m_F = -4$ state. The model was therefore used to estimate the optimal parameters needed in order to

[1] this condition is experimentally guaranteed by the on-axis constant magnetic field, which keeps the alignment of the magnetic moment

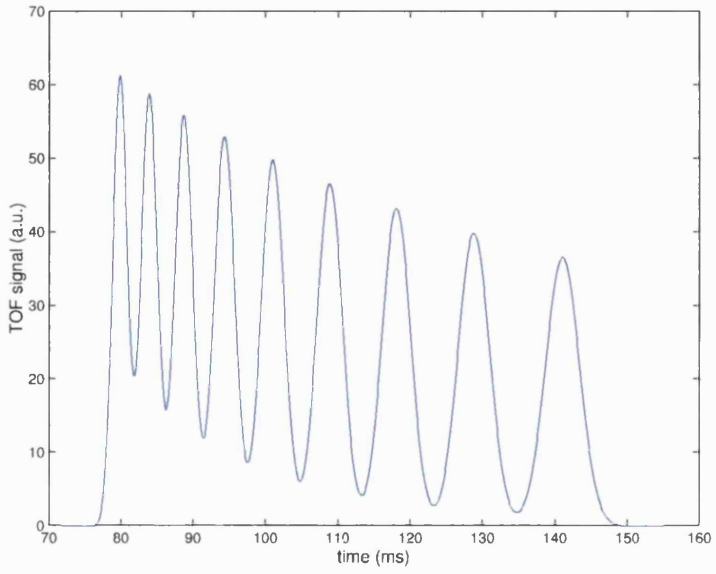

Figure 6.1: Simulated TOF spectrum for a a Stern-Gerlach experiment, for $t_{free-fall} = 25ms, t_{drop} = 30ms, G = 40G/cm$ and starting temperature $T = 4\mu$K.

perform the Stern-Gerlach experiment as well as to estimate the populations of the magnetic sub-levels from some experimental spectra.

6.3 Stern-Gerlach experiments

The Stern-Gerlach analysis allowed us to measure the populations of the different m_F states and also to distinguish the kinetic temperature in the two sublattices corresponding to trapping at σ^+ and σ^- circular polarized light locations. This was especially crucial in monitoring the transfer from the near-detuned to the far-detuned lattice and in inspecting the efficiency of the Raman cooling.

The basic idea is to use the time-of-flight (TOF) detection scheme described in chapter 3, to separate in time the detection of atoms in different m_F states. When the atoms are falling, following their release from the lattice, the introduction of a magnetic field gradient has the effect of generating a state dependent force which is proportional to the magnetic quantum number m_F of the atom [49]. This

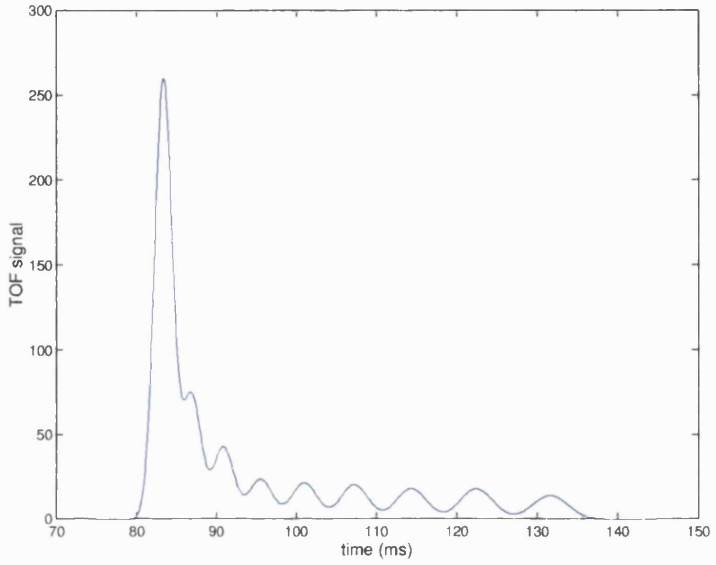

Figure 6.2: Simulated TOF spectrum for a a Stern-Gerlach experiment, for $t_{free-fall} = 30$ ms, $t_{drop} = 25$ ms, $G = 40$ G/cm and starting temperature $T = 4\mu$K and $\Pi_{-4} = 40\%$.

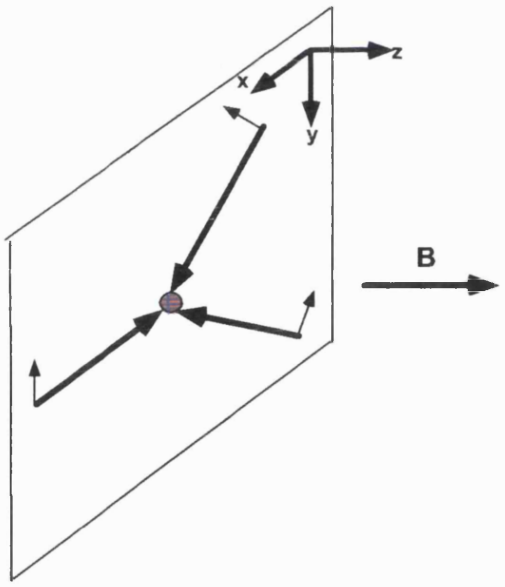

Figure 6.3: Representation of the lattice plane and quantization axis for the $lin - \theta - lin$ 2-D lattice.

force leads to different arrival times at the TOF beam location, for each magnetic sub-level atomic distribution.

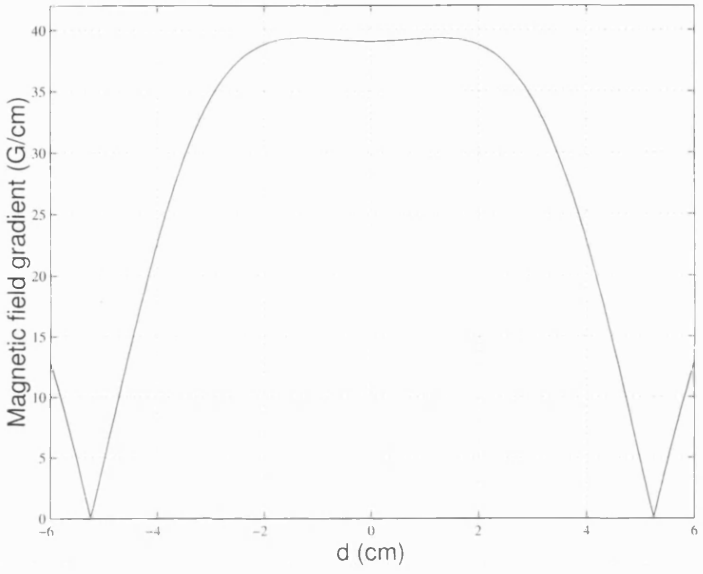

Figure 6.4: Magnetic field gradient generated from trap coils as a function of the distance from the trap center.

The geometry of the lattice (see figure 6.3) suggests a natural choice of a quantization axis, which is orthogonal to the plane of the lattice itself: the atoms trapped at different lattice sites where the light is σ-polarized present a magnetic moment along this axis, which we associate with the z-axis in the following. In the absence of in-plane stray magnetic fields, the projection of the magnetic moment along the quantization axis is preserved (see section 6.1), therefore the populations of the m_F states are preserved. However, in order to avoid population fluctuations due to precession around in-plane residual stray magnetic fields, we can introduce a uniform magnetic field along the $z-$axis as shown in figure 6.3, strong enough to maintain the orientation of the magnetic moment. This magnetic field is generated by a pair of coils oriented parallel to the lattice plane in Helmoltz configuration,

with a typical strength of $B_Z = 500$ mG.

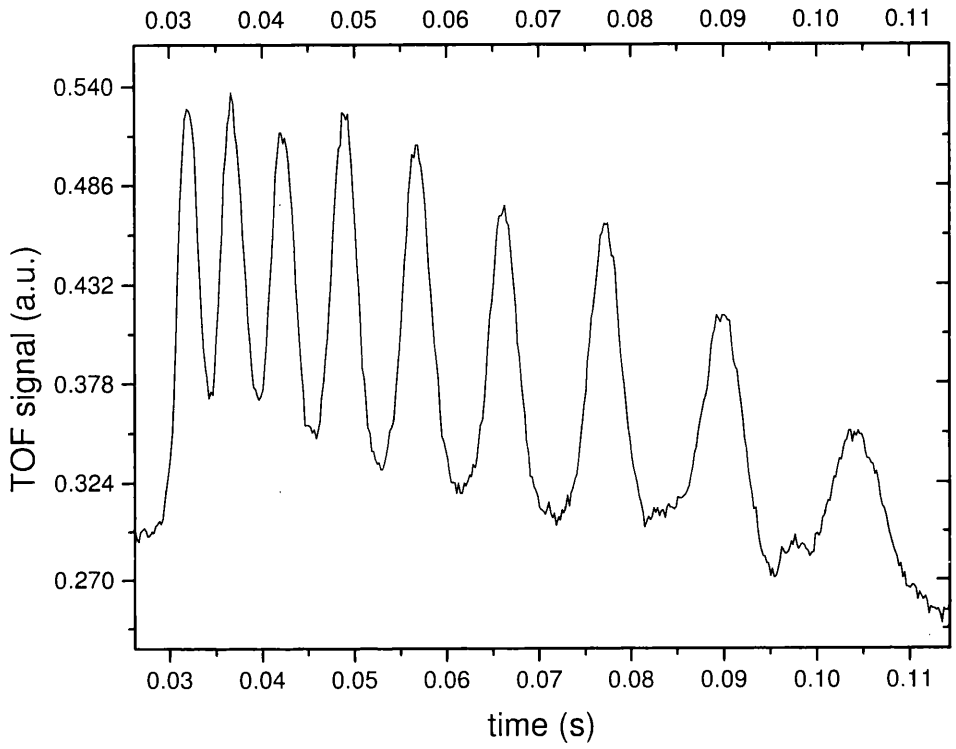

Figure 6.5: Spectrum of a Stern-Gerlach experiment in the near-detuned lattice.

A sequence of the experiment proceeds as follows. The atoms loaded in the lattice for different storage times are released and let free to fall. After $25 - 30$ ms (typically) the MOT coils are turned on, by ramping their current over 4 ms. The slow turn-on of the current in the trap coils is necessary in order to allow the magnetic moments to adiabatically follow the change in the magnetic field direction, while preserving the projection along the quantization axis, as shown by equation 6.9. For the standard value of current used, the magnetic field gradient is shown in figure 6.4, plotted against the distance from the center of the coils along the vertical direction. The atoms travel along the vertical axis for $\simeq 0.5$ cm, before the magnetic field gradient is switched on. This is necessary in order to guarantee that

the atoms do not cross the region where the quadrupole field vanishes while being accelerated; crossing a region of zero field would result in a loss of orientation of the magnetic moments. In our experiment the additional on-axis magnetic field guarantees the magnetic moment orientation will be maintained. If the orientation is not maintained, an atom could undergo opposite acceleration above and below the zero quadrupole field region, and therefore in the Stern-Gerlach spectrum, it would be difficult to associate a single peak to a specific m_F state. The magnetic field gradient is left on for 25 ms, during which time the atoms experience a force depending on their magnetic moment given by equation 6.10. This force is predominantly along the vertical direction and produces acceleration or deceleration on the atoms, which is actually space dependent, of about $\simeq (4 \times m_F)$ m/s^2. The atoms are accelerated enough to have different arrival times, according to their m_F state, as they fall though the probe beam located 5 cm below the MOT. The magnetic populations can then be determined from a fit of nine Gaussians to the time-of-flight distribution signal.

In figure 6.5 a typical TOF spectrum following a Stern-Gerlach experiment is shown: nine peaks corresponding to different magnetic sub-levels are resolved making it possible to extract information about temperatures and populations of the different Zeeman states.

In figure 6.6 the two spectra show the increased population of the two external $m_F = \pm 4$ stretched states, due to optical pumping with circular light in the far-off resonance lattice. A σ^+ or σ^- polarized beam was aligned orthogonal to the lattice plane with an intensity of $\simeq 0.5 I_S$ ($I_S = 1.12$ mW/cm^2) and was left to interact with the sample of cold atoms for 5 ms. This was especially useful in aligning the pumper beam with the quantization axis, since a misalignment results in the introduction of a π component of light, leading to a mixing of the m_F states, and thus resulting in a reduced efficiency of optical pumping to the stretched states.

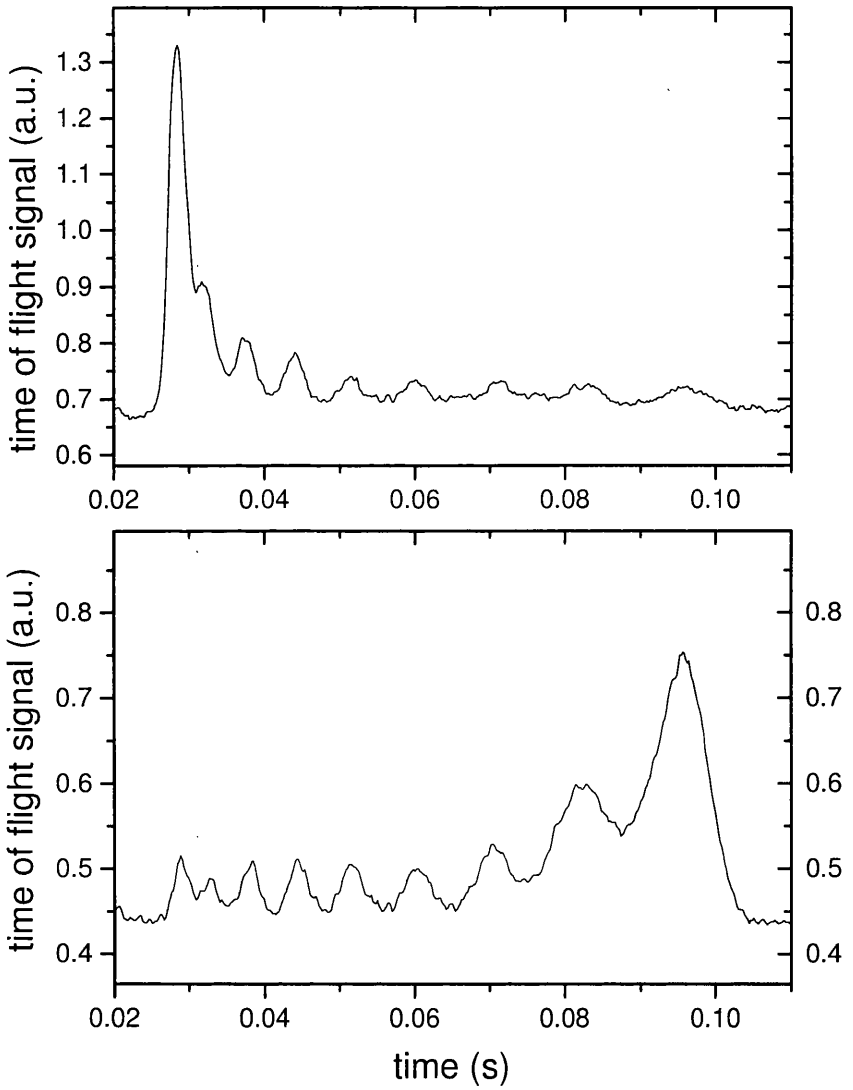

Figure 6.6: Spectrum of a Stern-Gerlach experiment in the far-detuned lattice showing the effect of σ^- and σ^+ optical pumping.

Figure 6.6 shows the efficiency of the optical pumping to the stretched states and also shows that there is residual population in the other m_F levels. This is probably due either to stray fields in the lattice plane, which generate mixing of the sub-levels, or to a non-perfect alignment of the pumper beam axis. By

maximizing the population in the $|m_F = \pm 4\rangle$ Zeeman sublevels it was possible to align the pumper beam to the lattice quantization axis.

6.4 Magnetization and spin temperature in the near-resonant lattice.

A set of experiments was also performed, aimed at the study of spin-polarization through the introduction of a magnetic field along the z-axis during the near-detuned lattice. As previously explained, this technique was investigated in an attempt to optimize sideband-Raman cooling, by increasing the population in the m_F potential well in which the cooling is working (see chapter 2). The efficiency of cooling should be increased by reducing the interaction of the atomic sample with the σ-polarized pumper beam, thus minimizing the heating and by increasing the cooling rate. The cooling time should be therefore decreased and the efficiency optimized.

In the case of a two-spin system and in the absence of a magnetic field, it should be expected that half the atoms would be in the spin up state and half the atoms in the spin down state. If a magnetic field is applied, some of the atoms will tend to align, so as to minimize the energy of the system, thus more atoms should be in the lower-energy state. Similarly, in our case, spin-polarization can be achieved by introducing a magnetic field along the z direction during the near-detuned lattice phase, where the interaction of the atoms with light can be exploited in order to increase the population of the stretched states [48]. Optical potentials generated by the light-shift of ground states with $F \geq 1$, are associated with space-dependent superpositions of the various Zeeman states. When a static magnetic field $\mathbf{B_z}$ is introduced in the direction orthogonal to the lattice plane, each Zeeman sub-level is shifted. The transition probabilities among the Zeeman sub-levels, induced by Raman coupling, are also altered. The corresponding field-induced

steady-state magnetization was found to display a quasi-thermal dependence on B, characterized by a phenomenological spin temperature [48], [12], which was found to be different from the kinetic temperature of the sample. This means that different mechanisms of energy exchange are involved, as will be discussed later, which act on different time-scales. For this reason we can talk of quasi-thermal equilibrium for the spin mode of the system: the isolated (translational and spin) modes still exchange energy one with the other (as it happens for a system in thermal equilibrium where the energy is stored in different modes - corresponding to the various quantum states accessible to the system -), but the time-scale of this exchange is much slower than for the exchanges within the isolated mode.

Depending on the direction of the magnetic field and on the polarization of the lattice light at a certain lattice site, the static magnetic field is either parallel or antiparallel to the fictitious magnetic field associated with the light shift. This asymmetry leads to a steady-state population imbalance between the atoms trapped at σ^+ or σ^- locations, as shown in [48].

The effect of the introduction of a static magnetic field parallel to the lattice axis was reported for the first time in [48]: the observation of paramagnetic behaviour of a three-dimensional caesium optical lattice was presented and the existence of a characteristic spin-temperature was shown. Subsequently in [12], a study of the induced magnetization in a one-dimensional optical lattice by means of a transverse magnetic field led to the confirmation of a characteristic spin-temperature for the sample of atoms; the results were also used to demonstrate the importance of Sisyphus cooling within single light-shift potential wells for atoms with large F. In [32] weak magnetic fields were used to enhance laser cooling and state preparation and to show that coherent mixing and local energy relaxation play important roles in laser cooling of large-F atoms. This was reinforced by finding that, in the presence of a magnetic field parallel to the lattice axis, the atoms

separate in two subsets (corresponding to σ^+ or σ^- lattice sites) with different temperatures, indicating that, for large F, cooling occurs locally at each lattice site.

In this section a simple model for quasi-thermal spin population distribution is presented. Results from spin-polarization experiments are then shown and discussed in the last part.

6.4.1 A model for quasi-thermal distribution of spin population

From previously published experiments [48, 12], it was reported that atoms trapped in a near-detuned paramagnetic optical lattice have a quasi-thermal behaviour. This means that the population distribution over different Zeeman states corresponds to a Boltzmann distribution. Herein a simple model is presented, which simulates the population distribution over the different magnetic sub-levels assuming that the atoms are in thermal equilibrium. The model does not take into account the potential modulation and the Raman coupling, but it treats the different Zeeman states as a discrete set of energy levels which are populated according to a Boltzman distribution. I will discuss later in this section the limitations of the validity of this model.

When the atoms are localized at the bottom of the potential well the light shift can be characterized by a scalar component independent of the m_F number plus a vector component, which acts as a magnetic field shifting the Zeeman levels. This fictitious magnetic field depends on the local light polarization, as shown by equation 2.5, and is therefore not constant, but varies with the position. If the atoms are well localized at the bottom of the potential well generated in the 2D configuration that we used, then the B_{fict} is maximum, the light being purely circular polarized at these locations. Moving away from the bottom of the potential well, the light polarization changes, which reduces the B^z_{fict} compo-

nent along the quantization axis. A smaller B^z_{fict} corresponds to less separation between the potential wells associated with different Zeeman sublevels, and an increased Raman coupling among them, due to transverse components of the fictitious field, which allows atoms to change m_F state. If the atoms are well localized at the bottom of the potential, then it is justified to assume a constant characteristic B_{fict}, as the one at pure σ polarization. We can simplify the treatment by assuming this condition is accomplished, but obviously this constitutes only an approximate description and the net effect of the effective magnetic field is necessarily overestimated. Assuming a quasi-thermal dependence of the Zeeman population on the total magnetic field, a phenomenological spin temperature can be introduced. Using standard statistical arguments, for an ensemble of atoms in thermal equilibrium, the population ratio of two energy levels is given by

$$\frac{\Pi_1}{\Pi_2} \propto \exp \frac{E_2 - E_1}{k_B T_S}, \tag{6.11}$$

where E_1, E_2 are the energies of the levels involved and T_S is the system temperature; what we call in this case the spin temperature. The energy of the levels depends on the light shift (which is a constant function of m_F) and on the Zeeman shift, which is given by $g m_F \mu_B B$, with $g = \frac{1}{4}$; B is projection of the sum of the real and fictitious magnetic fields along the quantization axis. In this picture, at the potential minima at sites of exact σ^+ and σ^- light polarization, the population distribution over the m_F levels will be:

$$\text{at} \quad \sigma^+ : \qquad \frac{\Pi_{m_F}}{\Pi_{m_0}} = \exp \frac{\frac{1}{4}\mu_B(B_{fict} + B_z)}{k_B T_S} m_F \tag{6.12}$$

$$\text{at} \quad \sigma^- : \qquad \frac{\Pi_{m_F}}{\Pi_{m_0}} = \exp \frac{\frac{1}{4}\mu_B(-B_{fict} + B_z)}{k_B T_S} m_F \tag{6.13}$$

where B_z is a static magnetic field added along the quantization axis and Π_{m_0} is the population of the $m_F = 0$ level. Simulations were run to monitor the population evolution for a varying static magnetic field. The significant parameters are the spin temperature and the effective magnetic field, which modify the initial

population distribution and the characteristic behaviour when the static magnetic field is introduced. In figures 6.7 and 6.8, the populations of different magnetic sub-levels are plotted versus the magnetic field, for an assumed 2.5 μK and 5.0 μK spin temperature respectively. Each of the two figures shows the population distribution for two different effective magnetic fields, 30 mG and 120 mG. In the inset the central region corresponding to a zero external magnetic field is shown in detail. When the B_{fict} is larger, for zero static magnetic field, the populations of the different magnetic levels are different, with the external states being more populated (figure 6.7). This difference in population is reduced for higher spin temperatures, as shown in figure 6.8.

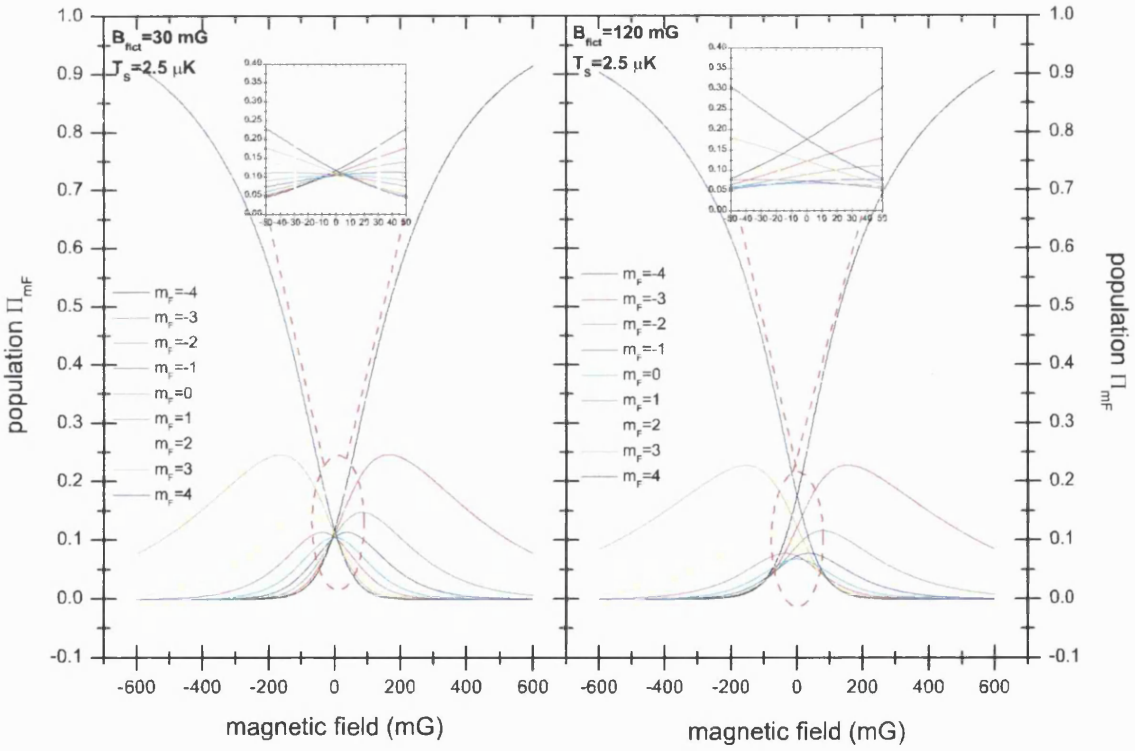

Figure 6.7: Population of different Zeeman levels versus static magnetic field, when a spin temperature of 2.5μK is assumed, for B_{fict} = 30 mG and B_{fict} = 120 mG. In the inset the central region of null external magnetic field is expanded.

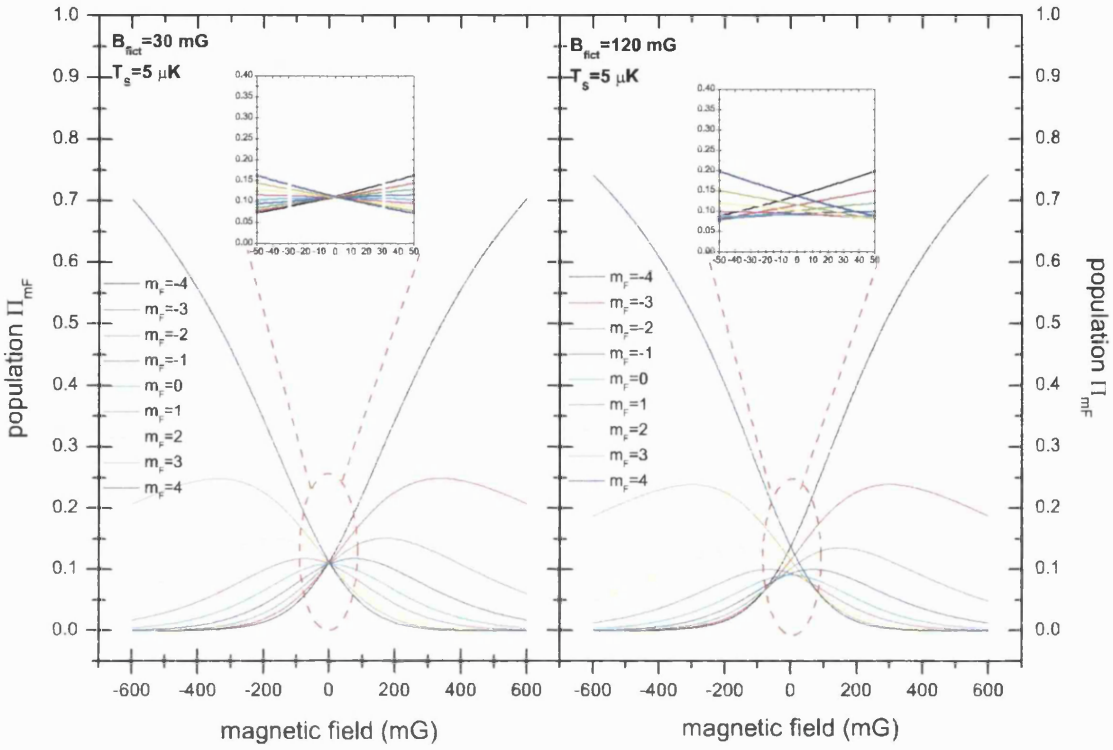

Figure 6.8: Population of different Zeeman levels versus static magnetic field, when a spin temperature of 5μK is assumed, for $B_{fict} = 30$ mG and $B_{fict} = 120$ mG. In the inset the central region of null external magnetic field is expanded.

This model is only valid in the low magnetic field regime, as it does not take into account potential structure and the spatial modulation of the energy levels. From figures 6.8 and 6.7, the maximum magnetization versus magnetic field is extracted and found to increase up to a maximum value $\langle m \rangle = \pm 4$ for positive and negative fields. This does not correspond to the real behaviour, as we shall see in section 6.4.2, where the experimental results are shown. In [12] the maximum magnetization achievable was explained as depending on the potential depth. Shallow wells produce less localization and cooling, thus resulting in unbound atoms which would diffuse through the lattice. This would also result in a reduced net polarization. Furthermore, the value of the magnetic field for which

the magnetization is maximum is associated with a well defined relationship of the light-shift and Zeeman shift; maximum magnetization is obtained when the adiabatic potentials of the different Zeeman states are only just separated. For stronger magnetic fields, the net magnetization decreases, due to the fact that, when the potentials are further separated, the Raman coupling among them is reduced and the eigenfunctions associated with the lowest adiabatic potential become pure $|m_F = 4\rangle$ or $|m_F = -4\rangle$. This suggests that, when the Raman coupling between different wells is much reduced, the atoms trapped at different wells are no longer in thermal equilibrium and can be considered as independent systems. When B is sufficiently large the highest adiabatic potential is shifted enough to become capable of trapping atoms again, and the net magnetization tends to decrease towards zero.

6.4.2 Spin-polarization experiments

The spin polarization method was used in order to increase the number of atoms in the desired stretched states in the near-detuned lattice, prior to the loading of the far-detuned lattice. This should improve the efficiency of sideband-Raman cooling by avoiding unnecessary heating related to optical pumping and in turn increase the population of the ground vibrational state (see chapter 7). The population distribution in the far-detuned lattice was also monitored, and it was shown that the distribution found in the NDL was almost entirely preserved in the FDL. Such a preparation should result in the increased efficiency of the Raman-cooling technique, as the atoms would not need to scatter σ pumping light in order to be transferred to the stretched state, where the cooling is efficient (see section 7.2). In this way the cooling time can be shortened and the heating due to the interaction with resonant light reduced.

The configuration of the beams that was used gives rise to an anti-ferromagnetic

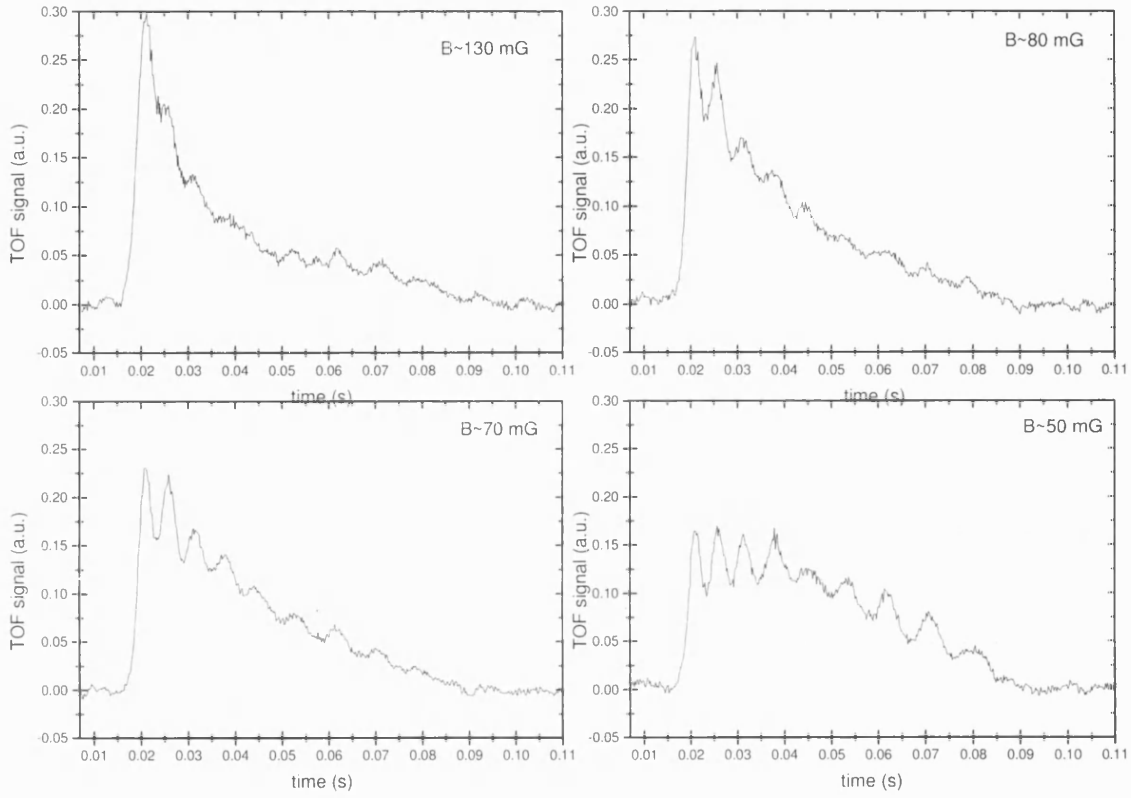

Figure 6.9: Spectrum of a Stern-Gerlach experiment in the far-detuned lattice, showing the effect of spin-polarization obtained by adding a small longitudinal magnetic field during the near-detuned lattice phase.

type of lattice, with adjacent well sites associated with opposite circular polarization of the light field. Atoms trapped at adjacent sites therefore have oppositely oriented magnetic moments. The atoms are distributed among the potential minima with an equal probability of occupying one σ^+ and one σ^- potential well. If a longitudinal magnetic field is introduced in a near-detuned lattice, there will be an opposite shift in energy for the potential corresponding to negative m_F and the one corresponding to positive m_F. The population distribution over the wells changes and the number of atoms increases in the wells with lowest potential

energy. The net result is that of a magnetization of the lattice.

A series of experiments was performed, aimed at increasing the population in the stretched state $|m_F = -4\rangle$, in order to prepare the sample of atoms for optimized Raman cooling (see section 6.4). A sample of spectra taken for different values of the magnetic field is shown in figure 6.9, for a potential depth of $120E_R$ and a measured kinetic temperature of $(4.5 \pm 0.2)\mu$K. A small static magnetic field was added during the near detuned lattice phase so that the atoms were preferentially populating potential wells corresponding to a m_F state of given sign. It should be noted here that the value of static magnetic fields reported in figure 6.9 is the nominal B_z; this means that the real external field is a sum of this value plus any magnetic field offset B_0, that may be due to non-compensated stray fields or an offset in the current of the magnetic coils. The near-detuned lattice was left on for 5 ms, during which the magnetization was built. The sample was probed following its loading in the far-detuned lattice for 2 ms, where such a distribution had been shown to be preserved. The atoms were then released and a Stern-Gerlach analysis was performed, as described in previous sections. As mentioned above, spin-polarization experiments have been reported in [48] and [12]. In both experiments, though, it was only possible to compare the global populations of σ^+ and σ^- potential wells. However, the ability to perform Stern-Gerlach experiments allowed us to follow the evolution of the population of individual m_F states with varying B_z. In figure 6.10, the populations obtained from figure 6.9 are plotted versus the magnetic field strength. The population of the $\{m_F = -4, -3, -2, -1\}$ states increases with increasing the magnetic field strength. Each of the sub-levels shows a characteristic rise in population for increasing B and a maximum, which is dependent on the m_F number.

The maximum value for the net magnetization was found to be $\langle m \rangle = -1.45 \pm 0.2$ for a static on-axis nominal magnetic field of 90 mG. The maximum magneti-

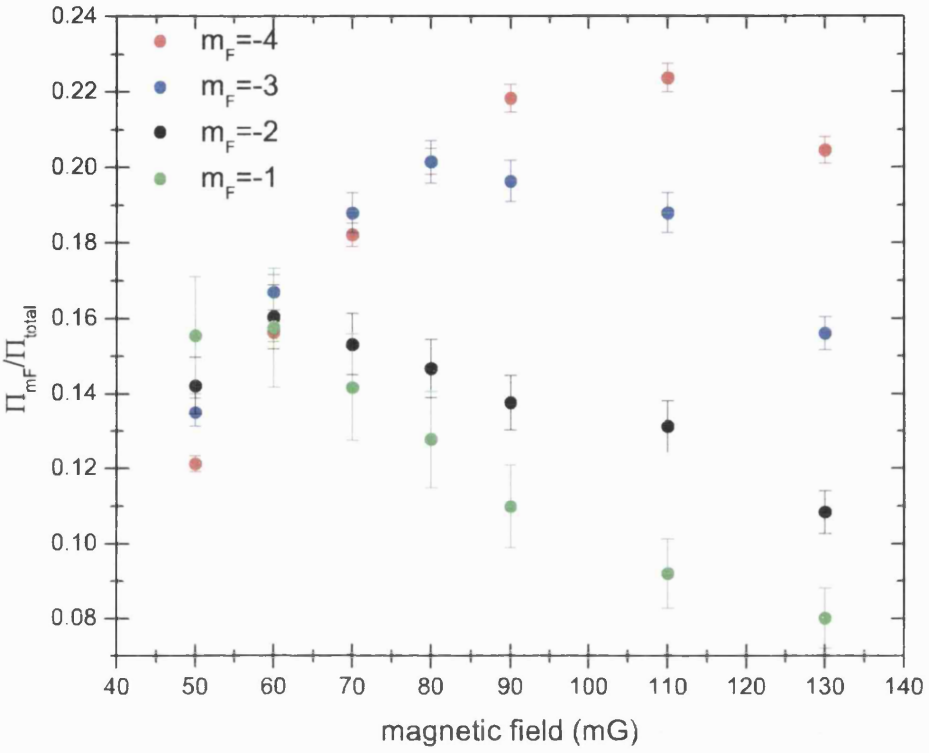

Figure 6.10: Populations of different m_F states plotted versus the magnetic field.

zation is obtained when the adiabatic potentials only just depart from each other, due to the Zeeman shift. For higher values of the magnetic field, the magnetization diminishes again as the potentials no longer overlap in energy and the Raman coupling between different levels vanishes. Then, as explained in [12] and in the previous section, the eigenfunctions of the light-shift Hamiltonian become single $|m_F\rangle$ states. For even higher magnetic fields, the higher lying potential becomes capable of trapping atoms and the atoms tend again to distribute equally over σ^+ or σ^- wells, thus reducing the net magnetization [12].

In figure 6.11 the ratio of the population of the $m_F = -4$ sub-level to that of the $m_F = -3, -2, -1$ sub-levels is shown as a function of the longitudinal magnetic

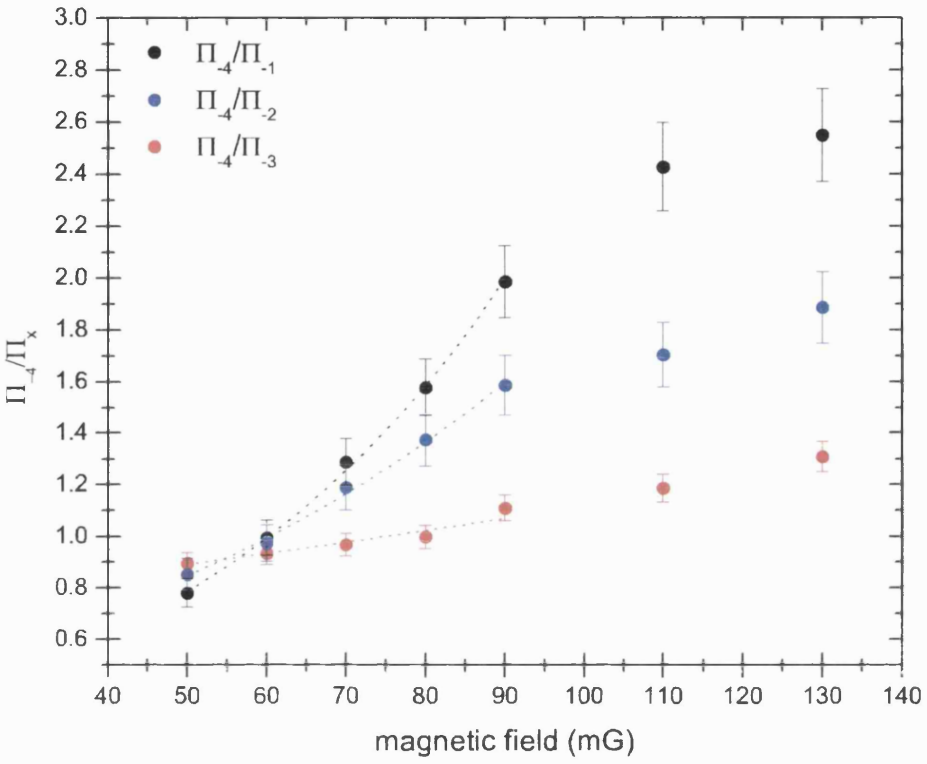

Figure 6.11: Population ratios $\Pi_{m_F=-4}/\Pi_{m_F}$ versus magnetic field.

field. For these data to be consistent with the existence of a well defined a spin temperature, they have to exhibit exponential behaviour. It is possible to recognize in all three sets of data an exponential growth at different rates for values of the magnetic field below 90 mG. For values of magnetic field above this, the ratios seem to reach a plateau and eventually decrease again. This is consistent with the explanation given above for the limit of the degree of polarization obtainable, as at higher magnetic field strengths the population of $m_F = 1, 2, 3, 4$ states starts rising again. It was therefore assumed that the spin temperature argument is valid for $B_z \leq 90$ mG.

If the assumption of the existence of a well defined spin temperature is valid,

it follows that the ratios of the populations of different m_F states versus magnetic field should follow a law:

$$\frac{\Pi_{m_{F_1}}}{\Pi m_{F_2}} \propto \exp -\frac{\mu_B B_{tot} \frac{1}{4}(m_{F_2} - m_{F_1})}{k_B T_S}, \tag{6.14}$$

where $B_{tot} = B_z + B_0 \pm B_{fict}$ depending on the Zeeman state quantum number. By taking the ratio of the measured population of two Zeeman states at the same lattice site, the dependence of the exponential on the effective plus offset magnetic fields can be factored out, thus leaving the exponential growth characteristic constant depending only on one unknown variable, which is the spin temperature. The spin temperature was then retrieved by fitting exponentials to the three sets of data in figure 6.11. The temperatures found from the populations ratios were $(2.2 \pm 0.1)\mu$K for Π_{-4}/Π_{-1}, $(2.3 \pm 0.1)\mu$K for Π_{-4}/Π_{-2} and $(3.2 \pm 0.8)\mu$K for Π_{-4}/Π_{-3}. The analysis of the spectra in figure 6.10 was limited to the levels $\{m_F = -4, -3, -2 - 1\}$ because of the reduced resolution of the spectra for $\{m_F = 1, 2, 3, 4\}$ levels; the low signal to noise ratio on this side of the spectra did not allow an accurate analysis of the level populations. This analysis showed that the introduction of a spin temperature argument was consistent with our set of data, and $T_S = (2.6 \pm 0.6)\mu$K was found to be the characteristic spin temperature of our system. This value is well below the measured kinetic temperature $T_K = (4.5 \pm 0.2)\mu$K, thus showing the distinct nature of the two. There is not a unique temperature that can describe the system, but two separate temperatures have to be assumed to characterize the motional and the internal degrees of freedom.

In figures 6.12 and 6.13, the populations of the different magnetic levels are plotted versus the m_F number, for a value of the nominal external magnetic field of 90 mG. According to equation 6.14 the populations should follow a geometric series behavior, of the type a^x, where $a = \exp\left[-\frac{1/4\mu_B(B_z+B_0\pm B_{fict})}{k_B T_S}\right]$ (for $\sigma^{\pm}$ wells respectively) and $x = m_F$. For varying m_F, the data points with $m_F < 0$ follow

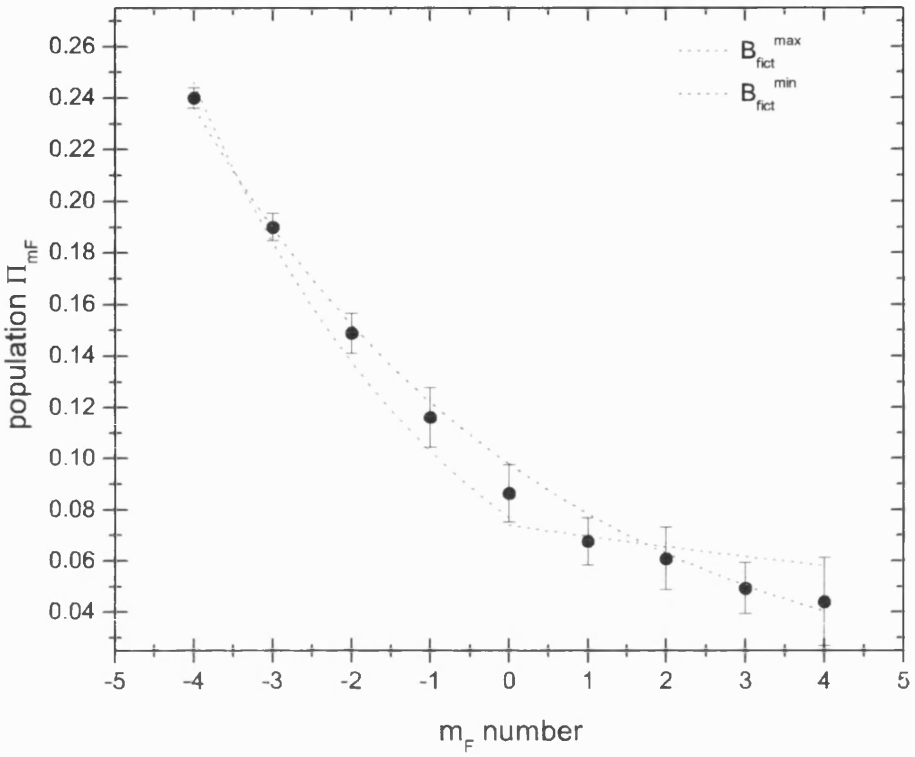

Figure 6.12: Population distribution among the m_F states for B_Z=90 mG. The red dotted lines (two exponentials fitted to $[m_F = -4 \rightarrow m_F = 0]$ and $[m_F = 0 \rightarrow m_F = 4]$ data sets separately) allow the evaluation of B_{fict}^{max}. The blue dotted ones (two exponentials fitted to $[m_F = -4 \rightarrow m_F = 0]$ and $[m_F = 0 \rightarrow m_F = 4]$ data sets separately) allow the evaluation of B_{fict}^{min}

a different exponential behaviour compared to the ones for $m_F > 0$. Therefore two distinct exponentials have to be fitted to the $[m_F = -4, -3, -2, -1, 0]$ and $[m_F = 0, 1, 2, 3, 4]$ sets of data, one with a decay constant proportional to $B_{fict} + (B_z + B_0)$ and the other with a decay constant proportional to $B_{fict} - (B_z + B_0)$. Assuming a unique spin temperature for σ^+ and σ^- wells and fitting two different exponential curves, it is therefore possible to estimate B_{fict}. It was assumed that the spin temperature, $T_S = (2.6 \pm 0.6)\mu$K, measured from the exponentials fitted in figure 6.11 was valid for both potential wells. It has to be pointed out here that from the experimental data it is only possible to estimate an *effective* fictitious

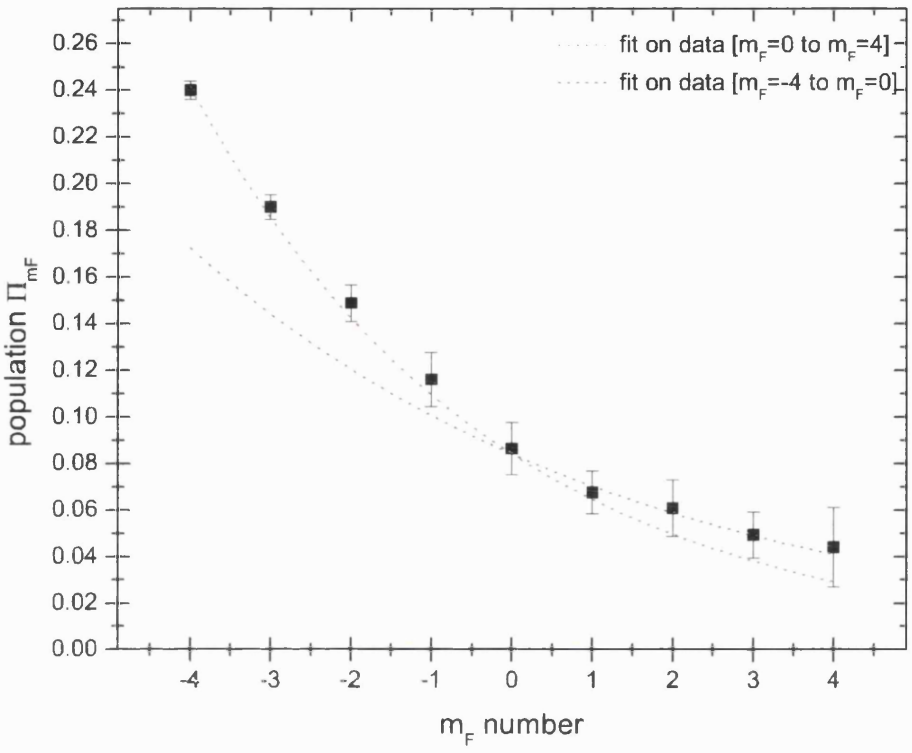

Figure 6.13: Population distribution among the m_F states for B_Z=90 mG. The red dotted line represents the exponential fit to the data set $[m_F = -4 \rightarrow m_F = 0]$, the blue dotted line is the fit to the data set $[m_F = 0 \rightarrow m_F = 4]$. From the fitted values follows $B_{fict} = (10 \pm 3)$ mG

magnetic field (B^*_{fict}) that takes into account the averaging of B_{fict} over an atomic wavepacket.

In figure 6.12 the populations of different Zeeman states are plotted versus their m_F number. This set of measurements is particularly affected by errors in determining the population of states with $m_F > 0$, due to the low resolution of the time-of-flight signal. Therefore, before performing a fit to the data, the range of possible values for the fictitious magnetic field was estimated as follows. B_{fict} increases with increasing difference between the decay constants of the two exponentials (corresponding to $m_F \leq 0$ and $m_F \geq 0$). In order to evaluate the maximum value for the fictitious field which is compatible with the data, the red

dotted curves were matched to the data, which showed the biggest difference in characteristic constant being compatible with the data set within the error bars. When the fictitious magnetic field decreases, the characteristic decay constants become comparable and, in the limit of very small fictitious magnetic field, an almost identical exponential can fit both data sets. The blue dotted lines represent the exponentials which lead to the minimum value for the fictitious field, and they show that there is very little difference between the two exponentials. From this preliminary analysis, the estimated maximum and minimum values were found to be ${B^*_{fict}}^{max} = 30$ mG and ${B^*_{fict}}^{min} = 5$ mG. It follows that the effective fictitious magnetic field is very weak (below 30 mG) and that an almost null fictitious field would also be compatible with this set of data.

In figure 6.13 fits are performed on the two sets of data, weighted by the errors. The red (blue) curve represents the fit to the $m_F \leq 0$ ($m_F \geq 0$) data points. Assuming again a spin temperature $T_S = (2.6 \pm 0.6)\mu$K, the measured effective fictitious magnetic field is then $B^*_{fict} = (10 \pm 4)$ mG. The B_{fict} calculated for a maximum potential depth of $120E_R$ is 150 milliGauss, so the result would not seem to be consistent. It should be borne in mind that the light intensity is not uniform over the trapping region, as shown in section 4.2. The non-uniformity of the lattice depth along the trapping region leads to a spread of B_{fict} values for atoms at different locations. Furthermore the degree of excitation of the atoms would change the effective fictitious field that they perceive. If the atoms are not well localized near the bottom of the potential well the resulting net effective fictitious field would be reduced. Another possible explanation is the non-perfect alignment and polarization of the beams: a slight misalignment or tilt in one of the beams polarization would change the local polarization at different lattice locations, thus reducing the effective field. It should also be pointed out that this set of measurements was particularly affected by the low resolution of the

time-of-flight signal for the $m_F = 1, 2, 3, 4$ states.

Our set of measurements is shown to be consistent with the introduction of a spin temperature. They reveal, however, that the spin temperature is different from the kinetic temperature. There is not a unique temperature that can describe the steady state of the system; it is possible, however, to associate a kinetic temperature to describe the motional degrees of freedom and a spin temperature to characterize the internal degree of freedom. An estimate of the effective fictitious magnetic field has been attempted, which was limited by the poor resolution of the time-of-flight signal. However this study showed that the atoms in the lattice wells experience a reduced fictitious field, due to the non-homogeneous potential depth along the lattice region, the polarization mixing of the beams and the spread of the atomic wavepacket . Work is being done at the moment attempting to improve the resolution of the time-of-flight Stern-Gerlach signal, to further investigate the paramagnetism. A better method to carefully check the alignment and the polarization of the beams has to be implemented. A more powerful laser has been purchased, which should allow us to expand the lattice beams and select a region of uniform intensity. Once these improvements have taken place, it would be useful to investigate the population evolution for both positive and negative magnetic field for all the magnetic levels. A more accurate study of the fictitious magnetic field should be undertaken. Furthermore measurements of the time necessary to build the magnetization as well as the characteristic time of relaxation of the magnetization could be analyzed. A study of the maximum magnetization versus potential depth could yield important information on the structure of the lattice potential.

6.5 Conclusions

In this chapter I described a technique that allowed the measuring of the populations of single Zeeman substates in the near-detuned and far-detuned lattices. This technique is based on Stern-Gerlach experiments aimed at resolving the different m_F-states time-of-flight signals. A Zeeman-state analysis of the sample allowed the measurement of the magnetization of the atomic sample. The efficiency of this method was demonstrated by studying spin-polarized samples in the near-detuned lattice, by adding a static magnetic field to Zeeman-shift the m_F energy levels. The evolution of the population of such states was reconstructed whilst varying the external static magnetic field along the quantization axis. Spin-polarization was proved to be efficient and a well-defined phenomenological spin-temperature could be evaluated, in agreement with the results presented in [48]. Furthermore, the possibility of measuring the population of the single Zeeman states gave more convincing proof for the existence of a spin temperature than the results presented in [48], where only the total population of a $\sigma^{\pm}$-well could be measured. Zeeman state analysis also enables us to verify that the net magnetization of the sample in the near-resonant lattice is preserved when it is transferred to the far-detuned lattice. In particular it allows the preparation and measurement of a large fraction of atoms in the $|m_F = \pm 4\rangle$ state, which could improve the efficiency of the sideband-Raman cooling scheme used for quantum state preparation.

CHAPTER 7

Resolved Sideband-Raman Cooling

In recent years many groups have been working at developing techniques for quantum state preparation and control for laser cooled atoms. Experiments aimed at the coherent manipulation of quantum states have also been performed, generating Fock coherent states, squeezed states [50] and Schrödinger cat states [15]. Demonstration of quantum logic gates as discussed in [51], opens the way toward quantum computation. Sideband cooling between hyperfine levels was also used to prepare a trapped ion in the motional ground state, a minimum uncertainty state and therefore a good starting point for experiments in quantum state control [51], [52]. The method required the use of two lasers which are phase-locked and with a difference in frequency given by the spacing between the levels used for cooling. Anti-Stokes processes are stimulated in this way, thus cooling the sample of atomic ions. A similar technique has been employed in [53] for neutral atoms in a one-dimensional optical lattice.

In [20] a scheme for resolved-sideband Raman cooling in a 2-D far-detuned optical lattice was demonstrated. In this scheme the cooling is introduced by means of stimulated Raman transitions between degenerate vibrational levels of a pair of different Zeeman sub-levels. The resonant Raman coupling required for

cooling can be engineered in the lattice itself, using an appropriate choice of beam polarizations. Atoms sideband cooled to the motional ground state at different lattice sites are in identical quantum states, which difference each other only by an arbitrary phase-factor.

In this chapter, I describe our implementation of a resolved-sideband Raman cooling technique, based on the method demonstrated in [20], whose basic principles were described in chapter 2, and the results of our experiments.

7.1 Experimental setup for resolved-sideband Raman cooling

The experimental set-up which was used in order to implement the Raman cooling scheme described in section 2.4, is shown in figure 7.1. The lattice setup consists of three coplanar beams at an angle of 120 degrees between each pair, as shown in figure 6.3, intersecting at the trapping region. The lattice plane contains the gravitational axis; this is necessary to allow long trapping times and also to enable the use of the time-of-flight method (section 3.8) as a diagnostic tool.

In order to introduce an appropriate Raman coupling according to the scheme of section 2.4, it is necessary to provide a π-component of the laser light. This is obtained by tilting the polarization of one of the lattice beams out of the lattice plane by 10^{o} typically. Additionally, a $\lambda/4$ plate provides a $\pi/2$ phase difference between the two components, which is required to optimize the cooling (see chapter 2). The coupling introduced by the π light induces transitions from $|m_F = -4, n\rangle$ to $|m_F = -3, n-1\rangle$ states. Relaxation back to the vibrational manifold of the $|m_F\rangle$ state is driven by optical pumping, as shown in figure 2.8. For this purpose, a σ^--pumping beam is added along the $z-$axis, resonant with the $|F = 4\rangle \rightarrow |F' = 4\rangle$ transition. A repumper beam, tuned to the $|F = 3\rangle \rightarrow |F' = 4\rangle$ transition and σ^--polarized is also added. The repumper beam repopulates the

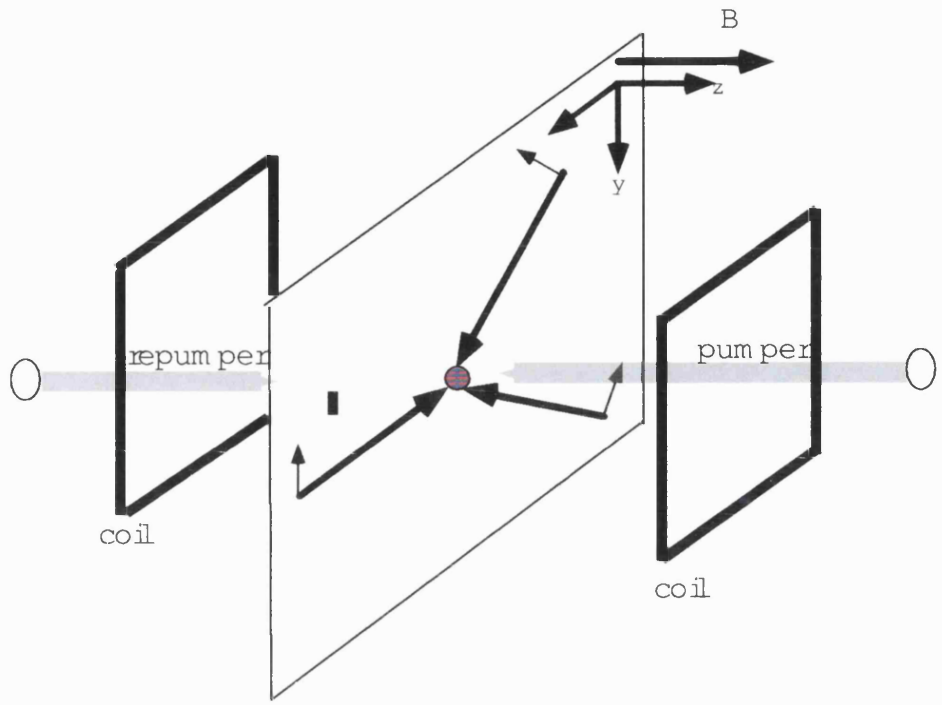

Figure 7.1: Experimental setup for resolved sideband Raman cooling on a 2-D optical lattice.

$|F' = 4\rangle$ state of the atoms which decay to the $|F' = 3\rangle$. Both the pumper and repumper beams are set to be propagating in the direction perpendicular to the lattice plane (i.e. the quantization axis) being opposite with respect to each other. This guarantees also a minimum net momentum transfer during the interaction of the lasers with the atoms. In order to increase the efficiency of cooling the $|m_F = -4, n\rangle$ and $|m_F = -3, n-1\rangle$ levels have to be brought into degeneracy. This is accomplished by adding a static magnetic field along the quantization axis which shifts the potentials, as explained in section 2.4. For this purpose a pair of coils in Helmoltz configuration were placed with their common axis orthogonal to the lattice plane, along the $z-$direction. These were used to generate a uniform static magnetic field in the trapping region, of a flux density up to 0.5 G. The static magnetic field is tuned to the proper value, derived from a consideration of the

band structure (see section 2.4), to bring into degeneracy the vibrational levels in adjacent wells involved in cooling. This method provides efficient two-dimensional cooling, when the initial temperature of the sample is sufficiently low. In this case the lowest lying vibrational levels are mostly populated in both dimensions, so simultaneous cooling in 2-D is driven with the same value of magnetic field. The typical parameters used for the lattice are $U_{max} = 200E_R$ and $\Delta = 3000\Gamma$. These values give a vibrational frequency of $\omega_{vib} = 35$ kHz, while the scattering rate results to be $\Gamma_s = 200$ Hz. As was mentioned in chapter 4, the heating induced by spontaneous scattering becomes significant for long times, so there is a constraint on the duration of the Raman cooling period. In the Lamb-Dicke regime the atoms mostly spontaneously scatter photons elastically. The probability per photon for there to be a net increase of one vibrational quantum is reduced, but it was shown in [54] that the average increase in energy per spontaneous scattering cycle (a two-photon process) is $2E_R$, the same as for a free atom. The heating produced by spontaneous photon scattering during an experiment time t_{cool} can be therefore calculated as $t_{cool}\Gamma_s E_R \ll \hbar\omega_{vib}$; this condition is guaranteed for $t_{cool} \ll 80$ ms. The cooling time is in general set to 10 ms, which insures that the spontaneous scattering induced heating is not significant.

7.2 Resolved-Sideband Raman cooling

The experiments start with the atoms being prepared in a 3-D magneto-optical trap and then transferred to an optical molasses, where they are cooled to the sub-Doppler regime. The cooled sample is then loaded into a 2-D near-detuned optical lattice for typically 5 ms, where the atoms reach a temperature of $\simeq 3\mu$K. During this phase a static magnetic field is introduced in the direction perpendicular to the lattice itself, in order to spin-polarize the sample and increase the population of atoms in the $|F = 4, m_F = -4\rangle$ state. As discussed in chapter 6, this process

can be quite efficient, thus increasing the number of atoms in the stretched m_F state. As mentioned in section 2.5, the initial distribution of atoms over different vibrational and Zeeman levels is important for the efficiency of this method of cooling.

Once the atoms are cooled and localized in the Lamb-Dicke regime, with an increased population in the $m_F = -4$ potential well, they are transferred to the far-detuned lattice. The far-detuned beams are superimposed on the near-detuned ones (see chapter 4). Transfer from the NDL to the FDL is obtained by simultaneously ramping the intensities of the far-detuned and near-detuned beams, as explained in the far-detuned lattice section. The transfer usually last 400μs. As shown in chapter 4, a transfer efficiency of $\simeq 90\%$ was typically achieved. By carefully matching the lattice beams paths and choosing the right potential depth, it was possible to load the far-detuned lattice with minimal increase in temperature over that of the near detuned one. Typical temperatures achieved were in the range of $(2.5 - 3.5)\mu$K, for $U_{max} = 200E_R$ and $\omega_{vib} = 35$ kHz.

When the longitudinal magnetic field is set to the appropriate value and the Raman coupling is introduced, a coherence between states $|m_F = -4, n\rangle$ and $|m_F = -3, n-1\rangle$ is established. Two isoenergetic photons, one σ and one π polarized are required to induce the transition. The atoms which are then transferred in the $m_F = -3$ well will scatter photons of the pumping σ^- polarized laser and will be preferentially pumped back to the $m_F = -4$ well. Due to the tight confinement of the atoms in the Lamb-Dicke regime, the spontaneous emission of a photon from the excited atom is most likely to return it to a state with the same vibrational quantum number it has just left. Atoms decaying to $|m_F = 3\rangle$ may be re-excited by the pumping laser, and atoms decaying to $|m_F = 4, n \neq 0\rangle$ are coherently transferred again to $|m_F = -3, n-1\rangle$, where the cooling cycle is repeated. After several cycles, the atoms end up in the $|m_F = -4, n = 0\rangle$ state.

This is a 'dark state', as there is no state in $|m_F = -3\rangle$ to establish a coherence with and there is a natural termination to the cooling cycle.

7.2.1 Resolved-sideband limit and causes of broadening

In the resolved-sideband limit it is required that the width of the resonances is much smaller that the separation between two vibrational levels. This in turn means that the coherent population transfer rate has to be much smaller than the vibrational frequency characteristic of the lattice:

$$\frac{|U_R|/\hbar}{\omega_{vib}} \ll 1, \tag{7.1}$$

where U_R is the Raman coupling, defined in section 2.4. Inserting the definition for U_R, equation 7.1 becomes:

$$\frac{|U_R|/\hbar}{\omega_{vib}} = \left(\frac{U_1/\hbar}{\omega_{vib}}\right)\left[\frac{1}{2\sqrt{2F}}\frac{E_\pi}{E_1}\left(\frac{2E_R}{15U_1}\right)^{\frac{1}{4}}\right]. \tag{7.2}$$

The first bracket on the right hand side of equation 7.2 is approximately the number of bands in the well and the second bracket may be evaluated by using typical parameters used in the experiment: $E_\pi/E_1 = 0.1$, $U_1/E_R = 44$ and $F = 4$ for the transition that was used. Using these values we have $\frac{|U_R|/\hbar}{\omega_{vib}} \simeq 0.04 \ll 1$, so the sidebands should be expected to be well resolved. This condition is fulfilled over a large range of values which would include the most reasonable experimental parameters.

There are other mechanisms, though, that could lead to a broadening of the Raman resonances. As shown in chapters 2 and 5, the spacing between vibrational bands is not unique, but varies with the band index, due to the anharmonicity of the light-shift potential. In figure 2.10 the values of magnetic field necessary to bring in resonance different $|m_F = 4, n_i\rangle$ with $|M_F = 3, n_i - 1\rangle$ states for $n_i = \{1, 2, 3, 4, 5\}$ are plotted versus the potential depth. Except in the case of a very shallow potential, it is possible to see that the magnetic field necessary to bring

sub-levels, whose energy differs by 1 quantum, into degeneracy is not unique, but depends on the band index n. For the Raman cooling to be efficient, it is therefore necessary to vary the strength of the magnetic field over the range which allows also the atoms in the higher-lying bands to be brought to a lower n level. This turned out to be particularly important if the population distribution is spread over many vibrational levels, i.e. when the starting vibrational temperature of the sample is high. Nevertheless, if the initial temperature is low enough for most of the atoms to be in the lower vibrational states, where the degree of anharmonicity is much reduced, then an efficient cooling can be obtained without scanning the magnetic field, as all the populated levels n are brought into degeneracy with levels $n-1$ simultaneously. The initial temperature is therefore a fundamental parameter that affects the efficiency of cooling. Other causes of reduced sideband resolution include inhomogeneity of the potential depth along the trapping region. As it will be shown later, this was actually found to be a major cause of broadening of the sidebands.

7.2.2 Experimental results

Typically a Raman cooling sequence was started immediately after the loading of the far-detuned lattice. Following the 400μs transfer time, the pumper and repumper beams were switched on and the $z-$axis magnetic field tuned. The time during which Raman coupling was effective was varied in order to optimise cooling, like discussed in section 7.1. The duration of Raman cooling cannot be increased indefinitely as, after a certain time, heating and loss of atoms become significant. The pumper beam intensity was set to $I_p = 0.06$ mW/cm^2.

A first set of Raman-sideband cooling sequences were run starting from a sample at a temperature of $(9.0 \pm 0.2)\mu$K, prepared in a lattice tuned 3000Γ to the red of the resonance with a maximum light shift $U_{max} = 200E_R$. The

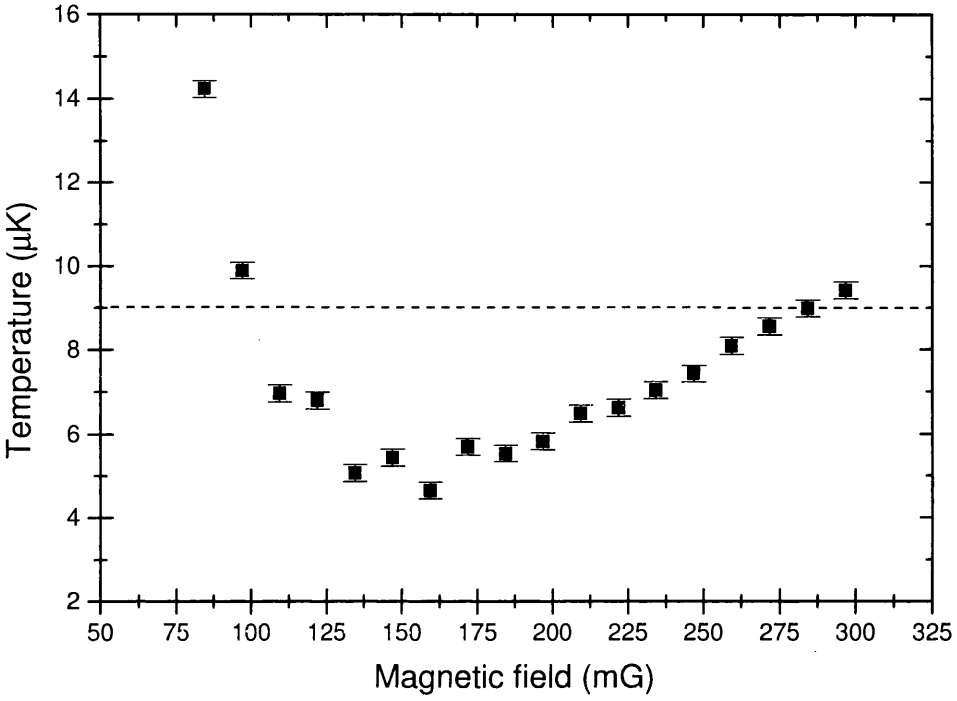

Figure 7.2: Temperature variation versus static magnetic field along the z-axis for a sideband Raman-cooled sample of atoms. The dotted line represents the initial temperature of the sample $T_{ini} = (9.0 \pm 0.2)\mu$K.

Raman pumper and repumper as well as the magnetic field where switched on as soon as the far-detuned lattice was loaded and were left on for 10 ms. The magnetic field was kept constant during the whole Raman-cooling phase. In figure 2.12 the population distribution over the vibrational levels $|n_x = 0, n_y\rangle$ for a 2-dimensional harmonic oscillator, shows that for a 9μK sample in a potential well with ground state kinetic energy $T_0 = 0.96\mu$K ($T/T_0 = 9.4$ with reference to figure 2.12), the atoms are populating a wide set of vibrational levels. Due to anharmonicity the values of magnetic field necessary to induce coherences among different vibrational levels are several, as shown in figure 2.10. In this case we need to calculate the band-structure appropriate to the 2-D lattice used in the experiment in order to determine the range of magnetic field required to bring

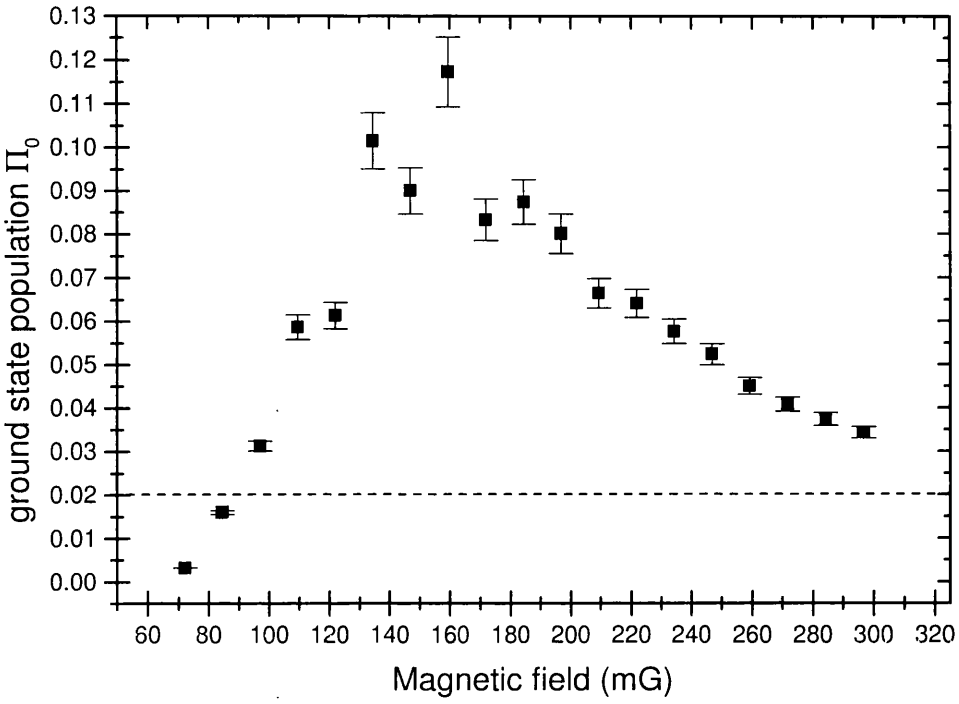

Figure 7.3: c Population of the 2-D ground state with $n_x = 0, n_y = 0$ versus static magnetic field along the z-axis for a sideband Raman-cooled sample of atoms. The dotted line represent the ground state population for the uncooled sample at a temperature of 9μK.

successively lower transitions to resonance. From these calculations, shown in section 2.4, it follows that to bring most of the atoms into the ground vibrational state the magnetic field should be varied over a 20 mG interval. However, by ramping the magnetic field over a range of values, the time for which a given pair of levels $(|m_F = -4, n\rangle, |m_F = -3, n-1\rangle)$ coherently interacts is reduced, thus limiting the cooling efficiency. If the magnetic field was to be scanned, then the Raman cooling phase duration would have to be increased adequately. But the heating rate due to photon scattering becomes relevant at long times, thus competing with the cooling processes. The net balance does not lead to improved cooling efficiency.

In figure 7.2 the temperature of the Raman-cooled sample of atoms is plotted

against the magnetic field flux density. The plot shows that there is a broad region over which the cooling is efficient and a drastic reduction of temperature was recorded, of up to $\Delta T = 5\mu$K. Two resonances would be expected by scanning the magnetic field, one corresponding to tuning to the first red sideband, i.e bringing into degeneracy the $|m_F = -4, n\rangle$ with the $|m_F = -3, n-1\rangle$ level, and another one, leading to a less efficient cooling, corresponding to tuning into degeneracy $|m_F = -4, n\rangle$ $|m_F = -3, n-2\rangle$ level (second red sideband). These should be separated by a ΔB given by:

$$\frac{1}{4}\mu_B|\Delta B| = \hbar|\Delta\omega|, \tag{7.3}$$

where $\Delta\omega$ is the separation between the n and $n-1$ vibrational levels in the $m_F = -4$ potential well. Thus for an expected vibrational frequency of $\simeq 35$ kHz it should be possible to distinguish two resonances separated by $\simeq 100$ mG, if these resonances had a width much smaller than the separation, from equation 7.2. In figure 7.2 two resonances are not resolved but this can be explained by observing that the spread of population over the vibrational levels due to the high initial temperature leads to a spread in the value of the magnetic field required to bring in resonance different vibrational levels, as discussed above (see figure 2.10, with $T/T_0 = 0.94$). This suggests that to have efficient cooling and to be able to transfer a large fraction of atoms into the vibrational ground state, it is necessary to start with a sample at low temperature such that a large fraction of atoms is already in the lower lying vibrational states;in this way the anharmonicity is negligible and all the $|m_F = -4, n_i\rangle$ levels can be brought into degeneracy with the $|m_F = -3, n_i - 1\rangle$ levels with the same value of Raman magnetic field. Nevertheless it has to be noted that the estimated 20 mG spread in resonant B fields due to anharmonicity of the potential well, does not completely account for the broadening in figures 7.2 and 7.3. As it will be shown later in this section, part of the broadening of the sideband resonances plotted in figure 7.2 can be

attributed to inhomogeneities of the optical potential, due to the spatial variation of the laser intensity over the lattice region.

The temperature was measured along the x-direction of the lattice plane, with reference to figure 2.7. Considering a 1-D harmonic oscillator, the population of the ground vibrational state with $n_x = 0$ has therefore been increased from 14% to 35%. In section 2.4 it was shown that this scheme for sideband Raman cooling allows the simultaneous cooling in 2-D, with an efficiency along the y-direction which is three times bigger than along the x-direction. Also, for low lying states, the 1-D potential wells along the two directions are practically identical. It is therefore reasonable to assume that the same temperature measured along the x-axis is also obtained along the y-axis, so that the ground state population can be calculated for a 2-D harmonic oscillator. In figure 7.3 the population of the 2-D ground state $n_x = 0, n_y = 0$ is plotted versus the magnetic field. This has been calculated according to equations 2.16 and 2.22 for a two-dimensional harmonic oscillator, with T_K the measured kinetic temperature. The ground state momentum distribution is equivalent to a temperature T_0 given by:

$$T_0 = \frac{\hbar\omega_0}{2k_B} \tag{7.4}$$

and is found to be $T_0 = 0.96\,\mu$K. In this calculation I assumed that the temperature of the sample is the same along the two lattice dimensions. Therefore the measured temperature along the vertical direction was assumed to apply for both directions. At maximum cooling the population of the ground state is increased by a factor of $5-6$, but still only 10% of the atoms are in the ground vibrational level. Increasing the pumper beam intensity or the π component did not increase the number of atoms in the ground state on this occasion.

In order to eliminate the broadening due to anharmonicity of the potential, further measurements were taken for lower starting temperatures for a sample of atoms which are mostly populating the lower lying vibrational levels. In figure 7.4

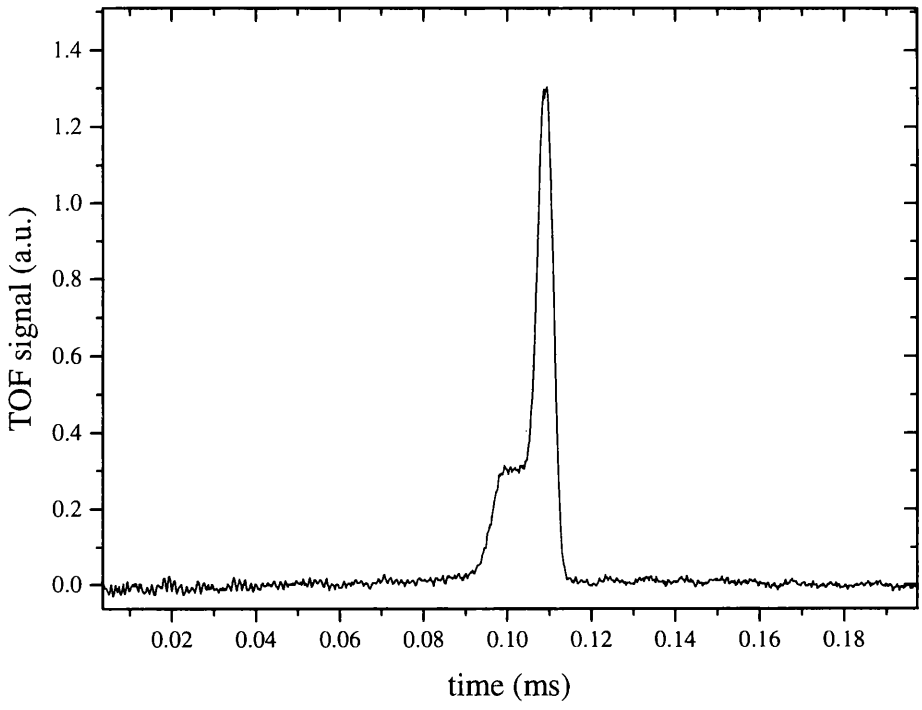

Figure 7.4: TOF signal of a far-detuned lattice with a kinetic temperature $T_K = (2.5 \pm 0.2)\mu$K.

a far-detuned lattice time-of-flight signal is shown for a sample at a temperature of $(2.5 \pm 0.2)\,\mu$K. It was found that very careful compensation of the static magnetic field was crucial in order to achieve very low temperatures. The far-detuned lattice parameters were the same as for the previous experiment and the sequence of the cooling was repeated.

In figure 7.5 the measured temperature of the atoms is again plotted versus the magnetic field. This time it is possible to distinguish the first of the two resonances, while the second one appears to be very broadened and the features do not have the expected Lorentzian shape observed in [20].

The spatial profile of the far-detuned lattice beam was studied in chapter 4 and

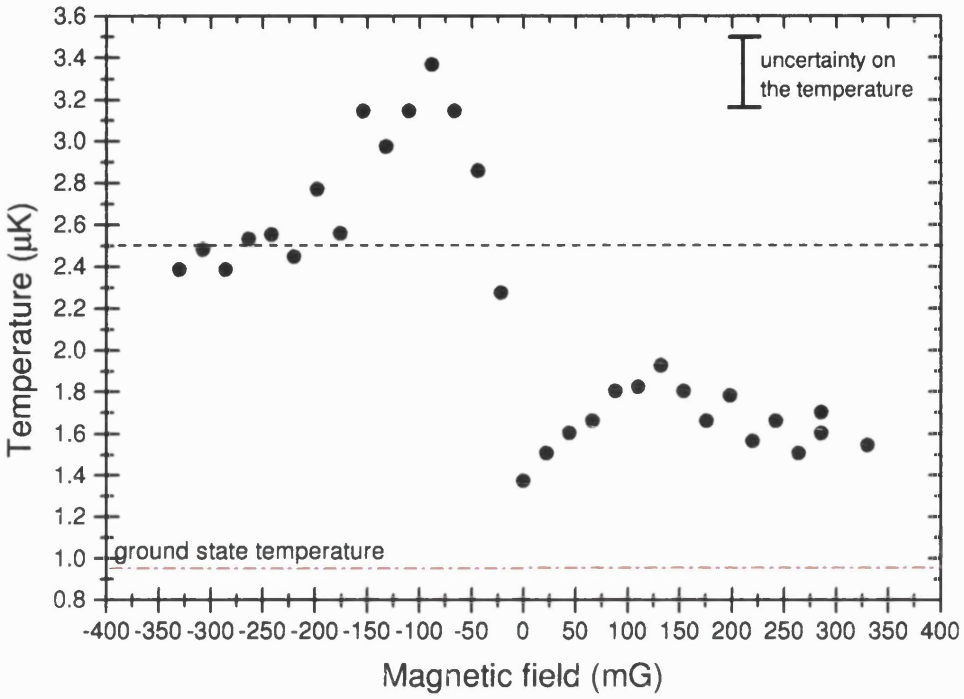

Figure 7.5: Temperature variation versus static magnetic field along the z-axis for a sideband Raman-cooled sample of atoms. The uncertainty in the temperature is represented in figure and corresponds to 0.2μK. The dotted line represents the initial temperature of the sample $T_{ini} = (2.5 \pm 0.2)\mu$K.

was found to lead to a inhomogeneous potential, which in turn means that wells at different spatial locations bind atoms with different characteristic vibrational frequencies. An estimated $(10-20)\%$ variation of the optical potential in the trap region would correspond to $(5-10)\%$ variation in the vibrational frequency, in the harmonic approximation. This would lead to less efficient cooling as not all of the atoms are cooled simultaneously and also to a broadening of the resonances, as for a wider range of magnetic field values there are still some levels brought into degeneracy. This problem could be avoided had it been possible to expand the lattice beam and select a spatially homogeneous region, such that the full-width at half-maximum of the laser profile is much bigger than the full-width at half-

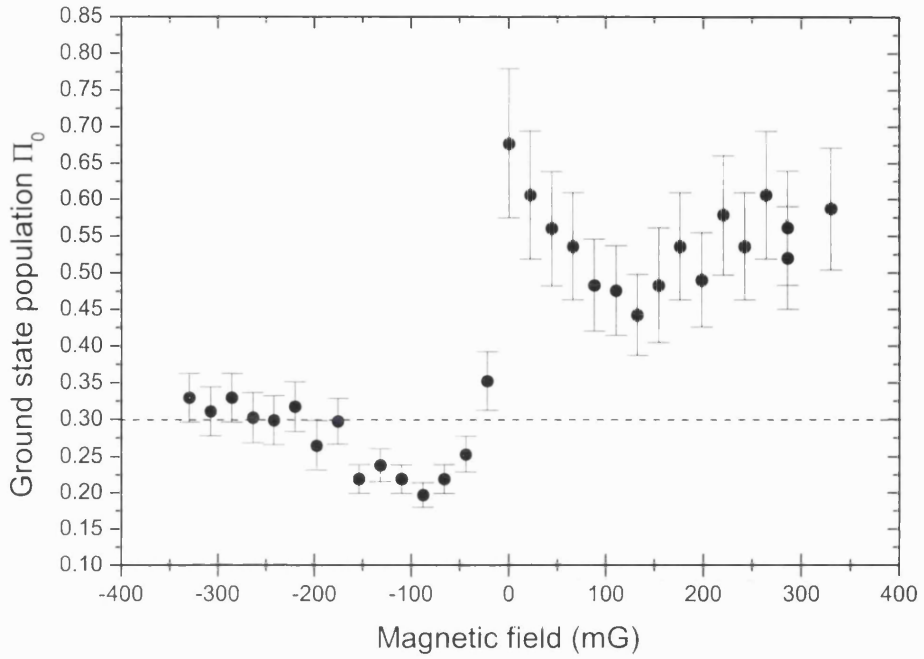

Figure 7.6: Population of the 2-D ground state with $n_x = 0, n_y = 0$ versus static magnetic field along the z-axis for a sideband Raman-cooled sample of atoms. The dotted line represent the ground state population for the uncooled sample at a temperature of 2.5μK.

maximum of the extension of the sample of atoms. Power limitations, however, did not allow us to expand the beam further. A compression of the MOT was also attempted, but the experiment showed only a modest improvement.

Returning to figure 7.5, we observe that for negative values of the magnetic field there is a sharp increase in temperature, corresponding to the levels $|m_F = -4, n_i\rangle$ being brought into degeneracy with higher lying states. This can be explained by observing that for negative values of the magnetic field the Zeeman shift is in the opposite direction, therefore levels $|m_F = -4, n\rangle$ can be brought into degeneracy with $|m_F = -3, n-1\rangle$, thus heating the sample. At higher values of the magnetic field the induced coherences with higher lying vibrational states become negligible and the temperature drops again. In figure 7.5 the presence of a magnetic field offset can be observed, which is due to non compensated stray fields.

The ground state population for a 1-D harmonic oscillator was found to increase up to 85%. Again the population of the ground state was calculated from the measured kinetic energy for a 2-D harmonic oscillator, assuming that the temperature is the same for x and y dimensions. Figure 7.6 shows the population of the ground state plotted against the applied magnetic field; the number of atoms in the ground state is increased from 30% to 70%, showing an improved efficiency of the Raman cooling.

The error on the ground state population measurement is mainly due to systematic errors in the temperature estimate (see section 3.8). An improvement of the accuracy of temperature measurements should be pursued in the future. In fact for very low temperatures the small uncertainty leads to a large error in the determination of the population of the ground state.

In conclusion the sideband-Raman cooling scheme was proved to be efficient and to work as expected. Nevertheless the experimental setup needs to be further improved in order to achieve higher accumulation of atoms in the ground vibrational state. It was found that the inhomogeneities in the far-detuned potential depth along the trapping region lead to a broadening of the Raman resonances and to a reduced efficiency. This can be avoided by using a more powerful laser source and expanding the beam, thus selecting a uniform region of laser intensity and therefore creating a uniform potential depth for all the atoms in the lattice. For this purpose a Ti:Sapphire laser, capable of producing 1W optical power, has already been purchased and installed.

7.3 Conclusions

In this chapter I have described the implementation of a resolved-sideband Raman cooling scheme first suggested in [18], which was used to prepare a large fraction of atoms in the ground vibrational state of the 2-D optical potential associated

with the $|m_F = -4\rangle$ state. When prepared in this fashion, atoms in the lattice are in identical, pure quantum states both with respect to their motional and internal degree of freedom. Sideband cooling occurs between vibrational levels in Zeeman substates and Raman coupling is provided by the lattice beams themselves. A longitudinal magnetic field tunes the lattice to the first red sideband to initiate cooling. This method was found to be very sensitive to the initial temperature of the sample, reflecting the high degree of anharmonicity of the lattice. Furthermore, the results were compromised by the non-uniform potential depth at different lattice sites, due to limitations in the available laser source power. Nevertheless, the method was very efficient and permitted us to prepare 85% of the total population in the one-dimensional ground vibrational state. The efficiency of cooling in two dimensions allowed us to increase the population of the 2-D vibrational ground state from 30% to 70% in the cooled sample. By improving the experimental apparatus and using a more powerful laser source, it should be possible to improve the efficiency of our method.

These results open up the possibility of performing a wide range of experiments involving the coherent manipulation of a quantum state using adiabatic rapid passage, which closely relates to this method for sideband-Raman cooling as it employs the same coherent coupling. Ultimately, exploiting the techniques for band population measurements (chapter 4) and Zeeman state analysis (chapter 6) it will be possible to implement methods for quantum state measurements [19].

CHAPTER 8

Conclusions

Optical lattices present us with a rich and flexible system for the preparation and manipulation of quantum states of neutral atoms. The light-shift potential can be varied in depth, shape and periodicity by simply changing the laser beam geometry, intensity and polarization as well as via the introduction of external fields. Coherent couplings between atomic states can be engineered in a way that makes it possible to manipulate the quantum state of atoms in the far-detuned lattice and prepare atoms in a chosen quantum state.

In the far-detuned regime, optical lattices for neutral atoms offer many advantages for quantum state preparation and control, as the decoherence caused by spontaneous emission is almost suppressed, and due to the weak coupling to the environment. Furthermore, the low filling factor typical of optical lattices allows atoms to be isolated from each other. Far-detuned optical lattices therefore constitute a suitable environment for studies of quantum transport and quantum chaos which can be performed with atoms prepared in such a manner; Fock states and Schrödinger cat states can be generated, while tunneling between double well potentials in a lattice can also be investigated [21]. Neutral atoms in far-detuned optical lattices may also be suitable candidates for quantum computation. At the

heart of quantum computation concepts lies the entanglement of many two-state systems (qubits), which form the register of the quantum computer. Recently, a new system for implementing quantum logic gates has been suggested [55], which exploits trapped neutral atoms stored at different locations in a far-detuned optical lattice that can be made to interact via laser-induced coherent electric dipole-dipole interaction. The difficulty in this method lies in addressing and reading out the state of individual qubits, which are generally spaced closer than the optical wavelength. Lattices can be however designed with more widely separated wells, for example by using a very long wavelength laser (such as an intense CO_2 laser [38]). Ultimately, quantum computing may require trap arrays which would allow atoms to be separately manipulated and read out, [56], [57].

In this thesis I investigated a 2-dimensional configuration for a far-detuned optical lattice, which has been proved to be ideal for exploiting a simple scheme of sideband-Raman cooling as the first step for quantum state preparation, [20]. This work was aimed at the preparation of a large fraction of atoms in the vibrational ground state of a 2-D far-detuned optical potential. The implementation of the experimental setup and the optimization of the loading of atoms in the FDL were the first objectives of this thesis. A scheme for sideband-Raman cooling was then successfully implemented, which led to the preparation of a large fraction of atoms in the ground vibrational state of the 2-D optical potential associated with the $|m_F = -4\rangle$ state. With the purpose of promoting and examining the efficiency of loading and optimizing the effectiveness of sideband-cooling, several diagnostic methods were implemented. Experiments were performed aimed at quantifying the populations of different vibrational levels and at the Zeeman state analysis of the atoms in the sample. These techniques were demonstrated to be effective with a variety of experiments.

I will now give a brief summary of the thesis with reference to the work pre-

sented in each chapter. Chapter 1 gave an overview on the theoretical background in laser cooling and optical lattices in one, two and three dimensions. In chapter 2, the results of band structure calculations for a 2-D far-detuned configuration were presented along with a a theoretical study of the sideband-Raman cooling technique proposed in [16] and a calculation of various parameters. Chapter 3 was dedicated to the description of the experimental apparatus. In chapter 4 the loading technique for the far-detuned lattice was illustrated in detail. In the same chapter the optimization of the loading efficiency and storage properties of the lattice were studied. Band population measurements were also performed, which lead to the confirmation of the existence of band-dependent loss mechanisms in the far-detuned lattice. It became evident from these experiments and from imaging the lattice beams intensity profile, that the non-homogeneity of the latter constitutes a major limitation of the experiment. In chapter 5 the optical potential was further investigated through parametric excitation experiments and modelling. These measurements yielded insight into the anharmonicity of the optical potential and the effects of non-uniform intensity profiles. It was found that these cause a significant spread in the vibrational frequencies of the atoms. The model was also used to simulate the heating induced by laser intensity fluctuations; this was shown to be partly responsible for the band-dependent losses of atoms in the far-detuned lattice, but also to be reasonably low so as not to affect the sideband cooling.

A Zeeman-state analysis of the sample via Stern-Gerlach experiments, allowed the measurement of the magnetization of our sample of atoms as well as the resolution of single m_F states. The evolution of the population of such states was also reconstructed by varying an external static magnetic field along the quantization axis. Spin-polarization was proved to be efficient and a phenomenological spin-temperature could be evaluated, in agreement with [48]. Furthermore, the

possibility of measuring the population of single Zeeman states yielded more convincing proof for the existence of a spin temperature than the results presented in [48], where only the total population of a $\sigma^{\pm}$-well could be measured. Zeeman state analysis also enabled us to verify that the net magnetization of the sample in the near-resonant lattice is preserved after its transfer to the far-detuned lattice. In particular it allowed the preparation and measurement of a large fraction of atoms in the $|m_F = \pm 4\rangle$ state, which could further improve the efficiency of the sideband-Raman cooling scheme used for quantum state preparation.

In the last chapter a resolved-sideband Raman cooling setup was implemented. Sideband cooling occurs between vibrational levels in Zeeman substates and Raman coupling is provided by the lattice beams themselves. A longitudinal magnetic field tunes the energy difference between vibrational states of distinct Zeeman sublevels. This method was found to be very sensitive to the initial temperature of the sample, reflecting a high degree of anharmonicity of the lattice. Furthermore, the results were compromised by the non-uniform potential depth at different lattice sites, due to limitations in the laser source available power. Nevertheless, the method was very efficient and permitted us to prepare 85% of the total population in the one-dimensional ground vibrational state. The efficiency of cooling in two dimensions led to an increase of the population of the 2-D vibrational ground state from 30% to 70% in the cooled sample. By improving the experimental apparatus and using a more powerful laser source so that inhomogeneous variation in the vibrational frequency over the lattice size is eliminated (i.e when the potential depth is uniform over the total spatial extent of the trap), it should be possible to further enhance the efficiency of this method.

In conclusion this thesis presents an extensive study of neutral atoms in far-detuned optical lattices. Experiments were implemented aimed at diagnosing the potential properties, such as characteristic frequencies, anharmonicity effects and

inhomogeneities of the potential depth. Measurements were performed to resolve the populations of the single vibrational bands and single Zeeman states, which could also allow the measurement of the quantum state of the sample. Raman-sideband cooling led to prepare in excess of 70% of the atoms in the 2-D $|m_F = -4, n_x = 0, n_y = 0\rangle$ state. The limitations of the current experiment have to be mostly attributed to the low laser power available and the non-uniform spatial profile of the beams. The laser source used throughout this work has been now replaced by a Ti:Sapphire laser capable of up to 1W output power; this should allow the creation of a uniform intensity profile for the optical lattice, which will definitely improve the experiments and the Raman cooling efficiency.

The outcome of this work opens up the possibility of performing a wide range of experiments involving the coherent manipulation of single quantum states using adiabatic rapid passage, which is closely related to the method for sideband-Raman cooling as it uses the same coherent coupling. Ultimately, exploiting the techniques for band population measurements (chapter 4) and Zeeman state analysis (chapter 6) it will be possible to implement methods for quantum state measurements [19]. Eventually this will open up the way to the controlled engineering of the individual quantum states of trapped atoms, as a precursor to the encoding and processing of information at the quantum level.

BIBLIOGRAPHY

[1] T. W. Hänsch and A. L. Shawlow. *Optics Comm.*, 13:68, 1975.

[2] C. Cohen-Tannoudji. *Atomic motion in laser light, Les Houches.*

[3] W. D. Phillips. *Atomic motion in laser light, Les Houches.*

[4] D. E. Pritchard, E. Raab, V. Bagnato, C. Wieman, and E. Watts. *Phys. Rev. Lett.*, 57:310, 1986.

[5] J. Dalibard and C. Cohen-Tannoudji. *J. Opt. Soc. Am. B*, 2:1707, 1985.

[6] S. Chu, J. E. Bjorkholm, L. Hollberg, A. Cable, and A. Ashkin. *Physical Review Letters*, 55:48, 1985.

[7] S. Chu, L. Hollberg, J. E. Bjorkholm, A. Ashkin, and A. Cable. *Physical Review Letters*, 57:314, 1986.

[8] P. D. Lett, R. N. Watts, C. I. Westbrook, and W. D. Phillips. *Phys. Rev. Lett.*, 61:169, 1988.

[9] C. Salomon, J. Dalibard, W. D. Phillips, A. Clairon, and S. Guellati. *Europhys. Lett.*, 12:683, 1990.

[10] P. J. Ungar, D. S. Weiss, E. Riis, and S. Chu. *J. Opt. Soc. Am. B*, 6:2058, 1989.

[11] I. H. Deutsch, J. Grondalski, and P. M. Alsing. *Phys. Rev. A*, 56:1705, 1997.

[12] G. Raithel, W. D. Phillips, and S. L. Rolston. *Phys. Rev. A*, 58:R2660, 1998.

[13] G. Raithel, G. Birkl, A. Kastberg, W. D. Phillips, and S. L. Rolston. *Phys. Rev. Lett.*, 78:630, 1997.

[14] K. I. Petsas, A. B. Coates, and G. Grynberg. *Phys. Rev. A*, 50:5173, 1994.

[15] D. R. Meacher. *Contemp. Phys.*, 39:329, 1998.

[16] P. S. Jessen and I. H. Deutsch. *Adv. Atom. Mol. Opt. Phys*, 37:95, 1998.

[17] Y. Castin and J. Dalibard. *Europhys. Lett.*, 14:761, 1991.

[18] I. H. Deutsch and P. S. Jessen. *Physical Review A*, 57:1972, 1998.

[19] G. Klose, G. Smith, and P. S. Jessen. *Physical Review Letters*, 86:4721, 2001.

[20] S. E. Hamann, D. L. Haycock, G. Klose, P. H. Pax, I. H. Deutsch, and P. S. Jessen. *Physical Review Lett*, 80:4149, 1998.

[21] D. L. Haycock; S. E. Hamann, G.Klose, and P. S. Jessen. *Physical Review A*, 55:R3991, 1998.

[22] N. W. Ashcroft and N. D. Mermin. *Solid State Physics*, Saunders, 1976.

[23] Federick Reif. *Statistical and thermal physics.*

[24] P. H. Jones. *Ph.D Thesis, Oxford University*, 2001.

[25] L. Goldberg, D. Mehuys, M. R. Surette, and D. C. Hall. *IEEE J. Quantum Electr.*, 29:2028, 1993.

[26] A. C. Wilson, J. C. Sharpe, C. R. McKenzie, P. J. Manson, and D. M. Warrington. *Appl. Opt.*, 37:4871, 1998.

[27] J. N. Walpole. *Opt. Quantum Elect.*, 28:623, 1996.

[28] L. Ricci, M. Weidmüller, T. Esslinger, A. Hemmerich, C. Zimmerman, V. Vuletic, W. König, and T. W. Hänsch.

[29] G. D. Rovera, G. Santarelli, and A. Clairon. *Rev. Sci. Instrum.*, 65:1502, 1995.

[30] I. Serre, L. Pruvost, and H. T. Duong. *Appl. Opt.*, 37:1016, 1998.

[31] A. Lambrecht, E. Giacobino, and S. Reynaud. *Quantum Semic. Opt.*, 8:457, 1996.

[32] D. L. Haycock, S. E. Hamann, G. Klose, G. Raithel, and P. S. Jessen. *Phys. Rev. A*, 57:R705, 1998.

[33] T. Müller-Seydlitz, M. Harlt, H. Hänsel, C. Keller, A. Schnetz, R. J. C. Spreeuw, T. Pfau, and J. Mlynek. *Physical Review Letters*, 78:1038, 1997.

[34] T. M. DePue, S. L. Winoto, D. J. Han, and D. S. Weiss. *Opt. Comm.*, 180:73, 2000.

[35] T. Müller, M. Harlt, H. Hänsel, C. Keller, A. Schnetz, R. J. C. Spreeuw, T. Pfau, and J. Mlynek. *Phys. Rev. lett*, 78:1038, 1997.

[36] T. Esslinger, F. Sanders, A. Hemmerich, T. W. Hänsch, H. Ritsch, and M. Weidmüller. *Opt. Lett.*, 21:991, 1996.

[37] M. Doery, M. Widmer, E. Vredenbregt, T. Bergeman, and H. Metacalf. *Phys. Rev. Lett*, 72:2546, 1994.

[38] S. Friebel, C. D'Andrea, J. Waltz, M. Weitz, and T. W. Hänsch. *Physical Review A*, 57:R20, 1998.

[39] R. Jáuregui, N. Poli, G. Roati, and G. Modugno. *Physical Review A*, 64:a.33403, 2001.

[40] T. A. Savard, K. M. O'Hara, and J. E. Thomas. *Physical Review A*, 56:R1095, 1997.

[41] C. W. Gardiner, J. Ye, H. C. Nagerl, and H. J. Kimble. *Physical Review A*, 61:045801, 2000.

[42] R. Járegui. *Physical Review A*, 64:R05348, 2001.

[43] G. Roati, W. Jastrzebski, A. Simoni, G. Modugno, and M. Inguscio. *Physical Review A*, 63:052709, 2000.

[44] N. Poli, R. J. Brecha, G. Roati, and G. Modugno. *Physical Review A*, 65:a.21401, 2002.

[45] M. E. Gehm, K. M. O'Hara, T. A. Savard, and J.E. Thomas. *Physical Review A*, 58:3914, 1998.

[46] T. M. Roach, H. Abele, M. G. Boshier, H. L. Grossman, K. P. Zetie, and E. A. Hinds. *Physical review Letters*, 75:629, 1995.

[47] W. G. Kaenders, F. Lison, I. Müller, A. Richter, R. Wynands, and D. Meschede. *Physical Review A*, 54:5067, 1996.

[48] D. Meacher, S. Guibal, C. Mennerat, J. Courtois, K. Petsas, and G. Grynberg. *Physical Review Letters*, 74:1958, 1995.

[49] B. H. Bransden and C. J. Joachin. *Physics of Atoms and Molecules.* Longman, 1983.

[50] M. Morinaga, I. Bouchoule, J-C. Karam, and C. Salomon. *Phys. Rev. Lett.*, 83:4037, 1999.

[51] C. Monroe, D. Meekhof, B. King, S. Jefferts, W. Itano, and D. Wineland. *Physical Review Letters*, 75:403, 1995.

[52] F. Diedrich, J. Bergquist, W. Itano, and D. Wineland. *Physical Review Letters*, 62:403, 1989.

[53] H. Perrin, A. Kuhn, I. Bouchoule, and C. Salomon. *EuroPhys. Lett.*, 42:395, 1998.

[54] S. Wolf, S. J. Oliver, and D. S. Weiss. *Phys. Rev. Lett.*, 85:4249, 2000.

[55] G. K. Brennen, C. M. Caves, P. S. Jessen, and I. H. Deutsch. *Phys. Rev. Lett.*, 82:1060, 1999.

[56] N. Schlosser, G. Reymond, I. Protsenko, and P. Grangier. *Nature*, 411:1024, 2001.

[57] I. E. Protsenko, G. Reymond, N. Schlosser, and P. Grangier. *Phys. Rev. A*, 65:52301, 2002.